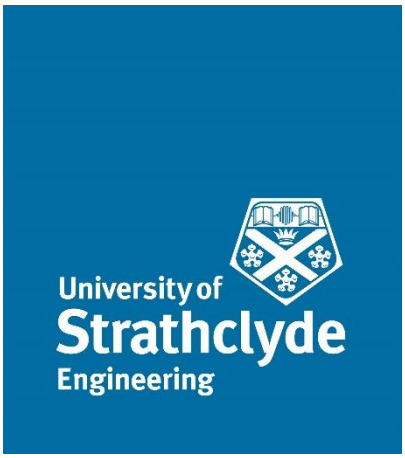

Study on structural integrity of welded components using the LMM

Manu Puliyaneth

Structural Integrity and Lifetime Assessment Research Group

Department of Mechanical and Aerospace Engineering

University of Strathclyde, Glasgow

2020

This thesis is the result of the author's original research. It has been composed by the author and has not been previously submitted for examination which has led to the award of a degree.

Manu Puliyaneth
November 16, 2020

Acknowledgements

Firstly, I would like to thank my supervisor, Dr Haofeng Chen. Without his continuous support and guidance throughout my PhD study, I would not have been able to complete it and submit this thesis. The innumerable discussions I have had with him has helped me become a better engineer.

I would also like to thank my colleagues from the SILA group Dario, Cho, Ross, Graeme, Taylor, Zhuyian Ma, and Xiao Xiao. Thanks to you all, my life was enjoyable both within and outside the university. Special thanks to Daniele for his support during my initial days in Glasgow and within the department. I hope to maintain this friendship and wish the best for all of you.

I would like to express my gratitude and love towards my parents,V. P. Chandranathan Pillai and Sreedevi Chandranathan Pillai, for their unconditional support, encouragement and prayers throughout my life. Special thanks to my brother Arjun whose calls have always been a stress buster for me.

I would like to offer my prayers to my spiritual guru Mata Amritanandamayi Amma, whose blessing made my PhD work and the writing of this thesis possible.

Finally, I would like to thank my wife Swathy for your patience, and for putting up with my ups and downs during this study. Life has become much more beautiful since our marriage and I will love you forever.

To Achan and Amma

Abstract

Industries, which have structures, subjected to high temperatures, such as the nuclear power plant industry, give paramount importance to structural integrity assessments due to the obvious catastrophic effect an unfortunate failure might cause. The presence of welds increases the susceptibility of premature failure within the structures. Hence identifying the structural response of welded components under cyclic loading conditions and developing methods to predict their safe life is of significant importance.

The work within this thesis focuses on the investigation of cyclic plasticity and creep-cyclic plasticity interaction of welded components, and the consequential damage assessment using the Linear Matching Method (LMM). Firstly, a numerical investigation and parametric study on the cyclic plasticity behaviour of a butt-welded pipe under cyclic thermal and constant pressure load is undertaken. The most critical results are used to create limit load envelopes that may be used to design welded pipes within the specified range. Secondly, through a series of case studies, the effect of various complex loading conditions on the evolution and progress of fatigue damage, creep damage and creep-fatigue interaction of welded connectors, commonly found in power plants, are identified and discussed comprehensively using the Direct Steady Cycle Analysis (DSCA) and the extended Direct Steady Cycle Analysis (eDSCA) method within the Linear Matching Method Framework (LMMF). Finally, the subroutine is enhanced to account for any previous residual stress such as the welding residual stress (WRS) on the shakedown-ratchet limit interaction curves and the creep-fatigue endurance. With a welded flange case study, the effect of WRS on mean strain during the transient cycles and the fatigue damage at steady state is demonstrated.

Publications

1. **Puliyaneth, M.**, Barbera, D., Chen, H., & Xuan, F. “Study of ratchet limit and cyclic response of welded pipe”, International Journal of Pressure Vessels and Piping, Volume 168, December 2018, Pages 49-58.

2. **Puliyaneth, M.**, Chen, H. & Weiling, L. “Creep Fatigue Damage Assessment of V-Butt Weld Pipe With an Extended Direct Steady Cycle Analysis”, ASME 2018 Pressure Vessels and Piping Conference. Volume 5, PVP2018-84568. July 2018.

3. **Puliyaneth, M.**, Chen, H. & Weiling, L. “Cyclic Plasticity Analysis of Welded Joint With Welding Residual Stress Using the Direct Method”, ASME 2019 Pressure Vessels and Piping Conference. Volume 6A, PVP2019-93228. July 2019.

4. **Puliyaneth, M.,** Jackson, G., Chen, H. & Liu, Y. “The Linear Matching Method and Its Software Tool for Creep Fatigue Damage Assessment”, Direct Methods: Methodological Progress and Engineering Applications, Lecture Notes in Applied and Computational Mechanics. July 2020.

5. **Puliyaneth, M.** & Chen, H. “Creep-cyclic plasticity and damage assessment of an SS304 weldolet”, Submitted to Journal of Pressure Vessel Technology.

6. **Puliyaneth, M.** & Chen, H. “Study on the effect of welding residual stress on creep-cyclic plasticity”, Submitted to International Journal of Pressure Vessels and Piping.

Awards

1. Engineering the Future (ETF) Studentship, University of Strathclyde, July 2016.
2. Postgraduate Research Travel Award, University of Strathclyde, July 2018.
3. Finalist, ASME PVP Conference, July 2018.


ASME
SETTING THE STANDARD

Manu Puliyaneth
University of Strathclyde

CERTIFICATE OF RECOGNITION

FINALIST (PHD CATEGORY) IN THE RUDY SCAVUZZO STUDENT PAPER SYMPOSIUM & 26TH ANNUAL STUDENT PAPER COMPETITION AT THE 2018 ASME PVP CONFERENCE WITH PAPER TITLED

"Creep Fatigue Damage Assessment of V-butt Weld Pipe with an Extended Direct Steady Cycle Analysis"

Douglas A. Scarth
CHAIR, SENATE OPERATIONS COMMITTEE

Trevor G. Seipp
CHAIR, PVPD HONORS & AWARDS

JULY 2018

Contents

List of tables

List of figures

Nomenclatures

α	Coefficient of thermal expansion
α^{PM},α^{HAZ}, α^{WM}	Coefficients of thermal expansion for PM, HAZ and WM
$\dot{\bar{\varepsilon}}_C$	Instantaneous creep strain rate
$\Delta\varepsilon_c$	Inelastic strain increment due to creep
$\Delta\varepsilon_e$	Elastic strain range
$\Delta\varepsilon_p$	Plastic strain range
$\Delta\varepsilon_r$	Ratcheting strain per cycle
$\Delta\varepsilon$	Total strain range
$\Delta\theta$	Temperature/thermal load range
$\Delta\sigma$	Total stress range
$\bar{\varepsilon}_C$	Creep ductility
$\bar{\varepsilon}_{MDF}$	Creep ductility considering MDF
$\dot{\varepsilon}^{cr}$	Creep strain rate
$\bar{\varepsilon}_{ec}$	Equivalent creep strain
ε_F	Fracture ductility
ε_L	Lower shelf creep ductility at the lower strain rate
ε_U	Upper shelf creep ductility at the high strain rate
ε_a	The amplitude of the total strain

ε_{cr}	Accumulated strain at which the component is considered to fail.
ε_f', c, σ_f', b	Coefficient for Manson-Coffin-Basquin equation
ε_{pm}	Mean strain
θ_0	The temperature at the outside surface of the component
σ	Stress
$\bar{\sigma}$	Equivalent stress
σ_1, σ_2, σ_3	Maximum, medium, and minimum principal stresses
σ_H	Hydrostatic stress or mean stress
σ_{ax}	Additional axial load on the pipe
σ_{ax}^c	Axial stress due to the internal pressure only in a closed-end situation
σ_{cs}	Stress at the beginning of dwell period for steady-state
σ_{mdh}	Mean diameter hoop stress
σ_{rup}	Multiaxial rupture stress
σ_{UTS}	Ultimate Tensile Strength
σ_y^{PM}, σ_y^{HAZ}, σ_y^{WM}	Yield stresses of PM, HAZ and WM
υ	Poisson's ratio
B, n, m	Norton-Bailey law constants
B^{DE}, n^{DE}	Material constants for the DE model
B_{RO}, β_{RO}	RO model parameters
B^{TF}, k^{TF}	Creep damage constants for the TF model

d_C^{TF}	Creep damage per cycle-TF model
d_c	Creep damage per cycle
d_c^{R5}	Creep damage per cycle-DE model
d_f	Fatigue damage per cycle
D	Total damage
D_{CI}	Creep damage due to the transient cycles
D_{CS}	Creep damage at steady-state
D_{FM}	Fatigue damage considering the effect of the mean strain
D_c/φ_c	Creep damage
D_f/φ_f	Fatigue damage
$\bar{E}$	Equivalent Young's modulus
E_y^{PM}, E_y^{HAZ}, E_y^{WM}	Young's moduli of PM, HAZ and WM
k_a	Axial stress ratio parameter
l_{PM}	Limit load of a pure PM pipe
M_L	Limit bending moment
N_0	Number of cycles to initiate a crack having a size of a_0
N_f	Number of cycles to fatigue failure
N_r	Number of cycles to failure by ratcheting
p	Pressure applied
P_L	Limit pressure
q	Axial load due to pressure

Q_{act}	Activation energy
R_{gas}	Global gas constant
t	Time
t_h	Duration for creep dwell
t_f	Creep rupture time at failure
t^{rup}	Time to rupture – TF model
T	Temperature
Z	Elastic follow up factor

Acronyms

ASME NH	American Society of Mechanical Engineers Boiler and Pressure Vessel Code Section III Subsection NH
AWS	American Welding Society
CAE	Computer-Aided Engineering
CDM	Continuum Damage Mechanics
DE	Ductility Exhaustion
DSCA	Direct Steady Cycle Analysis
ECM	Elastic Compensation Method
eDSCA	extended Direct Steady Cycle Analysis
EPP	Elastic-Perfectly Plastic
FEA	Finite Element Analysis
FSRF	Fatigue Strength Reduction Factor
GUI	Graphical User Interface
HAZ	Heat Affected Zone
HCF	High cycle fatigue
LCF	Low Cycle Fatigue
LDSR	Linear Damage Summation Rule
LMMF	Linear Matching Method Framework
PEEQ	Equivalent plastic strain
PEMAG	Plastic strain magnitude

PM	Parent Metal
R5	Assessment procedure for the high-temperature response of a structure
RCC-MR	Design and Construction Rules for Mechanical Components in high-temperature structures, experimental reactors and fusion reactors
RO	Ramberg Osgood
SMDE	Stress Modified Ductility Exhaustion
TF	Time Fraction
TMF	Thermomechanical fatigue
UMAT	User subroutine to define a material's mechanical behaviour
WER	Weld Endurance Reduction
WM	Weld Metal
WRS	Welding Residual Stress
WSEF	Weld Strain Enhancement Factor

This page is intentionally left blank

Chapter 1 Introduction

1.1 Research background

Energy demand has risen considerably over the past few decades and is expected to become double-fold by 2050. This coupled with the rising concerns over the large CO_2 emissions by the current power sector calls for the exploration and development of new generation power plants that run on renewable and nuclear energy sources. As of 2018, around 47.5% of electricity in the UK was still generated from gas, coal and other oil sources with an estimated 448.5 million tonnes of CO_2 equivalent emission [1].

The basic principle behind a nuclear power plant in terms of power generation is similar to conventional power plants. The difference being in the way the heat required to produce the steam that rotates the turbine blades are generated. Currently, the UK has 15 power plants in operation, of which some are approaching the end of their design life [2] and some are operating beyond the original design life [3]. While these power plants were initially put in service, a safe operational life was predicted based on the technology and structural integrity knowledge available then. Developing accurate structural integrity methodologies is critical in increasing the safe operational life of these power plants. Another 12 nuclear power plants are also scheduled to be constructed in the UK by 2030 which combined will have an electricity generation capacity of 16 GW [4]. It is widely recognised that the efficiency of power plants can be enhanced with an increase in the operating temperature [5]. Generation IV reactors, which is considered as the future of nuclear power plants and are currently researched include Gas-cooled Fast Reactor (GFR), Lead-cooled Fast Reactor (LFR), Molten Salt Reactor (MSR), Supercritical Water-cooled Reactor (SCWR), Sodium-cooled Fast Reactor (SFR) and Very High-Temperature Reactor (VHTR) [6]. The VHTR design will have a primary outlet temperature of 1000 ℃ [7]. However, the increase in operating temperature comes with the introduction of various damage mechanisms within the structure. Hence, for both the new and old nuclear power plants, structural integrity assessments are a crucial aspect.

A typical piping system in a power plant consists of different connectors such as flanges, elbows and weldolets, to mention a few. The most common and practical process to position

them within the piping system is welding. Weldments are reported to be prime locations for premature failures, hence their behaviour at high service temperature is key in predicting the life of the component [5]. The introduction of residual stress, material microstructural changes and deformations caused by welding compromises the integrity of the component [8]. The most common failure mechanisms observed in a power plant piping system are creep and fatigue. Creep and fatigue failure mechanisms are complex on their own, and in the presence of welds, their complexity is further increased. Figure 1-1 (a) and (b) present examples of cracks that initiated at weldments due to creep-fatigue interaction and creep respectively. Extensive research has been carried out to understand the creep-cyclic plasticity effects of welded structures. However, the premature failure within weldments indicates the requirement for improved understanding of the creep-cyclic plasticity mechanisms, and it is arguably more important now than it has ever been before.

a)  b) 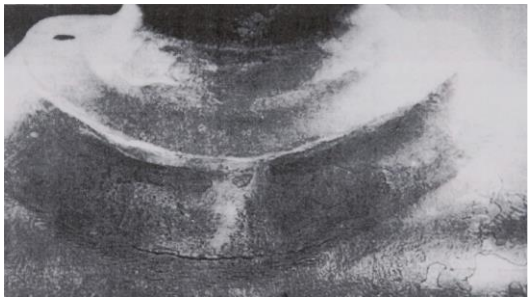

Figure 1-1 a) Creep-fatigue cracking in tailpipe-pintle welds [9]; b) Creep cracks at the weld of a branched pipe [10].

The complexity associated with welds makes experimental creep-fatigue lab testing very expensive and time-consuming, making the use of Finite Element Analysis (FEA) the most practical option. Numerous researchers have implemented Continuum Damage Mechanics (CDM) into the FEA framework to understand the cyclic plasticity and creep-cyclic plasticity behaviour of structures and have obtained remarkable results. Nevertheless, accurate modelling of the structural response requires numerous and precisely calibrated material parameters, which are not easily available. Moreover, their use in creep-fatigue damage studies is limited due to the high computational cost. An alternative to this is the use of rule-based standard codes such as The American Society of Mechanical Engineers Boiler and Pressure Vessel Code Section III subsection NH (ASME NH), the Design and Construction Rules for Mechanical Components in High-Temperature Structures, experimental reactors and fusion

reactors (RCC-MR) and the R5 Procedures for Assessing the High-Temperature Response of Structure (R5).

Though the rule-based procedures provide reasonable results, they tend to be overly conservative and are validated for a limited number of materials only. For instance, in R5, welds are analysed as parent material and its influence on the life of the structure is accounted by the Fatigue Strength Reduction Factor (FSRF) or more recently by the Weld Strain Enhancement Factor (WSEF) and Weld Endurance Reduction (WER). The reduction factors are dictated by the type and material of the weld. The FSRF method is overly pessimistic which led to the development of the WSEF and WER methods, but this too produces conservative results [11]. The predicted short life of structures, results in their early retirement which increases the running cost. Hence, there has been a constant demand from power industries to formulate alternative methods to conduct structural integrity studies.

This has led to the development of various direct methods within the structural integrity regime. The Linear Matching Method Framework (LMMF) is one such direct method. The LMMF can be broadly divided into the Linear Matching Method (LMM); the Direct Steady Cycle Analysis (DSCA); the extended Direct Steady Cycle Analysis (eDSCA). The former deals with the evaluation of limit load, shakedown, ratcheting and creep rupture boundaries while the latter two deal with the calculation of the cyclic plasticity and creep-cyclic plasticity behaviour at steady-state. The LMM is capable of use with multi-material structures such as weldments and Metal Matrix Composite's (MMC). The results from DSCA or eDSCA can be coupled with any of the aforementioned rule-based standards to assess the safe life of the structure.

1.2 Objectives of the thesis

Weldments have a critical role in limiting the safe life of a structure at high-temperature services, which makes a comprehensive understanding of their damage mechanisms important and critical. The CDM approach has been identified to give accurate results in terms of damage modelling for weldments but it requires complex constitutive modelling and extensive material data. It is particularly difficult to obtain the material data for the HAZ. Hence the process requires numerous experimental testing inherently increasing the cost. Within the power-plant industry the use of rule-based methods are much more common for damage calculations due

to their ease of use. But they tend to predict conservative life for welded components as the structure is considered to be of the parent material alone and reduction factors are imposed to account for the weldment, and does not consider the complete creep-cyclic plasticity interaction. As such the understanding of the creep damage, fatigue damage and their interactions leading to creep-fatigue and creep-ratcheting damage at welds considering the complete creep-cyclic plasticity interaction is limited and requires further research and investigation.

By taking into account these requirements and issues, the below objectives are identified and worked on in this thesis:

1) The effect of weld material properties, weld geometry and pipe dimension on the cyclic plasticity and ratchet limit of a welded pipe.

2) The effect of welds and loading conditions on the creep and fatigue damage; and creep-fatigue and creep-ratchet interaction of connectors commonly found in power plants.

3) The effect of Welding Residual Stress (WRS) on the shakedown-ratchet limit interaction curves and the creep-fatigue endurance of welded components.

1.3 Outline of the thesis

This thesis is structured to include eight chapters.

Chapter 2 introduces the basic concepts pertaining to the structural response of components subjected to high temperature. Discussions on the various damage mechanisms are also included. The chapter concludes with a brief insight into the different methodologies adopted by the ASME NH and R5 for life assessment with emphasis to welds.

Chapter 3 introduces the LMM which is the principal tool used within this study. Different facets of the LMM such as the shakedown and ratchet analysis, the DSCA and the eDSCA are presented along with a comprehensive discussion about their numerical procedure.

Chapter 4 deals with the investigation of the cyclic plasticity and ratchet limit of a welded pipe employing the ratchet limit analysis within the LMM. The parametric study included considers material and geometric factors.

Chapter 5 presents three weldment cases studies, a welded elbow, a dissimilar welded flange and a welded pipe. The former deals with the investigation and comparison of fatigue life of a single material elbow and welded elbow under various combinations of pressure, bending moment and thermal loads. The latter two focus on creep damage analysis, with the dissimilar welded flange case study focusing on the effect of thermal load on creep and provide comparisons between the Ductility Exhaustion (DE) and Time Fraction (TF) models. The welded pipe example deals with the effect of multiaxial and compressive stress, considering the TF model as recommended in RCC-MR and ASME.

Chapter 6 presents the creep-cyclic plasticity behaviour investigation and the lifetime prediction of an SS304 weldolet subjected to a cyclic thermal load and constant mechanical load through the LMM eDSCA.

Chapter 7 discusses the effect of WRS on the shakedown and ratcheting limit interaction curves. It also investigates the effect of WRS on creep and plasticity during the transient cycles, and the mean strain at steady-state which influences the fatigue life.

The thesis concludes with chapter 8 which summaries the key outputs from this research and offer recommendations for future work.

Chapter 2 High-temperature material response, design and assessment procedure

2.1 Introduction

Major damage mechanisms under cyclic loading conditions are introduced in this chapter. With the help of a Bree like diagram, cyclic plasticity responses, such as shakedown, alternating plasticity and ratcheting, are explained. A distinction between material and structural ratcheting is also presented in this chapter. An introduction to creep and creep-cyclic plasticity mechanisms including creep enhanced plasticity and cyclically enhanced creep is discussed. A comprehensive review of various types of fatigue, the total strain range and number of cycles to failure relationships, and creep damage assessment procedures are presented. Towards the latter section of the chapter R5 and ASME NH creep-fatigue damage assessment procedures are discussed.

2.2 Cyclic response of structures

A structure subjected to cyclic loading condition exhibits one of the following structural responses, namely a) elastic response; b) elastic shakedown (strict shakedown); c) plastic shakedown (global shakedown); d) ratcheting. Innumerable researches have been undertaken to understand and discuss such behaviours in components. Among them, the work presented by Bree in [12] is very comprehensive wherein a thin pipe subjected to constant mechanical load and cyclic temperature load is used to discuss various mechanisms.

Figure 2-1 shows a typical Bree diagram that is used to discuss the interaction between the cyclic and constant loads on the structure. The cyclic thermal load and the constant mechanical load are represented on the ordinate and abscissa of the plot, respectively. The various regions in the plot represent:

- Elastic response: The load applied is very small such that the structure will remain within the elastic limit during the load cycles.

- Elastic shakedown: Plastic strain is developed during the initial cycles due to yielding along with the formation of residual stress. In the subsequent cycles, the residual stress causes the structure to respond in an elastic manner.

- Plastic shakedown: A fixed range of plastic strain develops over the entire loading cycle, but without any increment in total strain accumulation. Alternating plasticity is observed leading to a closed hysteresis loop.

- Ratcheting: Plastic strain develops with every load cycle, leading to an incremental plastic collapse.

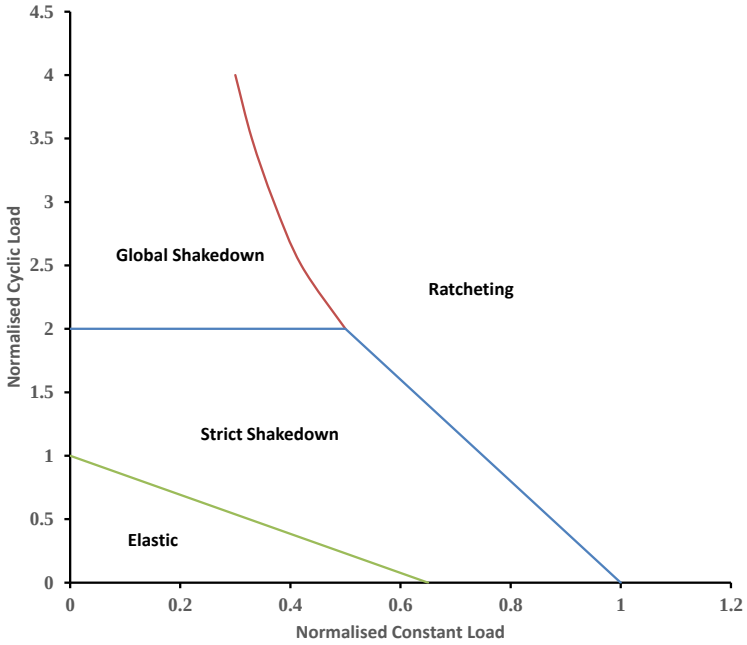

Figure 2-1 Classical Bree's like diagram for a cylinder subjected to cyclic thermal load and constant mechanical load [12], [13].

In an industrial environment, the most preferred structural response is of strict/elastic shakedown. However, this is not always possible and in many cases, a cyclic response similar to the global shakedown region is allowed as long as low cycle fatigue assessment is carried out and the component's life falls within the safety envelope. A structure under ratcheting is generally avoided unless both the number of cycles and the ratcheting strain per cycle is small.

Melan [14] and Koiter [15] are two major studies and theorems that give conditions for strict shakedown of a component. The shakedown limit analysis within the LMMF which is detailed in Section 3.2 is also based on these theorems.

a) Melan's theorem is defined as "For a given cyclic load set the structure will shakedown if a constant self-equilibrating residual stress field can be found such that the yield condition is not violated for any combination of cyclic elastic and residual stresses".

b) Koiter's theorem is defined as "For a prescribed load set P(t) with a cyclic period *t*, if any kinematically admissible strain rate can be found during a time interval (0, *t*) such that the strain field is compatible with a displacement field u (which satisfies the applied displacement boundary conditions) and

$$\int_0^t \sum P\dot{u} \geq \int_0^t \int_V \dot{D}\, dV dt \tag{2-1}$$

where $\dot{D}$ is the rate of plastic dissipation per unit volume corresponding to the admissible strain rate, then elastic shakedown has not occurred". The shakedown limit calculated using Koiter's theorem is generally greater or equal to the actual elastic shakedown limit, hence is commonly known as the upper bound shakedown theorem. Melan's theorem, on the other hand, provides conservative shakedown limits which are generally lesser or equal to the actual elastic shakedown limit, hence is known as the lower bound shakedown theorem

2.2.1 Plastic shakedown

A component within the global shakedown region exhibits plasticity during both loading and unloading at steady-state. It can be characterized by a typical closed loop as shown in Figure 2-2 and is associated with low cycle fatigue damage. Low cycle fatigue damage calculation is further discussed in Section 2.4.2.

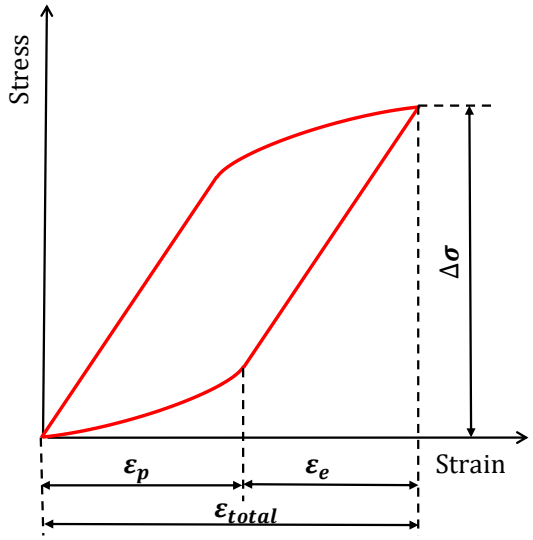

Figure 2-2 A typical hysteresis loop of a structure within global shakedown.

2.2.2 Ratcheting

Ratcheting can be studied and discussed in two aspects, structural ratcheting and material ratcheting [16]–[18]. Structural engineers associate ratcheting as a phenomenon where the strain increases by a constant amount in each load cycle whereas engineers from the material research domain associate ratcheting as the accumulation of strain even if gradually the rate of accumulation decreases and a steady-state is reached [17]. Material ratcheting is a material related effect and hardening/softening of the material plays an important role. Structural ratcheting can occur even in the absence of material ratcheting. For structural ratcheting, whether or not a ratcheting mechanism is prevalent in a structure of a particular geometry and loading can be illustrated using a shakedown-ratcheting interaction diagram. Once the interaction diagram is developed for the specific geometry and type of loading, they can be used to determine whether a considered set of loading conditions will lead to excessive strain accumulation thereby leading to ratcheting. With the Elastic-Perfectly Plastic (EPP) model, strain accumulates infinitely; on the other hand, if hardening is introduced then plastic shakedown may occur after a number of cycles such that strain accumulation is bounded. This state is referred to as finite ratcheting in material ratcheting. Material ratcheting is simulated by taking the cyclic stress-strain results and using them in an appropriate hardening/softening plasticity model such as Frederick-Armstrong [19] model and Chaboche model [20]–[22]. In this study, only structural ratcheting is considered, hence the word “ratcheting” or “ratchet’’ refers to structural ratcheting only.

2.3 Creep and cyclic plasticity

2.3.1 Creep mechanism

Creep is a time-dependent damage mechanism observed in materials when subjected to loads above a certain temperature, which is generally within 0.3 to 0.5 times the melting temperature of the material. Creep consists of three stages; namely a) primary; b) secondary; and c) tertiary. A typical creep strain curve is presented in Figure 2-3. During the primary phase the creep strain rate decreases. During the secondary stage, the creep strain rate remains constant; generally, the secondary stage is the longest and most prominent phase during the creep hold. During the tertiary phase, an exponential increase in the creep strain is observed. Within this thesis, the creep effect discussions will be restricted to the primary and secondary stage.

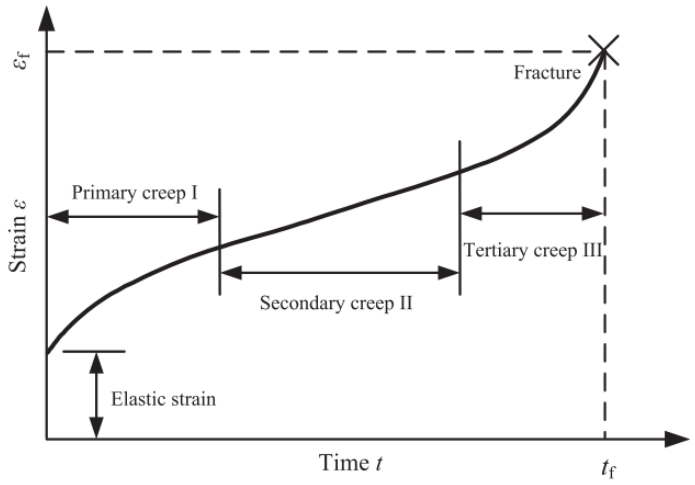

Figure 2-3 Schematic of a standard creep curve [23].

When a body is subjected to creep, the total strain range of the structure can be considered as:

$$\Delta\varepsilon = \Delta\varepsilon_e + \Delta\varepsilon_p + \Delta\varepsilon_c \tag{2-2}$$

where $\Delta\varepsilon$ is the total strain range, $\Delta\varepsilon_e$ is the elastic strain range, $\Delta\varepsilon_p$ is the plastic strain range and $\Delta\varepsilon_c$ is the inelastic strain increment due to creep. The creep strain can be expressed as a function of three parameters; a) stress (σ); b) time (t) ; and c) temperature (T), as:

$$\varepsilon_C = f_1(\sigma) f_2(t) f_3(T) \tag{2-3}$$

Boyle J.T. and Spence J. [24] listed some suggestions for the stress dependence function as:

$f_1(\sigma) = B\sigma^n$ - Norton relation

$f_1(\sigma) = C \sinh \xi\sigma$ - Prandtl relation

$f_1(\sigma) = D \exp \psi\sigma$ - Dorn relation

$f_1(\sigma) = A[\sinh(\gamma\sigma)]^n$ - Garofalo relation

$f_1(\sigma) = B(\sigma - \sigma)^n$ - Friction Stress relation

where ξ, ψ, γ, *B, C, D, A* and *n* are material constants. Similarly, the suggestions for the time-dependent function include:

$f_2(\sigma) = t$ - Secondary creep relation

$f_2(\sigma) = bt^m$ - Bailey

$f_2(\sigma) = \left(1 + bt^{1/3}\right)e^{kt}$ - Andrade

$f_2(\sigma) = \sum_j a_j t^m j$ - Graham and Walles

where *b, m, a* and *k* are material constants. The temperature-dependent function can be expressed using the Arrhenius's law as:

$f_3(T) = A\, e^{\frac{-\Delta H}{RT}}$ - Arrhenius's law

Combining Norton's relation from the stress-dependent functions and Bailey relation from the time-dependent functions gives the Norton-Bailey law. This is the most common and simple equation used to represent the primary and secondary creep strain. For an isothermal case, it is given by:

$$\varepsilon_C = B\sigma^n t^m \tag{2-4}$$

Differentiating Equation (2-4), we get the time hardening equation where the hardening phase is modelled using the time parameter, as:

$$\dot{\varepsilon_C} = mB\sigma^n t^{m-1} \tag{2-5}$$

This can be re-written in a time-independent form, commonly known as strain hardening equation, as:

$$\dot{\varepsilon_C} = \frac{mB^{\frac{1}{m}}\sigma^{\frac{n}{m}}}{\varepsilon_C^{\frac{1-m}{m}}} \tag{2-6}$$

2.3.2 Effect of creep dwell on cyclic plasticity

The response of a structure under cyclic loading at elevated temperature changes significantly with the introduction of a creep dwell. A schematic representation of the different possible creep-cyclic plasticity responses is presented in [25], [26]. If creep is introduced for load levels within the elastic limit, a hysteresis loop similar to Figure 2-4 (a) will be observed. On increasing the load levels to within the shakedown region but well below the shakedown limit, the structural response is similar to Figure 2-4 (b). For both these scenarios, at steady state, the inelastic strain accumulation that results in ratcheting is due to the creep effect.

If the load levels are further increased and plasticity occurs during unloading, the steady-state hysteresis will be either one from Figure 2-4 (c) to Figure 2-4 (f). For scenarios corresponding to Figure 2-4 (c) and Figure 2-4 (d), the reverse plasticity compensates for the creep strain and any plastic strain during loading. This results in a larger but closed hysteresis loop signifying creep-fatigue damage. If the creep strain and any plastic strain are not compensated by the reverse plasticity or vice versa, an open hysteresis loop will be observed resulting in creep-ratcheting. If the open-loop (Figure 2-4 (e)) is driven due to the enhanced creep strain, the creep-ratcheting process is termed as “cyclically enhanced creep”. For instance, consider the scenario where the structure is subjected to a large dwell time, in such cases it is possible that a very large creep strain is accumulated during the dwell period and the plastic strain during unloading cannot compensate for it. If very large stress relaxation occurs during the dwell period leading to an insignificant creep strain accumulation and large plastic strain is

accumulated during unloading, the resultant hysteresis will be similar to the one shown in Figure 2-4 (f). The open hysteresis here is driven by the reverse plasticity strain. This phenomenon is known as “creep enhanced plasticity”.

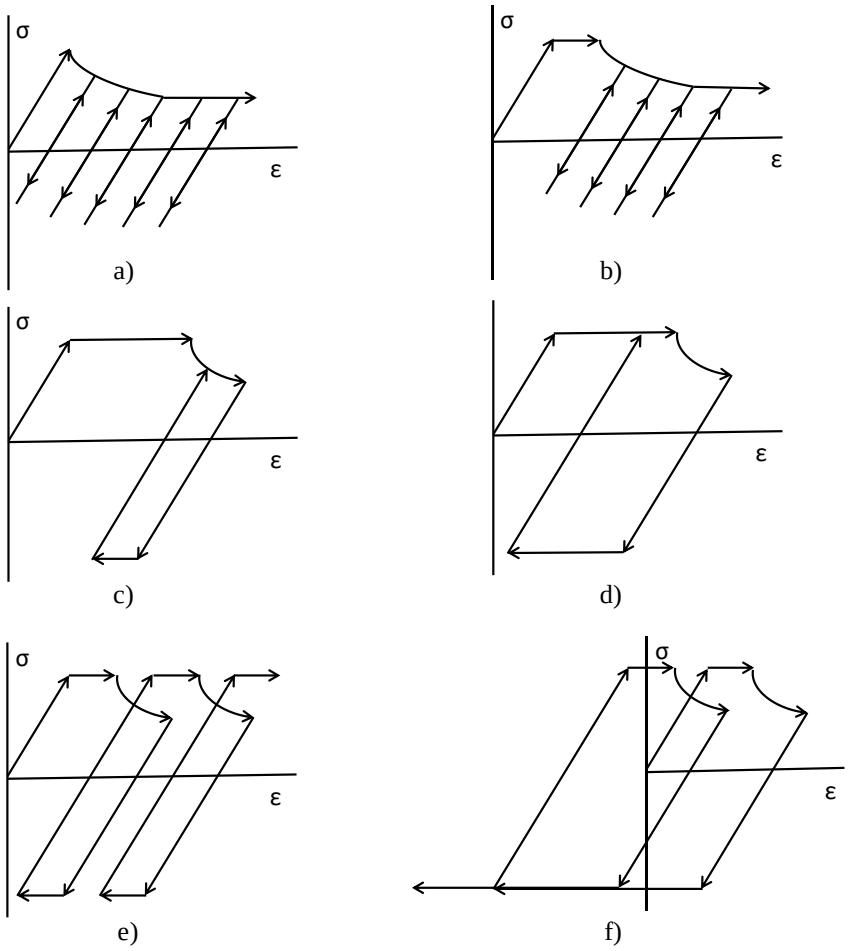

Figure 2-4 Variation in the cyclic plasticity responses with creep dwell a) elastic response [25], [26]; b) elastic shakedown [25], [26]; c) creep-cyclic plasticity due to creep enhanced reversed plasticity [25], [26]; d) creep-cyclic plasticity shakedown due to creep enhanced plasticity [25], [26]; e) creep-ratcheting due to cyclically enhanced creep; and f) creep-ratcheting due to creep enhanced plasticity.

2.4 Major damage mechanisms and interaction

2.4.1 Fatigue mechanism

Fatigue is the weakening of a material caused by repeatedly/cyclically applied loads. Fatigue failure occurs in three distinct stages: initiation, propagation and failure, as presented in Figure 2-5.

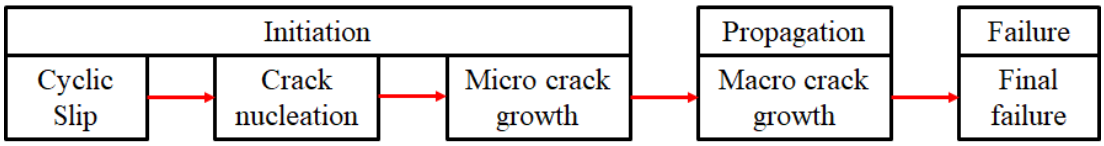

Figure 2-5 Stages of fatigue failure [27]

- Initiation: Crack initiation generally starts from the surface of the component or at the vicinity of a stress riser. The application of cyclic loads lead to the formation of slip bands, which eventually results in the generation of an intrusion or extrusion on the surface [28]. Gradually this leads to the formation of a crack.

- Propagation: Crack propagation occurs in two stages. During Stage I the crack grows along the slip band which is usually at 45° to the principal stress direction whereas in Stage II the crack grows perpendicular to the principal stress direction [28]. Compared to Stage II, crack growth rate in Stage I is very low.

- Failure: On maintaining the loading condition, crack propagates through a significant part of the cross-section and failure is considered when the remaining cross section cannot support the load.

2.4.1.1 Fatigue classification based on the number of cycles

Based on the stress level and the number of cycles to failure, fatigue can be differentiated as High Cycle Fatigue (HCF) and Low Cycle Fatigue (LCF). For HCF, the number of cycles is more than 10^4 and an elastic behaviour is observed. On the other hand, LCF is associated with the plastic response of the material and the number of cycles is less than 10^4. Generally, the

stress associated with LCF is near or at the yield stress of the material. Figure 2-6 shows a schematic diagram showing the relationship between stress and number of cycles to failure for HCF and LCF.

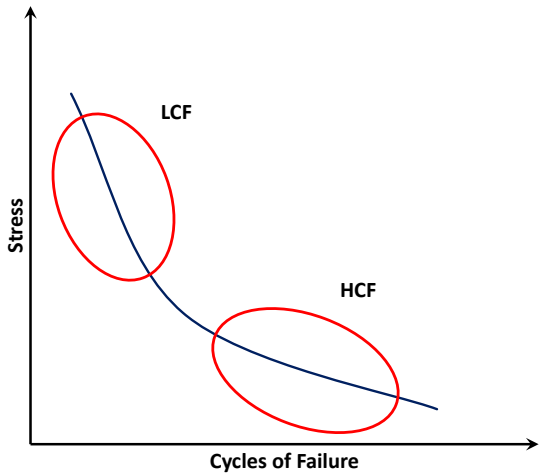

Figure 2-6 Schematic comparison of stress with HCF and LCF.

Within the power sector, LCF is more prominent compared to HCF, so within this thesis, emphasis is given to LCF damage and is discussed in depth in subsequent chapters.

2.4.1.2 Fatigue classification based on types of stress

Based on the source of the stress, fatigue can be distinguished as mechanical, thermal or a combination of both known as thermo-mechanical fatigue [29].

Mechanical fatigue

Mechanical fatigue is the most common form of fatigue [3]. It is a result of the structure being exposed to cyclic mechanical stresses for an extended period. A typical example is the vibration fatigue of equipment or piping operation. Generally materials with larger yield stress will be more resistant to mechanical fatigue [3].

Thermal fatigue

Thermal fatigue occurs due to the cyclic fluctuations of temperature the component is exposed to. It is driven by the internal stress caused by uneven expansion and contraction due to repeated heating and cooling of the component. The thermal stress (σ_{th}) is driven by two factors, a) the coefficient of thermal expansion (α) and b) the temperature range (ΔT).

$$\sigma_{th} \propto \alpha \, \Delta T \tag{2-7}$$

Thermo-mechanical fatigue

Thermomechanical Fatigue (TMF) is a combined fatigue damage that is observed in components subjected to cyclic thermal and mechanical loads. If both the thermal loads and the mechanical loads are cycled in such a way that their maximum peaks occur simultaneously, it is referred to as in-phase TMF. On the other hand, if the peaks of the thermal load and mechanical load are separated by a 180-phase lag, it is termed as out of phase TMF.

2.4.2 Low cycle fatigue

LCF has been identified as a major damage mechanism in components subjected to cyclic loads with failure occurring in less than 10^4 cycles. Its assessment has been a major research area for decades now [30]. LCF damage is influenced by the total strain range, hence effectively calculating the total strain range is key in predicting the LCF damage and life of the component. The relationship between the total strain range and number of cycles to failure is illustrated by $\Delta\varepsilon - N_f$ curve. A typical $\Delta\varepsilon - N_f$ is presented in Figure 2-7.

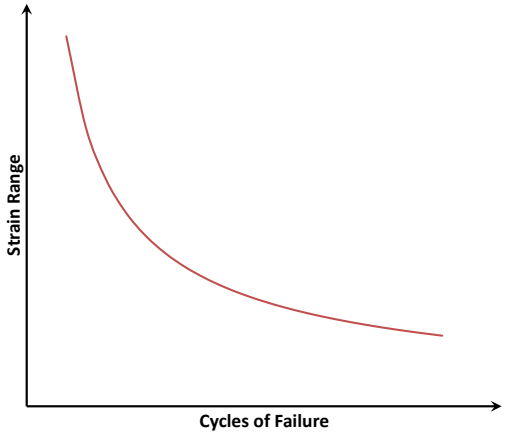

Figure 2-7 Typical $\Delta\varepsilon - N_f$ curve.

Several relationships have been formulated to relate the total strain range and the number of cycles to failure. Coffin-Manson relationship is one of the most popular ones. The total strain range, $\Delta\varepsilon$, is defined as the sum of elastic strain range, $\Delta\varepsilon_e$ and plastic strain range, $\Delta\varepsilon_p$.

$$\Delta\varepsilon = \Delta\varepsilon_e + \Delta\varepsilon_p = C_e N_f^{\beta 1} + C_p N_f^{\beta 2} \tag{2-8}$$

where C_e, C_p, $\beta 1$ and $\beta 2$ are material constants. For the number of reversals to failure, N_f, it may be expressed as:

$$\frac{\Delta\varepsilon}{2} = \frac{\Delta\varepsilon_e}{2} + \frac{\Delta\varepsilon_p}{2} = \frac{\sigma_f^{'}}{E}\left(2N_f\right)^{\beta 1} + \varepsilon_f^{'}\left(2N_f\right)^{\beta 2} \tag{2-9}$$

where $\sigma_f^{'}$ and $\beta 1$ are the fatigue strength coefficient and exponent respectively; $\varepsilon_f^{'}$ and $\beta 2$ are the fatigue ductility coefficient and exponent respectively. Ideally $\Delta\varepsilon$, E, $\varepsilon_f^{'}$, $\sigma_f^{'}$, $\beta 1$, $\beta 2$ should be experimentally obtained but the high cost and complexity associated with cyclic experiments makes it difficult [31]. Hence, monotonic material properties are used to obtain the fatigue parameters. Several researchers have modified the Coffin-Manson for various metals and have reported them in [30], [32]–[35]. Lee K. & Song J. [32] and Meggiolaro M.A. & Castro J.T.P. [35] have discussed in depth about the various methods for assessing the fatigue properties. Among the various methods, a few of the major ones are introduced below.

i. *Modified universal slopes method [30]*

The equation is proposed in the following form:

$$\Delta\varepsilon = 1.17\left(\frac{\sigma_{UTS}}{E}\right)^{0.832} N_f^{-0.09} + 0.0266\varepsilon_f^{0.155}\left(\frac{\sigma_{UTS}}{E}\right)^{-0.53} N_f^{-0.56} \quad (2\text{-}10)$$

The above equation has been reported to fit best for steel material.

ii. *Uniform materials method*

Bäumel and Seeger introduced the uniform material law in [36]. They proposed different equations for steel and aluminium alloys. For unalloyed and low-alloy steels, as:

$$\frac{\Delta\varepsilon}{2} = 1.50\frac{\sigma_{UTS}}{E}\left(2N_f\right)^{-0.087} + 0.59\varphi\left(2N_f\right)^{-0.58} \quad (2\text{-}11)$$

where

$$\varphi = 1 \; for \; \frac{\sigma_{UTS}}{E} \leq 0.003$$

$$\varphi = 1.375 - 125\frac{\sigma_{UTS}}{E} \; for \; \frac{\sigma_{UTS}}{E} \geq 0.003$$

and for aluminium and titanium alloys, as:

$$\frac{\Delta\varepsilon}{2} = 1.50\frac{\sigma_{UTS}}{E}\left(2N_f\right)^{-0.087} + 0.59\varphi\left(2N_f\right)^{-0.58} \quad (2\text{-}12)$$

iii. *Roessle-Fatemi's hardness method*

Roessle-Fatemi [37] introduced an estimation method which requires only the hardness and the elastic modulus. In their work, it is reported that for steel, their hardness method provides better results compared to the modified universal slopes method. The equation suggested is:

$$\frac{\Delta\varepsilon}{2} = \frac{425HB + 225}{E}\left(2N_f\right)^{-0.09} \frac{0.32(HB)^2 - 487HB + 19100}{E}\left(2N_f\right)^{-0.56} \quad (2\text{-}13)$$

where HB is the Brinell hardness.

iv. *Mitchell method and modified Mitchell's method*

In 1977, Mitchel *et al.*[38] proposed that $\beta 1$ depends upon σ_{UTS} and that $\beta 2 = -0.6$ for ductile materials and $\beta 2 = -0.5$ is appropriate for strong alloys. They proposed the below equation:

$$\frac{\Delta\varepsilon}{2} = \frac{\sigma_B + 335}{E}\left(2N_f\right)^{\frac{1}{6}log\left(\frac{\sigma_{UTS}+335}{\sigma_{UTS}}\right)} + ln\left(\frac{100}{100 - RA}\right)\left(2N_f\right)^{\beta 2} \quad (2\text{-}14)$$

Park and Song [34] modified Mitchell's method and proposed a new equation, which is now commonly referred to as modified Mitchell's method, as:

$$\frac{\Delta\varepsilon}{2} = \frac{\sigma_B + 335}{E}\left(2N_f\right)^{\frac{1}{6}log\left(\frac{\sigma_B+335}{0.446\sigma_B}\right)} + ln\left(\frac{100}{100 - RA}\right)\left(2N_f\right)^{-0.664} \quad (2\text{-}15)$$

Modified Mitchell's method is found to be appropriate for aluminium and titanium alloys.

v. *Medians method*

Maggiolaro and Castro [35] proposed the median method, which requires only the tensile strength. They are defined as:

$$\frac{\Delta\varepsilon}{2} = 1.5\frac{\sigma_{UTS}}{E}\left(2N_f\right)^{-0.09} + 0.45\left(2N_f\right)^{-0.59} \quad (2\text{-}16)$$

for steel materials

$$\frac{\Delta\varepsilon}{2} = 1.9\frac{\sigma_{UTS}}{E}\left(2N_f\right)^{-0.11} + 0.28\left(2N_f\right)^{-0.66} \quad (2\text{-}17)$$

for aluminium alloys.

2.4.3 Creep damage

Considerable progress has been made in creep damage modelling using CDM, but they require numerous calibrated material parameters for accurate results in addition to the high computational cost. Hence, the high-temperature design codes generally use simplified rule-based approaches, though they provide conservative results. The most prominent ones are presented here.

2.4.3.1 Time Fraction

ASME and RCC-MR recommend the use of Time Fraction (TF) rule for the estimation of creep damage. The TF rule for the creep damage per cycle is given by:

$$d_C^{TF} = \int_0^{t_h} \frac{dt}{t_f(\sigma, T)} \tag{2-18}$$

where t_f is the creep rupture time at failure. It is a function of stress and temperature. dt is the time increment and t_h is the dwell time.

2.4.3.2 Ductility Exhaustion

Creep damage is calculated using the Ductility Exhaustion (DE) method while using the R5 design code. The creep damage is calculated by:

$$d_C^{DE} = \int_0^{t_h} \frac{\dot{\bar{\varepsilon}}_C}{\bar{\varepsilon}_C(\dot{\bar{\varepsilon}}_C,\ T)} dt \tag{2-19}$$

where $\dot{\bar{\varepsilon}}_C$ is the instantaneous creep strain rate and $\bar{\varepsilon}_C(\dot{\bar{\varepsilon}}_C,\ T)$ is the corresponding uniaxial creep ductility at temperature, *T*, as a function of the creep strain rate.

2.4.3.3 Stress Modified Ductility Exhaustion

Spindler M. W. introduced the Stress Modified Ductility Exhaustion (SMDE) method in his work [39]–[41]. Compared to the DE method, where the creep damage is calculated by treating the ductility as a function of strain rate and temperature, in SMDE the creep damage is calculated by treating creep damage as a function of strain rate, temperature and stress. The creep damage is calculated by:

$$d_C^{SMDE} = \int_0^{t_h} \frac{\dot{\bar{\varepsilon}}_C}{\bar{\varepsilon}_C(\dot{\bar{\varepsilon}}_C,\ \sigma,\ T)} dt \tag{2-20}$$

where $\dot{\bar{\varepsilon}}_C$ is the instantaneous creep strain rate and $\bar{\varepsilon}_C(\dot{\bar{\varepsilon}}_C,\ \sigma,\ T)$ is the creep ductility at temperature, *T*, as a function of both creep strain rate and stress.

2.4.4 Creep-fatigue interaction diagram

The principle of damage diagram is that fatigue damage and creep damage can be calculated separately and then summed to obtain the total damage [42]. There is no single accepted damage diagram. The selection of the damage diagram depends upon factors such as the design standard followed and the material under consideration. The two most common damage diagrams are introduced in the following section.

2.4.4.1 Bi-linear damage diagram

ASME and RCC-MR use a bi-linear interaction diagram. It can be represented using the equation:

$$\varphi_f + \varphi_c \leq D \tag{2-21}$$

When $\varphi_f = 1, \varphi_c \to 0$ and when $\varphi_c = 1, \varphi_f \to 0$ and for all other locations, the sum of creep and fatigue damage should be under *D* to be considered safe for service. ASME has defined varying acceptable damage envelopes for 304 and 316 steels; 2 ¼ Cr1Mo and NiFeCr alloy 800H; and 9Cr1MoV (T91), as shown in Figure 2-8. RCC-MR, on the other hand, recommends

the use of the same bi-linear curve with an intersection at (0.3, 0.3) for 304, 316, 316L, 316(N), 316H, alloy 800 and T/P91.

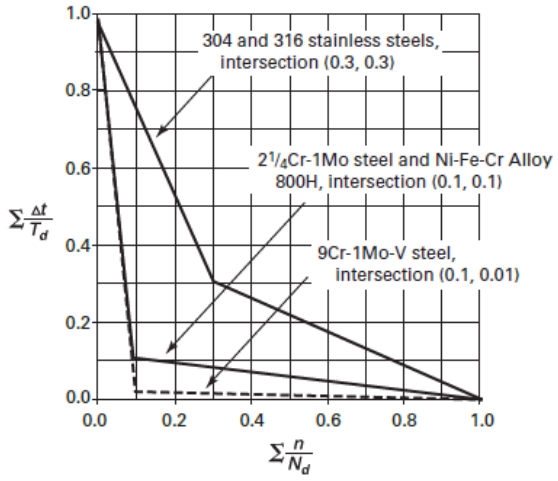

Figure 2-8 Creep-fatigue damage envelope-ASME [43].

2.4.4.2 Linear damage diagram

R5 recommends the use of a linear damage diagram, where the damage *D* defined in Equation (2-21) is equal to 1. If the loading conditions assessed gives a combined damage which falls within this envelope, then crack initiation will be avoided. Whereas if the combined damage is outside this envelope, R5 recommends conducting creep-fatigue crack growth calculations.

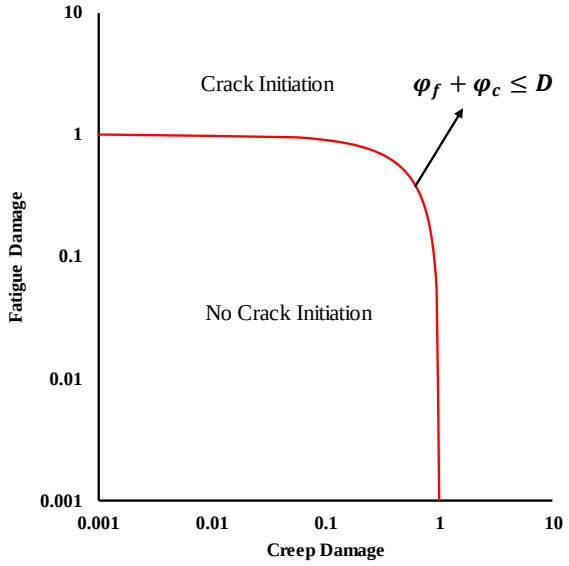

Figure 2-9 Creep-fatigue damage envelope-R5 [44].

2.5 Introduction to weldment

As this thesis aims to evaluate the structural integrity with an emphasis on welds, an introduction to welds is presented in this section. In large plants, welding is the preferred and practical process for joining piping and vessels. American Welding Society (AWS) has defined welding as "*A joining process that produces coalescence of materials by heating them to the welding temperature, with or without the application of pressure or by the application of pressure alone, and with or without the use of filler metal*"[45].

For services at elevated temperatures, it has been reported that the performance of welds is often the life-limiting factor [46], [47]. Broadly, weldments contain three region, a) Parent Metal (PM) - this is the region next to the joint within the parent material that is not affected by the welding process; b) Weld Metal (WM) – this is the region within the weldment that consists of the weld metal; and c) Heat Affected Zone (HAZ) - this is the region within the PM near the WM whose microstructure and mechanical properties are altered due to the heat of welding that approaches the melting temperature. The presence of different material zones with different properties and varying weld geometries makes the prediction of weld behaviour difficult.

A schematic representation of the different subzone within the HAZ due to multiple weld pass with their respective phase transformation for P91 is provided by Khajuria A. *et al.* in [48], Figure 2-10. It can be observed that within the small region of the HAZ, the microstructure varies considerably leading to the formation of Coarse-Grained HAZ (CGHAZ), Fine-Grained HAZ (FGHAZ) and Inter-Critical HAZ (ICHAZ).

- The CGHAZ is the region within the PM, adjacent to the WM. Within this region, the material experiences a temperature well above AC_3. Complete transformation to austenite occurs here and the precipitates are dissolved [49], [50].

- The FGHAZ is formed further away from the WM. Within this region, the material experiences temperature above AC_3 so that austenite transformation occurs but the temperature is not high enough to dissolve all the precipitates. This restricts the free growth of austenite grains[49], [50].

- The material within the ICHAZ experiences temperature above AC_1 but below AC_3. Within this region some austenite may be formed and very little, if any, of the precipitate is dissolved. A low carbon austenite is formed in this region[49], [50]. The For P91, creep cracks, commonly known as Type IV cracking have been reported to initiate from the ICHAZ [51].

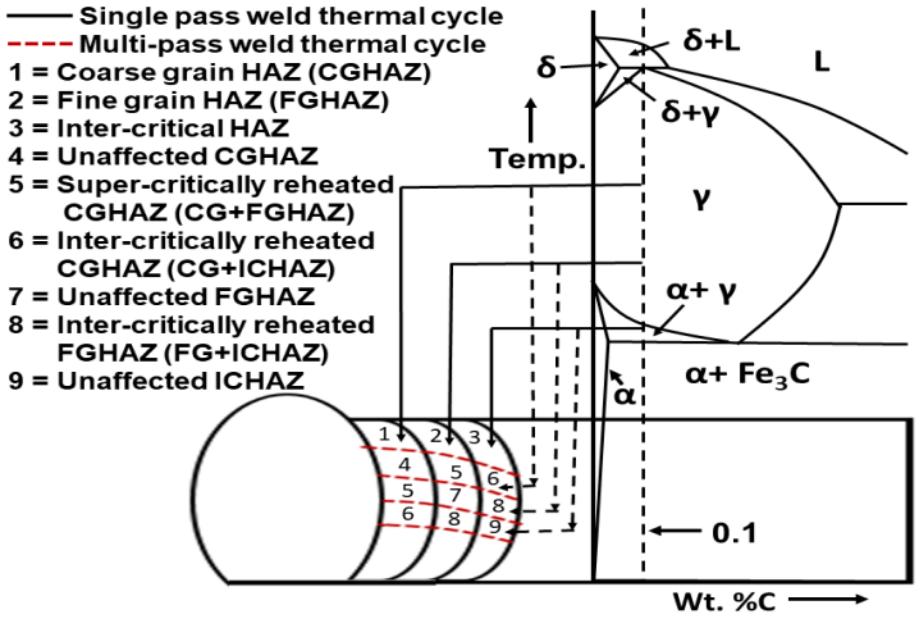

Figure 2-10 Evolution of different regions within the HAZ [48].

The presence of various zones within a weldment subjected to high temperature leads to a complexity in the creep behaviour [52]. Also, the microstructural changes that occur during welding affect the LCF behaviour [53]. In many circumstances, it has been reported that welds tend to perform worse than the parent material with respect to creep [54]. The difference in the properties of the PM, WM and HAZ, creates a strain concentration which leads to a metallurgical notch such that the creep properties of the welded joint may be poor when compared to PM [55]. Non-uniform stress and strain are developed within the zones with time due to creep. If the WM exhibits a higher strain rate compared to the PM, it is called creep-soft weld. On the other hand, if the WM exhibits a lower creep strain rate compared to the PM it is termed as creep-hard weld [56]. Rivolta B. *et al.* [57] in their study on P91 welded plates have reported that even for tensile properties similar to that of the PM, the presence of weld reduced the creep life. Tabuchi M. and Takahashi Y. [58] analysed around 370 points of creep rupture data for modified 9Cr-1Mo steel welded joints and reported that the creep strength of

the welded joints was lowered by a factor of 0.75 compared to the PM at 600 ºC. Mathew M.D. *et al.* [55] investigated the creep strength reduction factor for SS316L(N) welds at 600 ºC and 650 ºC. For both the temperatures, the rupture strength for the weld joint and the WM was lower than that of the PM. An interesting outcome of the research was that at 650 ºC, the difference in the rupture strength of the weld joint and WM decreased with an increase in the rupture life. Kumar D.H. and Reddy A.S. [59] compared the creep rupture strength of SS316L(N) weld joints produced by single pass activated TIG and multi-pass activated TIG. Joints manufactured from both these process showed lower creep rupture life compared to the base material.

Spigarelli S. and Quadrini E. have discussed the microstructure of the different zones in a P91 weldment and presented Transmission electron microscopic (TEM) studies in [60], Figure 2-11. A typical P91 material consist of tempered martensite with $M_{23}C_6$ and MX. They have superior creep properties but the within the HAZ, a large amount of martensite with undissolved precipitates is observed. As a results, on recrystallization a soft fine grained structure is produced which is less creep resistant compared to the PM.

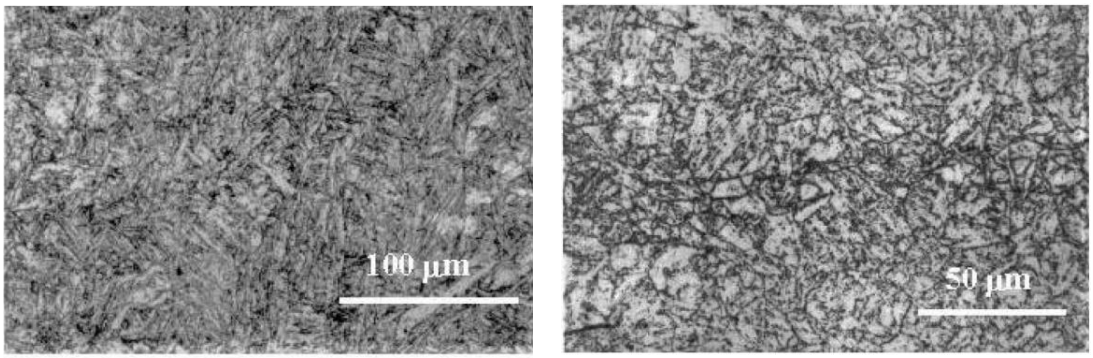

a) **b)**

Figure 2-11 Microstructure of the a) WM [60]; b) Fine-grained intercritical zone [60].

2.6 Design codes and procedures for assessing structural integrity under high temperature

The current structural assessment codes such as the R5 and ASME NH do not have a uniform approach in their methodologies especially in their guidance for the creep and fatigue damage calculation of welds [55]. Though conservative, the design codes provide a safe assessment

route for components operating at high temperature. With respect to creep-fatigue damage assessment both the codes agree that identifying the structural response at steady-state is key, but the steps undertaken are different. A brief discussion on the R5 and ASME NH steps are included in this section.

2.6.1 R5 assessment procedure for the high-temperature response of structure

R5 and R6 are two standardized procedures developed by the former Central Electricity Generating Board (CEGB) and consequently absorbed within the Nuclear Electric plc. to perform integrity assessment. R6 deals with components operating below the creep range and is now well established. On the other hand, R5 provides a comprehensive assessment procedure for the high-temperature response of structures [61]. R5 identifies various failure mechanisms such as instantaneous plastic collapse, creep rupture, ratcheting, enhanced creep deformation, crack initiation and crack propagation due to creep-fatigue interaction and provides step-by-step assessment for all of them [44], [62], [63].

Initially, R5 was written in 7 volumes, but recently, volumes 2 and 3 were combined into a single procedure. Similarly, volumes 4 and 5 were combined to a single procedure reducing the number of volumes to five as below:

Volume 1: Overview
Volume 2/3: Creep-fatigue initiation procedure for defect-free structures
Volume 4/5: Procedures for assessing defects under creep and creep-fatigue loading
Volume 6: Assessment procedure for dissimilar metal welds
Volume 7: Behaviour of similar welds: guidance for steady creep loading of CrMoV pipework components

Discussions within this section will be limited to volume 2/3 which deals with the evaluation of steady-state stress and strain by a simplified technique based on elastic stress analysis. Volume 2/3 provides guidance against crack initiation only and does not cover crack propagation. It consists of 18 steps. A very brief introduction to them highlighting the major aspects is given below.

Step 1. Resolve load history into cycle types

In this step, the operational history is broken up into a well-defined number of different service cycles.

Step 2. Perform elastic stress analysis

Elastic stress analysis is performed. This helps in identifying the critical regions within the structure. Zones with maximum stress levels, stress range etc. are selected as critical zones. Elastic analysis can be easily carried out by Finite Element Methods (FEM).

Step 3. Demonstrate sufficient margins against plastic collapse

This step is related to ensuring that the component does not collapse with the application of the first load. It should be ensured the calculated linear stress is not so huge to induce a very large plastic deformation before steady-state is achieved.

Step 4. Determine whether creep is significant

For the considered loading condition, before getting into complex creep calculations, the possibility of significant creep should be checked. It is recommended that if the sum of the ratios of the hold time t to the maximum time t_m, at the maximum temperature in the dwell T_{ref} for the total number of cycles n_j of each cycle type j, is less than one, then the effect of creep may be ignored.

$$\sum_j n_j \left[t/t_m\left(T_{ref}\right) \right]_j < 1 \tag{2-22}$$

Step 5. Demonstrate that creep rupture endurance is satisfactory

Using rupture reference stress the creep rupture is calculated in this step. The creep usage factor, *U*, is then calculated and it should be less than 1

$$U = \sum_j n_j \left[\frac{t}{t_f\left(\sigma^R_{ref}, T_{ref}\right)} \right]_j < 1 \tag{2-23}$$

Step 6. Perform simple test for shakedown and check for insignificant cyclic loading

Within this step, the structure is analysed for ratcheting that may lead to incremental plastic failure. A simple test, which is called as stress linearization method, is carried out to check if the structure is in shakedown. Further, in case the structure exhibits insignificant loading, steps 7-14 may be avoided. For the acceptance of insignificant loading, the following three criteria need to be met:

a) The most severe cycle is within the elastic range of the material.
b) The total fatigue damage for all cycles should be less than 0.05.
c) The cyclic load does not affect the creep behaviour. This is confirmed if the below equation is satisfied.

$$\Delta\bar{\sigma}_{el,max} \leq \sigma_{SS} + \left(K_s S_y\right)_{nc} \tag{2-24}$$

where $\Delta\bar{\sigma}_{el,max}$ is the elastic strain range, σ_{SS} is the steady-state creep stress and $\left(K_s S_y\right)_{nc}$; K_s is the parameter provided by R5 and S_y is the proof stress of the material. "*nc*" refers to values at the non-creep end of the cycle.

Step 7. Perform global shakedown check and calculate cyclic plastic zone size

The structure is assessed for its capability to attain global shakedown or nearly elastic behaviour after the first few cycles of loading. This also helps in confirming that the structure is not subjected to plastic ratcheting or incremental collapse. If it cannot be confirmed that the body is under global shakedown, then it might be necessary to have detailed inelastic analysis to validate the integrity of the structure.

Step 8. Calculate shakedown reference stress, reference temperature and start-of-dwell stress

This step may be further divided into two sequences. The first sequence deals with minimising the shakedown reference stress and the creep rupture damage by optimising the residual stress field while the latter sequence deals with the estimation of the start of dwell stress.

Step 9. Estimate elastic follow-up factor and associated stress drop during creep dwell

During periods of steady operation at high temperature, which is typical of power plants, stress relaxation occurs within the structure with the elastic strains being replaced with creep strains. This process is generally explained using the term "elastic follow-up". The stress relaxation process increases the total strain and can be described by the below equation:

$$\frac{d\bar{\varepsilon}_{ec}}{dt} + \frac{Z}{\bar{E}}\frac{d\bar{\sigma}}{dt} = 0 \tag{2-25}$$

where $\bar{\varepsilon}_{ec}$ is the equivalent creep strain, $\bar{E}$ is the equivalent Young's modulus, υ is the Poisson's ratio, $\bar{\sigma}$ is the equivalent stress and Z is the elastic follow-up factor.

There are three options provided for the estimation of *Z*. a) assume $Z = \propto$, in this case, the stress relaxation during the dwell is ignored and provides conservative results for creep damage. However, the stress relaxation should be considered while evaluating the total strain range; b) the elastic follow up factor may be taken as 3, provided the structure is isothermal and the primary loads are small compared to the secondary loads; c) the final option is to calculate *Z* using an inelastic analysis. R5 provides advice on how to simplify the inelastic process so that alternating plasticity and creep need not be considered.

Step 10. Calculate the total strain range

The total strain range can be obtained by summing the maximum elastically calculated stress range calculated in step 2 with the stress relaxation drop. This can be calculated using the following equation:

$$\Delta\bar{\sigma}_{el,r} = \Delta\bar{\sigma}_{el} + \Delta\sigma_{rD} \tag{2-26}$$

If the effects of creep are negligible, then Equation (2-26) reduces to $\Delta\bar{\sigma}_{el,r} = \Delta\bar{\sigma}_{el}$. If it is considered that the material follows the Ramberg-Osgood (RO) relation, then the total stress range is initially calculated, which is in turn used to calculate the total strain range.

Step 11. Check limits on cyclically enhanced creep and calculate creep usage factor

The previous steps confirm that there is no plastic ratcheting within the structure. Within this step, the possibility of creep-ratcheting by the accumulation of creep strain due to cyclic loading is evaluated. A creep usage factor "*W*" is introduced for this,

$$W = \sum_{n} n_j \left[\frac{t}{t_f\left(\sigma^s_{ref}, T^s_{ref}\right)}\right]_j < 1 \tag{2-27}$$

where σ^s_{ref} is the shakedown reference stress.

$$\begin{gathered}\sigma^s_{ref} = \left\{Y - 2\sqrt{Y(1-X)} + 1\right\} S_y \text{ for } Y(1-X) < 1 \\ \sigma^s_{ref} = XYS_y \text{ for } Y(1-X) \geq 1\end{gathered} \tag{2-28}$$

X and *Y* are load parameters such that

$$X = \sigma_{ref}/S_y \quad Y = Q_{range}/S_y$$

where σ_{ref} is the primary load reference stress and Q_{range} is the maximum elastically calculated range of the linear thermal stress.

Step 12. Summarise assessment parameters

The parameters required for the basic structural integrity of the component has been identified in the previous steps. They are as summarised below:

a) r_p- The cyclic plastic zone size; Calculated in Step 6 or 7
b) σ_0- The start of dwell stress; Calculated in Step 8
c) T_{ref}^{s}- The shakedown reference temperature; Calculated in Step 8
d) $\Delta\sigma'$- The stress drop during creep dwell; Calculated in Step 9
e) Z - The elastic follow-up factor; Calculated in Step 9
f) $\Delta\bar{\varepsilon}_{Total}$- The total strain range; Calculated in Step 10
g) W- The creep usage factor; Calculated in Step 11

Step 13. Treatment of weldments

R5 provides specific advice for the treatment of welds. This is dealt with in detail in Section 2.6.1.1 of this thesis.

Step 14. Calculate fatigue damage per cycle

The total strain range calculated in the previous steps is used to assess the fatigue damage per cycle, d_f.

$$d_f = 1/N_0 \tag{2-29}$$

where N_0 is the number of cycles to initiate a crack of size a_0. N_0 is calculated by the following steps:

a) The relevant fatigue endurance data is collected as an initial step
b) The obtained data is partitioned into curves that indicate the number of cycles for nucleation and growth, as:

$$ln(N_i) = ln(N_\lambda) - 8.06N_\lambda^{-0.28} \tag{2-30}$$

$$N_g = N_\lambda - N_i \tag{2-31}$$

c) The number of cycles for the crack to grow from a_i to a_o is calculated as:

$$N'_g = MN_g \tag{2-32}$$

Step 15. Calculate creep damage per cycle

Two possibilities are considered in this step, based on whether insignificant or significant cyclic loading has been established in step 6. If insignificant cyclic loading is confirmed, then creep damage d_c is calculated as

$$d_c = t_h / t_f(\sigma_{ss}) \tag{2-33}$$

where t_h is the duration for creep dwell and $t_f(\sigma_{ss})$ is the rupture time of the material at steady-state creep stress. For significant cyclic loading conditions, the creep damage per cycle is calculated using the DE method introduced in Section 2.4.3.2.

In cases where the creep damage during the transition state is significant, it should be separately calculated and added to the steady-state creep damage.

Step 16. Calculate total damage

The total damage in R5 is assessed using the Linear Damage Summation Rule (LDSR).

$$D = D_f + D_c \tag{2-34}$$

where

$$D_f = \sum_j \frac{n_j}{N_{0j}} = \sum_j n_j d_{fj} \tag{2-35}$$

and

$$D_c = \sum_j n_j d_{cj} \tag{2-36}$$

D is the total damage, D_f is the total fatigue damage, D_c is the total creep damage and n_j is the number of the loading cycle. All notations with subscript "j" indicate the respective value at j^{th} cycle. For cases with $D < 1$, the structure is considered to be free of any crack initiation risk.

2.6.1.1 Modifications on R5 assessment for Weldments

R5 has categorised weldments into three main types as presented in Figure 2-12. Weldments are also classified as dressed (profiled) and undressed (as-welded) weldments, and separate advice on the assessment is provided within R5.

- Type 1 - Full penetration butt weldment transverse to the main loading direction.
- Type 2 - Full penetration T-butt or fillet weldment transverse to the main loading direction.
- Type 3 - Partial penetration T-butt or fillet weldment transverse to the main loading direction.

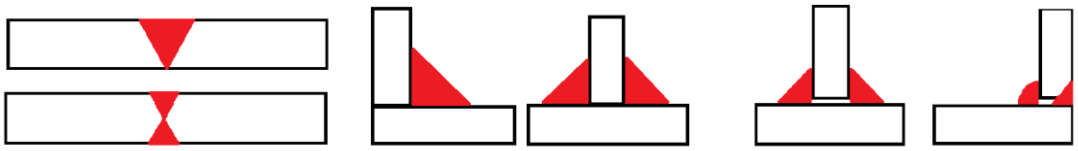

a) b) c)

Figure 2-12 Classification of welds in R5 a) Type 1, b) Type 2, and c) Type 3.

For creep-fatigue crack initiation assessment in weldments, the structure is considered to be of the PM alone and a Fatigue Strength Reduction Factor (FSRF) is used to account for the weldment behaviour. The FSRFs are obtained by tests done on weldments and comparing their endurance with the PM. Table 2-1 indicates the recommended FSRF for the different weld types.

Table 2-1 FSRFs in the current R5 Volume 2/3 for austenitic steel weldments.

Weldment Type	FSRF	
	Dressed	Undressed
1	1.5	1.5
2	1.5	2.5
3	N/A	3.2

For both dressed and undressed weldments, the FSRF is used to enhance the strain range. The difference between the analysis route for dressed and undressed weldments is in determining the start of dwell stress for creep relaxation. For undressed welds, linearized stress and strain

which is modified using FSRF is used to determine the start of dwell stress, on the other hand, for dressed welds peak elastic stress is used to determine the start of dwell stress.

It has been identified that the FSRF method is overly conservative, especially for undressed weldments. Hence, a new approach is proposed within the R5. The new approach has a common methodology for both dressed and undressed weldments. It separates the existing FSRF into Weld Strain Enhancement Factor (WSEF) and Weld Endurance Reduction (WER), Figure 2-13.

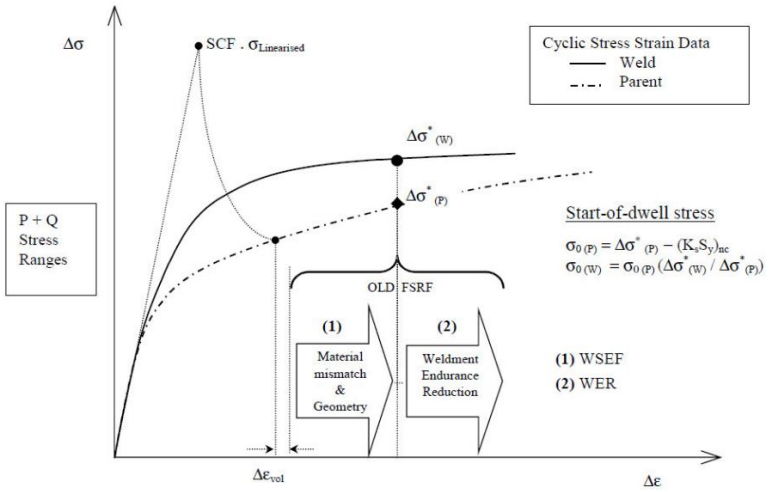

Figure 2-13 Schematic to split the FSRF into WSEF and WER for a simple cycle [44].

The same weldment database which is used to determine the FSRF is used for the determination of WSEF also. However, WSEF is derived relative to the reduced endurance curve. With respect to the fatigue damage assessment, both the current and proposed methodologies are quite similar. A combination of WER and WSEF is used to predict the fatigue damage in the proposed route, which corresponds to the FSRF in the current route. The first step involves the determination of the elastic-plastic strain range. WSEF is applied to it which is then combined with the WER to estimate the number of cycles for crack initiation due to fatigue damage. With respect to creep damage assessment, the proposed route uses WSEF only to evaluate the start of dwell stress resulting in a less conservative creep damage. obtained. The WSEF includes the geometric strain enhancement due to both the geometry and the material mismatch in the stress-strain properties of the materials of the weld [64].

Table 2-2 WSEFs applied to mean base-line fatigue data for austenitic weldments.

Weldment Type	WSEF
1	1.16
2	1.23
3	1.66

Volume 6 within the R5 provides guidance for damage assessment for dissimilar metal welds. It should be noted that the material, weld types etc. for which this assessment procedure can be used are limited. The material combinations covered include joints between 2¼Cr1Mo and austenitic stainless steels with austenitic or nickel-based weld metal, and joints between 9Cr and austenitic stainless steel with Inconel weld metal. The methodology has been validated by several case studies within the R5. Nevertheless, it should be noted that there are certain limitations also. The creep rupture strength data available is limited to 2¼Cr1Mo:Type 316 and 9Cr1Mo:Type 316 parent material combinations. For 2¼Cr1Mo and austenitic stainless steel dissimilar metal welds, rupture data available is limited to stress between 150 MPa to 25 MPa, and for temperature equal to or over 540 ºC. For fatigue assessment, the availability of cross weld fatigue endurance data for dissimilar metal welds is limited.

2.6.2 ASME BPVC section III subsection NH

Similar to the R5 which is used within the UK nuclear energy sector, ASME is a globally accepted code which is widely used in countries such as the USA and Canada. Based on the material and the operating temperature ASME recommends the use of either ASME Section III Subsection NB or ASME Section III Subsection NH. For instance, for austenitic stainless steel, at temperatures over 427 ℃ and for 2.25 Cr-1Mo and Mod. 9Cr-1Mo, at temperatures over 371 ℃, the use of ASME Section III Subsection NH is recommended. A pictorial representation is provided in Figure 2-14.

For temperatures where the creep is significant ASME NH recommends that the design analysis should take into consideration effects such as a) ductile rupture from short holding; b) creep rupture from long holding; c) creep-fatigue damage and d) distortion due to an incremental collapse and ratcheting. The loading categories include the design load, service load (from level A to D) and finally the test loads.

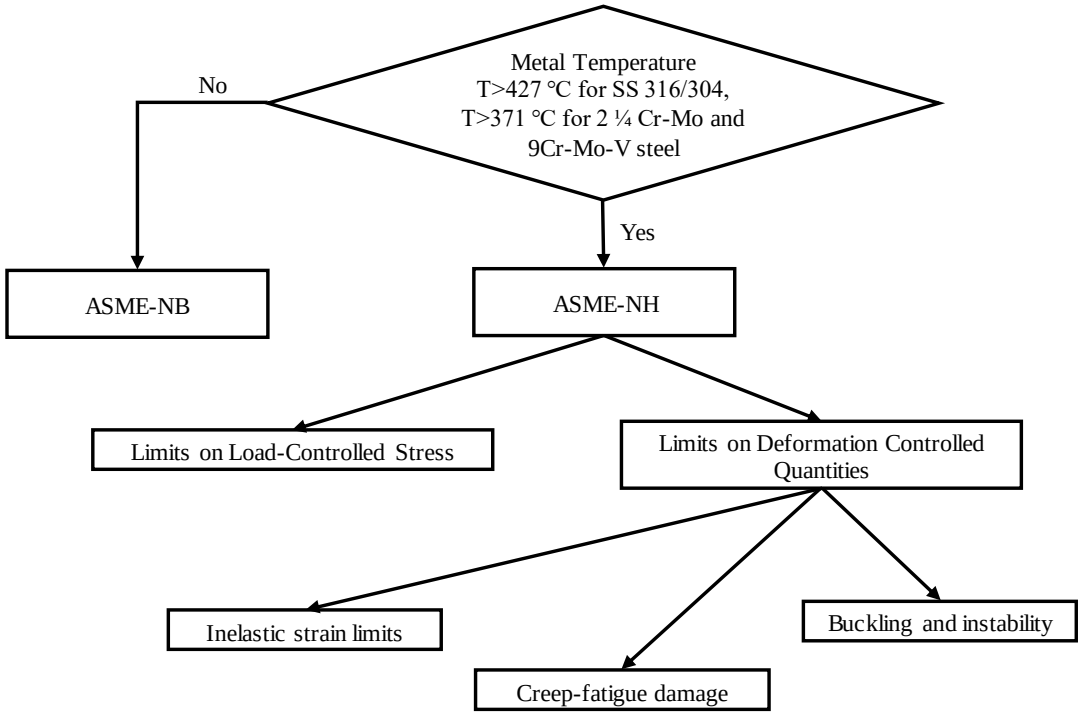

Figure 2-14 The design checks recommended by ASME [65].

The check for structural integrity at high temperature can be broadly classified as below [66].

a) Load controlled stress
b) Total accumulated inelastic strain
c) Creep fatigue damage
d) Buckling instability

Load controlled stress

ASME NH lists the service loads as A - normal operation, B - moderate incidents, C - infrequent incidents and D - limiting faults. The stresses are categorised as primary membrane stress P_m , local primary membrane stress P_L and primary bending stress P_b, secondary stress Q and peak stress F. Table 2-3 indicates the primary stress limit that needs to be satisfied where S_m is the time-independent stress limit, S_{mt} is the long-time service at an elevated temperature stress limit, and S_t is a temperature and time-dependent stress limit. S_u is the tensile strength at a given temperature. K is the section factor for the cross-section considered

and K_t is the factor accounting for the reduction in bending stress due to creep. S_r is the minimum stress-to-rupture strength.

Table 2-3 Primary stress limits for service loads A-D [66].

Design Condition	Service Load A and B	Service Load C	Service Load D
Membrane	Membrane	Membrane	Membrane
$P_m \leq S_o$	$P_m \leq S_{mt}$	$P_m \leq \begin{Bmatrix} 1.2\ S_m \\ S_t \end{Bmatrix}$	$P_m \leq \begin{Bmatrix} 2.4\ S_m \\ 0.7\ S_u \\ 0.67\ S_r \\ 0.8\ RS_r \end{Bmatrix}$
Membrane+Bending	Membrane+Bending	Membrane+Bending	Membrane+Bending
$P_L + P_b \leq (1.5)S_o$	$P_L + P_b \leq KS_m$ $P_L + P_b/K_t \leq S_t$	$P_L + P_b \leq 1.2\ KS_m$ $P_L + P_b/K_t \leq S_t$	$P_L + P_b \leq \begin{Bmatrix} 3.6\ S_m \\ 1.05\ S_u \end{Bmatrix}$ $P_L + P_b/K_t \leq \begin{Bmatrix} 0.67\ S_r \\ 0.8\ RS_r \end{Bmatrix}$

It should be noted that for weldments S_{mt} should be taken as the lower value between S_{mt} and 0.8 S_r . R where R is the ratio of the WM creep rupture strength to the PM creep rupture strength.

Limits for deformation and strain

If the effect of creep is significant, ASME NH recommends using detailed inelastic analysis. Nevertheless, ASME NH lists a series of elastic and simplified in-elastic methods which may be used instead to give results within a conservative band. At any point within the structure experiencing high temperature, the inelastic strain has certain restrictions such as:

(a) The strains averaged through the thickness cannot exceed 1%.
(b) Strains at the surface due to an equivalent linear distribution of a strain through the thickness cannot exceed 2%.
(c) Local strains at any point cannot exceed 5%.

ASME NH defines elastic analysis tests A-1, A-2 and A-3 to check for the inelastic strain limits. If any of them are satisfied then it is considered that the strain limits are satisfied. Tests A-1 and A-2 are expressed using the parameters X and Y where:

$$X = \frac{(P_L+P_b/K_t)_{max}}{S_{y,average}} \text{ and } Y = \frac{\Delta Q_{max}}{S_{y,average}} \quad (2\text{-}37)$$

$(P_L+P_b/K_t)_{max}$ is the maximum value of the primary stress intensity corrected for bending. $S_{y,average}$ is the average of the maximum and minimum wall S_y values. ΔQ_{max} is the maximum range of secondary stress intensity.

For A-1 to be satisfied

$$X + Y \leq {S_a}/{S_y} \quad (2\text{-}38)$$

where S_a is the lesser value of $1.25S_t$ and the average of the two S_y values associated with the maximum and minimum wall temperature.

For A-2 to be satisfied

$$X + Y \leq 1 \quad (2\text{-}39)$$

for cycles during which the average wall temperature at one of the stress extremes defining ΔQ_{max} is below the appropriate temperature.

For A-3 to be satisfied

The process for A-3 is a little more elaborate considering the limits of NB-3222.2, NB-3222.3, and NB-3222.5, as defined in ASME NH, are to be met along with the requirements defined in Equation (2-40) – Equation (2-42):

$$\sum_i \frac{t_i}{rt_{id}} \leq 0.1 \quad (2\text{-}40)$$

$$\sum_i \in_i \leq 0.2\% \quad (2\text{-}41)$$

(2-42)

$\Delta(P_L + P_b)_{max} + \Delta[Q]_{max} \leq 3\bar{S}_m$; where $3\bar{S}_m$ is the lesser of $3S_m$ and $3\bar{S}_m$

t_i is the total service time at the elevated temperature, t_{id} is the maximum allowable time, $\in_i$ is the creep strain at a stress level of $1.25S_y$; and $3\bar{S}_m = 1.5S_m + S_{rh}$ when only one extreme of stress difference occurs at a temperature above those covered by ASME NB or $3\bar{S}_m = S_{rH} + S_{rL}$ when both extremes of stress difference occur at a temperature above those covered by ASME NB.

When the elastic analysis method does not satisfy the limits or if they are highly conservative, simplified inelastic analysis method can be used. Similar to the elastic analysis method, this is also done using a series of test numbered B-1, B-2 and B-3. Before explicating applying them, there are a list of conditions to be satisfied, as listed below:

a) Test B-1 is applied for structures where the peak stress is negligible. Test B-2 can be applied for any structure and loading and is more conservative.
b) The individual cycle as defined in the Design Specification cannot be split into sub-cycles. The transients conditions should be uniformly distributed along the lifetime of the plant for strain evaluation unless otherwise specified.
c) As an alternate to B-1 and B-2, the inelastic strains may be evaluated separately by B-3 or using detailed inelastic analysis but the resulting sum of inelastic strains must be within the acceptable limit.
d) Secondary stresses with elastic follow-up are classified as primary stresses for evaluations.
e) The time used for B-1 and B-2 to enter the isochronous curve shall always sum to the entire life.
f) For B-1 and B-2, the S_y in the definition of X and Y is replaced by S_{yL} which is the lower of the wall averaged temperatures for the stress extremes defining the secondary stress.
g) For B-3, X and Y are calculated for the cold and hot ends using S_{yL} and S_{yH}. S_{yH} is the higher of the wall temperature for the stress extreme defining the secondary stress.
h) The wall membrane forces can be conservatively included as axisymmetric forces.

7For test B-1 and B-2

These tests apply to check the strain limits when the wall temperature at one of the stress extremes defining the secondary stress intensity is below the applicable temperature. The effective creep stress is determined as $\sigma_c = Z.S_{yL}$ and the creep strain is determined as 1.25 σ_c. The parameter *Z* is obtained from Figure 2-15 for B-2 and Figure 2-16 for B-1 and B-3.

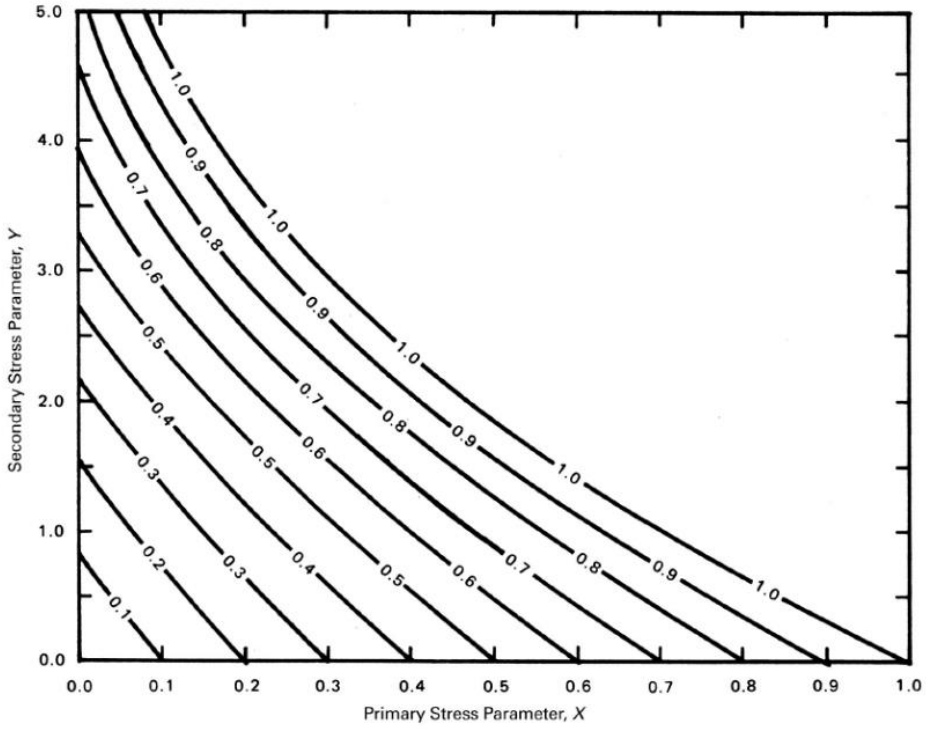

Figure 2-15 Effective creep stress parameter Z for Test B-2 [43].

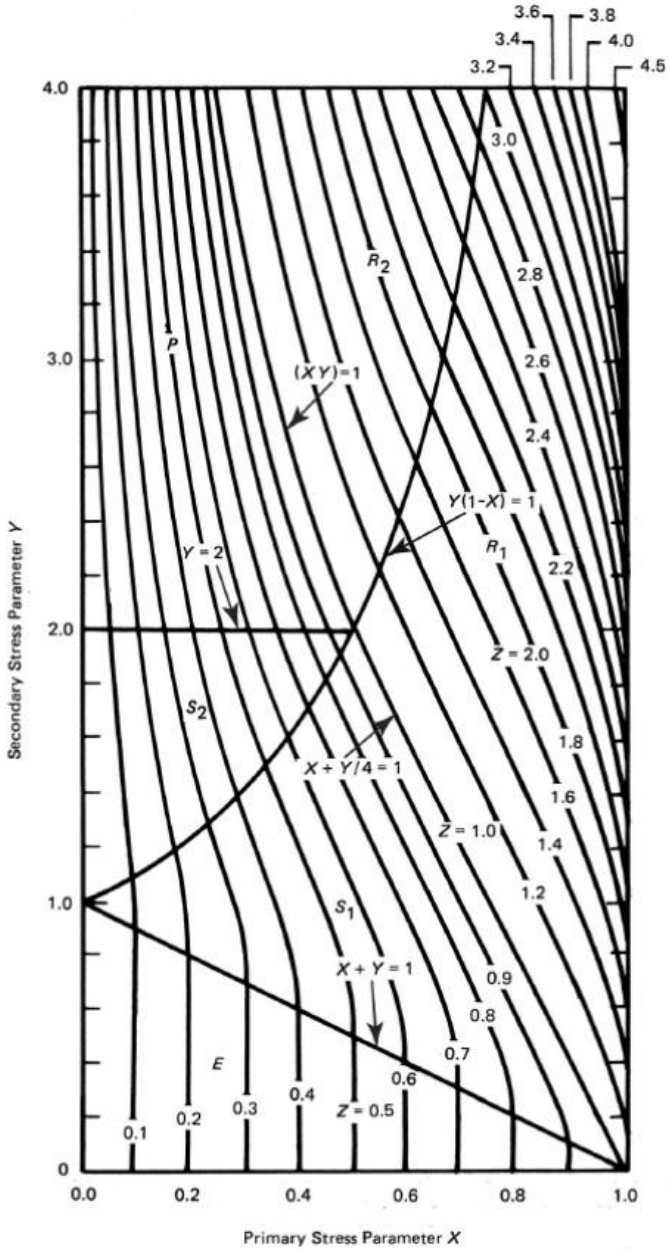

Figure 2-16 Effective creep stress parameter Z for Test B-1 and B-3 [43].

For test B-3

Test B-3 applies to region R1 and R2 indicated in Figure 2-16 or to reduce the conservatism in the other regions. While checking the strain limits, the resulting plastic ratchet strains and the enhanced creep strains due to creep relaxation must be added to the strains obtained from test B-1 or B-2.

Creep-fatigue damage evaluation

The total damage creep-fatigue damage due to the combined service level loads A, B and C should satisfy the below relationship:

$$\sum_{j=1}^{p}\left(\frac{n}{N_d}\right)_j + \sum_{k=1}^{q}\left(\frac{\Delta t}{T_d}\right)_k \leq D \tag{2-43}$$

where D is the total creep-fatigue damage; $(N_d)_j$ is the number of designed allowable cycles for cycle type j corresponding to the maximum temperature occurring during the cycle; $(T_d)_k$ is the allowable time duration for given stress and the maximum temperature at the point of interest and occurring during the time interval k.

For the elastic analysis method, the fatigue damage is determined using the material's design curve which uses the total strain range. The total strain range is calculated as:

$$\epsilon_T = K_v \Delta\epsilon_{mod} + K\Delta\epsilon_c \tag{2-44}$$

where K is the local geometric concentration factor, K_v is the multiaxial plasticity and Poisson adjustment ratio, $\Delta\epsilon_c$ is the creep strain increment, $\Delta\epsilon_{mod}$ is the modified maximum equivalent strain range and ϵ_T is the total strain range. The detailed procedure for calculating $\Delta\epsilon_{mod}$ is given in Section NH-T-1432.

The creep damage may be assessed using a general procedure or an alternate procedure. The alternate procedure has a restriction that it may not be used if $\epsilon_T > 3\bar{S}_m/E$. The general method starts with identifying the total number of hours at elevated temperature (t_H) and the hold temperature (T_{HT}). The average cycle time is then computed for each cycle type. The stress level is obtained from the time-independent isochronous stress-strain curve corresponding to T_{HT}. For the hold temperature, the stress relaxation history is obtained for the average cycle time either considering the isochronous stress-strain curve or the multi-axial stress state. For the transient state, the time, the load control stress intensity and the temperature are then identified. The earlier steps are repeated for different cycle types and superimposed. The stress/temperature-time history envelope obtained is then divided into q

time intervals so as to use Equation (2-43) for evaluating the creep damage. For each time interval, the corresponding allowable time duration is obtained from the stress to rupture curve.

2.6.2.1 Modifications on ASME Assessment for Weldments

In the presence of welds, the allowable number of design cycles used for evaluating fatigue damage and the allowable time duration used for evaluating creep damage are modified. The value of N_d is taken as half the value for the PM. The T_d for the weldment is obtained from the stress to rupture curve that is obtained by multiplying the WRF with the stress to rupture value of the PM. The weld strength reduction factor is provided in Tables NH-1-14.01A-1 - NH-1-14.01E-1 in ASME NH.

2.7 Chapter summary

The fundamental principles of structural integrity at high temperature service, and the major damage mechanisms along with a comprehensive discussion of their classifications and evaluation methods are introduced within this chapter. The introduction of a creep dwell alters the cyclic response of the component with the possible amplification of the existing damage mechanism resulting in creep-fatigue or creep-ratcheting.

Exposure to very high temperature during the welding process causes a variation in the microstructure within the weldment region which leads to a loss of strength predominantly in the HAZ due to the presence of undissolved precipitates, and the formation of multiaxial stress. Both of which has an adverse effects on the safe life of the structure. Though considerable experimental and numerical studies have been undertaken to account for welds in the damage accumulation, the knowledge is limited and requires further research.

The chapter concludes with a step by step overview of the two most common high-temperature service design procedures, R5 and ASME NH. A limitation with them is that the presence of weldments is accounted by introducing considering certain reduction factors and in effect do not consider the complete creep-cyclic plasticity mechanism. This leads to conservatism and early retirement of the structure. Further, due to the lack of experimental data, their use is restricted to a limited number of material and range.

Chapter 3 The Linear Matching Framework

3.1 Introduction

Due to the complexity of obtaining analytical solutions for accessing the structural response, FEA is used to address such challenges. A limitation in using incremental FEA is that it can only predict how the structure will behave under the chosen set of load points, i.e. whether the body will exhibit shakedown behaviour or ratcheting behaviour [67]. The aforementioned strategy does not allow to determine easily the more comprehensive interaction diagrams such as the Bree-diagram [12], which accounts for several cyclic load combinations. Recently, several direct methods have been developed such as 1) Uniform Modified Yield (UMY) surface method [68]; 2) The Elastic Compensation method (ECM) [69]; 3) the Generalized Local Stress-Strain r-node method [70]; 4) the LMM. They use relatively simpler material models such as an EPP or RO model. They are generally based on Koiter's kinematic and/or Melan's static theorems. Direct methods do not require the knowledge of the exact load path as they consider a loading domain that contains all possible path between the extreme load points [71].

The LMM is a numerical procedure that has undergone extensive research and development over a number of years to conduct various types of structural integrity assessments. The theoretical ground for LMM is that the nonlinear elastic behaviour of a structure can be mimicked by a series of linear elastic solutions where the moduli vary spatially and with time [72]. LMM has been developed for limit analysis, shakedown analysis, ratchet analysis, and recently to include steady-state cyclic behaviour with full creep-cyclic plasticity interaction. The LMM subroutines are coded using FORTRAN language to facilitate its use with Abaqus. This implies that users need to have sufficient programming experience to run the analysis efficiently. As this is not the case especially in an industrial environment, to counter this issue, a Graphical User Interface (GUI) and an autonomous Abaqus plug-in have been developed in [73], [74]. The LMM Abaqus user subroutines for limit load analysis and shakedown analysis have been consolidated by the R5 research program of EDF Energy to the commercial standard.

This chapter presents the numerical procedures within the LMM framework. Section 3.2 presents the numerical procedure for the shakedown procedure. Section 3.3 presents the numerical procedure for the ratchet limit analysis, which also includes the DSCA analysis. Section 3.4 details the numerical procedure of eDSCA that deals with the steady-state creep-cyclic plasticity behaviour. Section 3.6 concludes the chapter with a summary.

3.2 Shakedown analysis

Consider an EPP body of volume, V and surface area, S. The structure satisfies the von Mises yield condition. It is subjected to a cyclic thermal load $\lambda\theta(x_i,t)$ within the volume of the structure and a constant mechanical load $\lambda P_i(x_i,t)$ acting over the part of the structure's surface, S_T over the period $0 \le t \le \Delta t$. The remaining surface is constrained with no displacement. λ is the load parameter, which facilitates consideration of various loading history. A linear elastic solution can be obtained for the defined loading condition:

$$\lambda\hat{\sigma}_{ij} = \lambda\hat{\sigma}^{\theta}_{ij} + \lambda\hat{\sigma}^{P}_{ij} \tag{3-1}$$

where $\hat{\sigma}^{\theta}_{ij}$ and $\hat{\sigma}^{P}_{ij}$ are the elastic solutions for loads $\theta(x_i,t)$ and $P_i(x_i,t)$. Equation (3-2) is the general stress solution for a cyclic problem. $\bar{\rho}_{ij}$ is the constant residual stress field in equilibrium with zero surface traction and denotes the residual stress at the beginning and end of the cycle. ρ^{r}_{ij} denotes the changing component of residual stress.

$$\sigma_{ij}(x_i,t) = \lambda\hat{\sigma}_{ij}(x_i,t) + \bar{\rho}_{ij}(x_i) + \rho^{r}_{ij}(x_i,t) \tag{3-2}$$

The changing component of residual stress, ρ^{r}_{ij}, will be 0 for shakedown analysis. The LMM has been developed to calculate the upper bound and lower bound shakedown limit multiplier based on Koither's and Melan's theorem respectively.

Upper bound theorem

The upper shakedown theorem is given by:

$$\lambda_{UB} \cdot \int_V \int_0^{\Delta t} \left(\hat{\sigma}_{ij} \dot{\varepsilon}_{ij}^C\right) dt dV = \int_V \int_0^{\Delta t} \left(\sigma_{ij}^C \dot{\varepsilon}_{ij}^C\right) dt dV \tag{3-3}$$

This is further simplified to:

$$\lambda_{UB} = \frac{\int_V \int_0^{\Delta t} \sigma_y \bar{\dot{\varepsilon}}\left(\dot{\varepsilon}_{ij}^C\right) dt dV}{\int_V \int_0^{\Delta t} \left(\hat{\sigma}_{ij} \dot{\varepsilon}_{ij}^C\right) dt dV} \tag{3-4}$$

where $\dot{\varepsilon}_{ij}^C$ is a kinematically admissible strain rate and $\bar{\dot{\varepsilon}} = \sqrt{2/3 \dot{\varepsilon}_{ij}^C \dot{\varepsilon}_{ij}^C}$ is the effective strain rate. Through an iterative process, a sequence of upper bound values are produced that converges to the least upper bound and satisfies $\lambda_{UB} \geq \lambda_{SD}$, where λ_{SD} is the exact shakedown limit.

Lower bound theorem

While the iterative process is carried out to calculate the upper bound shakedown limit multiplier, a sequence of residual stress field is produced. A lower bound shakedown limit can then be calculated for every integration by scaling the elastic solution so that $\lambda_{LB} \hat{\sigma}_{ij} + \bar{\rho}_{ij}$ satisfies yield at everywhere, such that $\lambda_{LB} \leq \lambda_{SD}$. The lower bound shakedown limit multiplier can be written as:

$$f\left(\lambda_{LB} \hat{\sigma}_{ij}(x_i, t) + \bar{\rho}_{ij}(x_i)\right) \leq 0 \tag{3-5}$$

3.3 Ratchet limit analysis

To address the ratchet limit analysis numerically, we decouple the evaluation of the changing residual stress, $\rho_{ij}^r(x_i, t)$, due to the cyclic part of the load and the constant residual stress. The varying and constant parts of the residual stresses are evaluated separately. Ratchet limit analysis using the LMM consists of two steps. The first step involves an incremental minimization for the evaluation of the cyclic history of residual stress and plastic strain range, this step calculates the history of residual stress field related to the cyclic load and the

corresponding plastic strain ranges associated with the low cycle fatigue assessment. Within the LMM framework, this step is referred to as Direct Steady Cycle Analysis (DSCA). The second step involves a global minimization for the ratchet limit due to an extra constant load, this step locates the ratchet limit as a convectional shakedown limit where the constant residual stress is evaluated and the elastic stress history is augmented by the changes in residual stress calculated in the first step.

Step 1 Numerical procedure for plastic strain range

The residual stress history and the plastic strain due to the cyclic component of the load history are expressed in terms of *N* discrete-time points. For a strictly convex yield condition, the instants when plastic strain occurs are the vertices of the stress history, $\hat{\sigma}_{ij}^{\Delta}(t_n)$ *n*=1 to *N*, where *N* represents the total number of time instants, $t_1, t_2, t_3 \ldots t_N$. Then $\Delta\varepsilon_{ij}^{T} = \sum_{n=1}^{N} \Delta\varepsilon_{ij}^{P}(t_n)$ is the plastic strain accumulated during the cycles; $\Delta\varepsilon_{ij}^{P}$ defines the increment of plastic strain at t_n. We also define $\Delta{\rho_{ij}}_{m}^{n}$ as the evaluated changing residual stress for the n^{th} load instance at the m^{th} cycle of the integration; *n*=1 to *N* and *m*=1 to *M*. The iteration process starts with the first increment where $\Delta{\rho_{ij}}_{1}^{1}$ is solved, due to the elastic solution at first load instance. At the next increment, $\Delta{\rho_{ij}}_{1}^{2}$ is solved, which is due to the previously calculated residual stress and the elastic stress at the second load instance. The incremental iterative process continues until convergence is achieved i.e. $\sum_{n=1}^{N} \Delta{\rho_{ij}}_{m}^{n} = 0$. The constant element of the residual stress is:

$$\rho_{ij}^{r}(0) = \rho_{ij}^{r}(\Delta t) = \bar{\rho}_{ij} \tag{3-6}$$

where

$$\bar{\rho}_{ij} = \sum_{n=1}^{N} \Delta{\rho_{ij}}_{1}^{n} + \sum_{n=1}^{N} \Delta{\rho_{ij}}_{2}^{n} + \cdots + \sum_{n=1}^{N} \Delta{\rho_{ij}}_{M-1}^{n} \tag{3-7}$$

Equation (3-8) gives the converged increment of the plastic strain at t_n,

$$\Delta\varepsilon_{ij}^{P}(t_n) = \frac{1}{2\bar{\mu}_n}\left[\bar{\sigma}_{ij}^{\Delta\,\prime}(t_n) + \rho_{ij}^{\prime}(t_n)\right] \tag{3-8}$$

where $\bar{\mu}_n$ is the iterative shear modulus and $'$ indicates the deviator component of $\bar{\sigma}_{ij}^{\Delta}$ and ρ_{ij}. In order to calculate the ratcheting limit using LMM, we require the history of residual stress field, $\rho_{ij}(t_n)$.

$$\rho_{ij}(t_n) = \bar{\rho}_{ij} + \sum_{k=1}^{n} \Delta\rho_{ij}{}_M^k \tag{3-9}$$

Step 2 Numerical procedure for ratchet limit

As indicated earlier, ratchet limit analysis within the LMM involves two steps. Step one concludes with the determination of $\rho_{ij}(t_n)$. Once this is done, the ratchet limit is calculated using the existing shakedown methodology where the predefined linear elastic solution is augmented by the varying residual stress field $\rho_{ij}(t_n)$. The upper bound limit is based on Koiter's theorem and is given as:

$$\lambda_{RB} = \frac{\int_V \sum_{n=1}^{N} \sigma_y \bar{\varepsilon}\left(\Delta\varepsilon_{ij}^n\right) dV - \int_V \sum_{n=1}^{N} \left(\hat{\sigma}_{ij}^{\Delta}(t_n) + \rho_{ij}(t_n)\right) \Delta\varepsilon_{ij}^n dV}{\int_V \hat{\sigma}_{ij}^{\bar{F}} \sum_{n=1}^{N} \left(\Delta\varepsilon_{ij}^n\right) dV} \tag{3-10}$$

where

$$\bar{\varepsilon}\left(\Delta\varepsilon_{ij}^n\right) = \sqrt{{}^2/_3 \, \Delta\varepsilon_{ij}^n \Delta\varepsilon_{ij}^n} \tag{3-11}$$

σ_y is the von Mises yield stress, $\rho_{ij}(t_n)$ is the residual stress at the time t_n. $\Delta\varepsilon_{ij}^n$ is the increment of plastic strain that occurs at t_n. λ_{RB} denotes the extra constant load $\hat{\sigma}_{ij}^{\bar{F}}$ the body can endure along with a predefined cyclic load $\hat{\sigma}_{ij}^{\Delta}(t_n)$ before it starts ratcheting. For the fixed displacement field, LMM then produces a sequence of monotonically reducing upper bounds that converges to the least upper bound ratchet limit.

3.4 Extended Direct Steady Cycle Analysis

LMM has been further developed to access more complicated structural responses, which includes a creep dwell. This development is referred to as extended Direct Steady Cycle Analysis (eDSCA). A minimization process $I(\dot{\varepsilon}_{ij}^{c}) = \sum_{l=1}^{L} I^{l}$ was proposed by Chen *et al.* in [7-8] to calculate the steady-state cyclic response of a body subjected to an arbitrary cyclic load history, where L is the total number of loading instances and $\dot{\varepsilon}_{ij}^{c}$ is the kinematic admissible strain rate. For the defined minimization function, an incremental form is proposed:

$$I^{l}(\Delta\varepsilon_{ij}^{l}) = \int_{V} \{\sigma_{ij}^{l}\Delta\varepsilon_{ij}^{l} - [\hat{\sigma}_{ij}^{l}(t_l) + \rho_{ij}^{l}(t_l)]\Delta\varepsilon_{ij}^{l}\} dV \tag{3-12}$$

where $\Delta\varepsilon_{ij}^{l}$ is strain increment and $\rho_{ij}^{l}(t_l)$ is the residual stress, which is the sum of previous changing residual stress field increment $\rho_{ij}^{l}(t_l)$ and constant part of the changing residual stress $\bar{\rho}_{ij}$. In an iterative manner, $\Delta\varepsilon_{ij}^{l}$ is calculated by minimizing the function in Equation. (3-12). Assuming l is the number of load instances considered, and k is the number of sub-cycles required to reach convergence. The residual stress and inelastic strain are calculated based on the elastic stress and the previous accumulated residual stresses at each increment. For the load instance t_l during the loading cycle, $\Delta\varepsilon_{ij,k+1}(t_l)$ is calculated by:

$$\Delta\varepsilon_{ij,k+1}(t_l)' = \frac{1}{2\bar{\mu}(t_l)}\left[\hat{\sigma}_{ij}(t_l) + \rho_{ij,k+1}(t_{l-1}) + \Delta\rho_{ij,k+1}(t_l)\right]' \tag{3-13}$$

where $\bar{\mu}$ is the iterative shear modulus, σ_{ij} is the associated elastic solution, $\rho_{ij,k+1}(t_{l-1})$ is the prior changing residual stress history and $\Delta\rho_{ij,k+1}(t_l)$ is the current changing residual stress associated with that inelastic strain increment. When creep is considered for the load cases, the equivalent creep strain increment is calculated by:

$$\Delta\bar{\varepsilon}^{c} = \frac{B(n-1)\Delta t^{m+1}(\bar{\sigma}_s - \bar{\sigma}_c)}{\left(\frac{1}{\bar{\sigma}_c^{n-1}} - \frac{1}{\bar{\sigma}_s^{n-1}}\right)(m+1)} \tag{3-14}$$

$$\bar{\sigma}_c = \left(\frac{\dot{\bar{\varepsilon}}^F}{B\Delta t^m}\right)^{\frac{1}{n}} \tag{3-15}$$

$$\dot{\bar{\varepsilon}}^F = \frac{\Delta\bar{\varepsilon}^c}{\Delta t}\frac{(m+1)}{(n-1)}\frac{\bar{\sigma}_c^n}{(\bar{\sigma}_s - \bar{\sigma}_c)}\left(\frac{1}{\bar{\sigma}_c^{n-1}} - \frac{1}{\bar{\sigma}_s^{n-1}}\right) \tag{3-16}$$

where *B, m* and *n* are the creep constants of the material, $\bar{\sigma}_c$ represents the creep flow stress, and it is defined as the sum of the start of dwell stress, $\bar{\sigma}_s$ and the residual stress $\Delta\rho_{ij,k+1}(t_l)$ during the dwell period. Equation (3-15) is used to calculate $\bar{\sigma}_c$ and Equation. (3-16) is in-turn used to calculate $\dot{\bar{\varepsilon}}^F$, which is the creep strain rate. The next step involves calculating the residual stress and iterative shear modulus at each increment using the linear solutions previously calculated. The below equation is used for it:

$$\bar{\mu}_{k+1}(x,t_l) = \bar{\mu}_k(x,t_l)\frac{\sigma_y^R(x,t_l)_k}{\bar{\sigma}\left(\hat{\sigma}_{ij}(x,t_l)+\rho_{ij}^r(x,t_l)_k\right)} \tag{3-17}$$

where $\bar{\mu}_{k+1}(x,t_l)$ is the iterative shear modulus at the sub-cycle *k* for l^{th} load instance. $\sigma_y^R(x,t_l)_k$ is either the iterative von-Mises yield stress for the material model considered at load instance t_l or the creep flow stress $\bar{\sigma}_c$. $\rho_{ij}^r(x,t_l)$ is the sum of the constant residual stress field and all previous changing residual stresses at load instance t_l.

3.5 Modification for the inclusion of weldments

Welded structures have regions with different material properties. For better results it is only reasonable to assign different material and creep properties to each of the regions. In order to achieve this, during the model creation stage within Abaqus, each zone is identified and the section names are provided according. The subroutine is enhanced to identify each region and assign the properties as per the region. The material and creep properties are then used within the analysis depending on the region it is called for. The same logic is applied to calculate the fatigue and creep damage at different regions by providing different fatigue and creep damage calculation parameters. It should be noted that this modification is to facilitate the use of temperature dependent parameters, as temperature independent parameters can be directly assigned within Abaqus CAE.

3.6 Chapter summary

The LMM is a numerical methodology that was pioneered by Chen and Ponter in the early 2000s [72], [76]–[78]. Initially, the procedure dealt with limit and shakedown analysis, over the years it has been developed to include ratchet analysis and more recently the eDSCA analysis. The numerical procedures for the shakedown analysis, ratchet analysis and the eDSCA are comprehensively presented in the chapter. The shakedown and ratchet analysis helps in creating the shakedown-ratchet interaction boundary which with inelastic analysis would require innumerable trial and error runs. The eDSCA calculates the steady-state cyclic response considering the full creep-cyclic plasticity.

Compared to traditional inelastic methods, LMM requires very less computational resources. The LMM has the flexibility to be coupled with rule-based codes such as R5, ASME or RCC-MR to assess the creep-fatigue damage and predict the safe life. Further, LMM has the capacity to analyse multi-material structures which makes it an effective tool for MMCs and welded structures. The limit and shakedown analysis of the LMM subroutine has already been consolidated into the R5 research program of EDF Energy to the commercial standard and has acknowledged internally that the start of dwell stress, elastic follow-up factor and strain range values provided by the LMM is potentially more accurate than the ones calculated following the R5 sequence. LMM has progressed much further compared to other direct methods, though it still has areas for improvement such as the implementation of strain hardening law for creep strain analysis.

Chapter 4 Study of ratchet limit and cyclic response of a welded pipe

4.1 Introduction

Ratcheting and low cycle fatigue are failure mechanisms observed in components subjected to cyclic temperature and mechanical loads. Ratcheting is a global failure mechanism which leads to an incremental plastic collapse of the component whereas low cycle fatigue is a localized mechanism which leads to crack initiation which is exacerbated by grooves, notches and changes in the geometry of the component. To estimate the remaining life of the component and predict its failure mechanism, it is important to understand how it responds to various combinations of cyclic loads.

Welded pipes used in many industries are exposed to both cyclic thermal and mechanical loads. It has been of interest to study the variations in the reverse plasticity and ratchet limits of welded pipes. This is because welds are sites of geometric irregularities in the form of joint configurations which leads to local stress concentration that affects the life of the pipe, and because of the different microstructure and material composition within the weldment region that causes a variation in their strength [79]. The presence of temperature difference between the inner and outer surface of the pipe leads to an uneven expansion/contraction within the pipe, this leads to additional stress. If the temperature difference occurs in a short interval of time, this can lead to thermal shock. Structures subjected to repeated thermal shocks may experience incremental crack growth [80]. Thermal shocks are generally a result of some abnormality in the working condition. A typical example of thermal shock is when emergency core cooling water is injected into the reactor coolant system resulting in a sharp change in the temperature across the thickness of the vessel wall [81]. In case of weldments the ductility and brittleness of the HAZ and WM are different compared to the PM, leading to local brittle zones which may lead to crack initiation from these regions.

This chapter includes investigation of the ratchet limit and the plastic strain range, which is associated with the low cycle fatigue, of a circumferential butt-welded pipe by using the ratchet analysis method which includes the DSCA within the LMM. The obtained results are verified by the full incremental cyclic analyses using Abaqus step-by-step method. The pipe is

subjected to a constant internal pressure and a cyclic thermal load. The investigation is carried out by varying 1) material properties of the WM; 2) ratio of inner radius to wall thickness; 3) weld geometry.

The finite element model of the welded pipe, geometry, material properties and applied boundary conditions are presented in Section 4.2. Section 4.3 provides a comprehensive parametric study on the influence of material and geometric properties on the ratchet limit and plastic strain range of the welded pipe. Section 4.4 presents the creation of a limit load envelope that can be used for designing purposes. Section 4.5 is the final section in this chapter where the summary is presented.

4.2 Pipe geometry and material properties

The pipe geometry considered is a circumferentially welded pipe, which includes a single V butt weld with V root. It is subjected to a constant internal pressure and a cyclic thermal load. The weldment comprises of three zones; 1) the PM, 2) the WM and 3) the HAZ. It is assumed that all the three zones exhibit EPP material properties and that they satisfy the von Mises yield condition. An EPP model is opted as they provide conservative results with respect to the ratcheting mechanism with the use of minimal material parameters. The welding induced residual stress in the pipe is considered to be zero due to the post-weld heat treatment (PWHT). Pipe geometry is shown in Figure 4-1 (a) and its dimensions are presented in Table 4-1. The yield stress is considered to be temperature-dependent. Material properties for baseline calculations are indicated in Table 4-2 [80], [82]. The values for thermal conductivity, k, and Poisson's ratio, v, are considered to be the same for all three zones. Due to the limited availability of material properties for HAZ, they are assumed to be the average of PM and WM for this study.

An axisymmetric model is used for the analysis, as shown in Figure 4-1 (b), with the symmetric condition applied in the axial direction. The end of pipe is constrained to remain in-plane thereby simulating expansion of the pipe. An axial tension (Equation)) is applied to simulate the closed-end condition of the pipe.

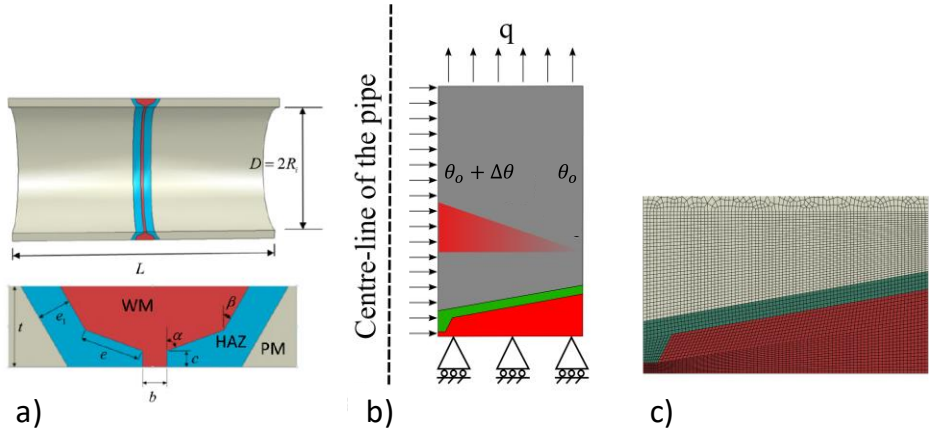

Figure 4-1 a) Butt-welded pipe geometry with principal geometrical parameters. b) Boundary condition and the load applied to the welded pipe; c) Mesh used for FEA.

$$q = \frac{pR_i^2}{2R_i t + t^2} \tag{4-1}$$

It is assumed that the outside temperature of the pipe is θ_0, and the operating temperature of the fluid in the pipe varies between the outer temperature and a higher value, $\theta_0 + \Delta\theta$. The applied cyclic thermal loading can be constructed by three thermal stress extremes: i) a thermal stress field produced by a linear temperature gradient through the wall thickness; ii) a thermal stress field occurring at the highest uniform temperature due to the different coefficient of thermal expansion and Young's modulus between the PM, HAZ and WM; and iii) a zero thermal stress field simulating a uniform ambient temperature. Considering θ_0 equal to zero, the maximum effective elastic thermal stresses for the three extremes can be determined by the maximum temperature difference $\Delta\theta$. This will allow concentration specifically on the effect of the thermal gradient. Hence, the thermal load history can be characterized by $\Delta\theta$. CAX8R 8-node biquadratic axisymmetric quadrilateral elements with reduced integration are used for structural analysis and DCAX8 8-node quadratic axisymmetric heat transfer quadrilateral elements with reduced integration are used for the heat transfer analysis.

Table 4-1 Pipe dimensions for V-butt welded pipe.

$L\ (mm)$	$R_i\ (mm)$	$t\ (mm)$	$e_1\ (mm)$	$e\ (mm)$	$b\ (mm)$	$c\ (mm)$	$\alpha\ (°)$	$\beta\ (°)$
1000	300	40	2.5	4.5	3	2	63	10

Table 4-2 Temperature independent material parameters for V-butt welded pipe.

$E_y^{PM}(GPa)$	$E_y^{HAZ}(GPa)$	$E_y^{WM}(GPa)$	$k(Wm^{-1}{}^{\circ}C^{-1})$
200	220	240	15
$\alpha^{PM}(\times 10^{-5}{}^{\circ}C^{-1})$	$\alpha^{HAZ}(\times 10^{-5}{}^{\circ}C^{-1})$	$\alpha^{WM}(\times 10^{-5}{}^{\circ}C^{-1})$	v
3.8	3.7	3.6	0.3

Table 4-3 Temperature-dependent yield stress for V-butt welded pipe.

	≤ 20 ℃	200 ℃	400 ℃	600 ℃
$\sigma_y^{PM}(MPa)$	230	184	132	105
$\sigma_y^{HAZ}(MPa)$	345	275.5	198	157
$\sigma_y^{WM}(MPa)$	460	367	264	209

4.3 Parametric study

The parametric study is conducted to investigate the effects of 1) material properties such as the coefficient of thermal expansion of WM (α^{WM}), Young's modulus of WM (E^{WM}), the yield stress of WM $\left(\sigma_y^{WM}\right)$; 2) weld geometry, and 3) ratio of inner radius to wall thickness (R_i/t) on the ratchet limit and the plastic strain range. It is generally convenient to work with plots that have a dimensionless set of ordinate and abscissa. The plots used for the ratchet limit discussions have a normalized internal pressure, p/p_0 and a normalized temperature range, $\Delta\theta/\Delta\theta_0$ as their ordinate and abscissa. p_0 = 23 MPa and $\Delta\theta_0$ = 50 ℃ are the reference internal pressure and cyclic temperature range respectively.

Figure 4-2 shows the shakedown and ratchet limit interaction curve for the baseline model considered in this study. S stands for the shakedown region, P indicates reverse plasticity region and R is the ratcheting region. The shakedown and ratchet limit curves are generated using the LMM procedures introduced in Section 3.2 and Section 3.3. The first step for both the process is to generate the elastic stress solutions for all the load extremes, in this case due to the thermal gradient and the mechanical load, and the temperature field. The next step is to define the loading history. Once this is done, the shakedown limit and ratchet limit multipliers may be produced using the LMM subroutine by running a series of analysis for various combinations of the loads. It should be noted that each of the above calculation will produce

a point on the shakedown or ratchet limit curve and hence a series of analysis is required to construct the complete shakedown-ratchet interaction curves. The thermal field applied is used to modify the temperature dependent properties such as the yield stress and Young's modulus.

Plastic strain range investigation using DSCA is done for two pressure references, p/p_0= 0 (only cyclic temperature load) and p/p_0= 0.25. This is selected as for most cases analysed, they are well within the P region, and provide grounds for better comparison. The load points for plastic strain range analysis are indicated in Figure 4-2.

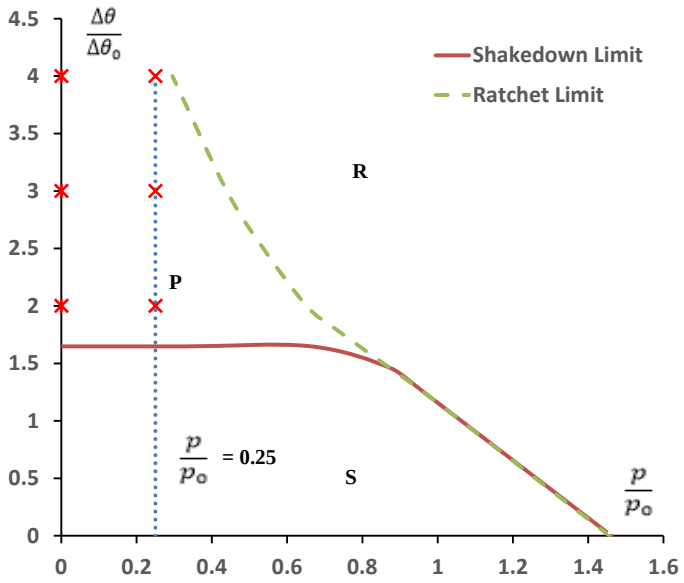

Figure 4-2 Shakedown - ratchet limit interaction curve and load points adopted for plastic strain analysis.

4.3.1 Influence of material properties of the weldment

4.3.1.1 Effect of coefficient of thermal expansion of WM, α^{WM}

In increments of 0.2 x 10^{-5}, α^{WM} is increased from 3.2 x 10^{-5} to 4.6 x 10^{-5}. Figure 4-3 shows the ratchet limit curve of the welded pipe for varying values of α^{WM}, it can be seen that they exhibit a typical Bree-like diagram. As ratcheting is a global mechanism, the coefficient of thermal expansion, which only has a localized effect, does not affect the ratchet limit.

Figure 4-4 indicates the variation of plastic strain range with increasing α^{WM}. It can be observed that the presence of an additional mechanical load has only a minimal effect on the plastic strain range of the pipe. At lower cyclic temperature load, the presence of mechanical load does not affect the plastic strain range values, whereas at higher cyclic temperature loads a slight increase in the plastic strain range is observed. The plastic strain range decreases to a minimum value as α^{WM} is increased after which it remains constant with and without the presence of an additional mechanical load. In all cases analysed the plastic strain range values were maximum at the PM-HAZ interface towards the inner side of the pipe. Also, it should be noted that for the same miss-match factor the plastic strain range is greater at higher temperatures.

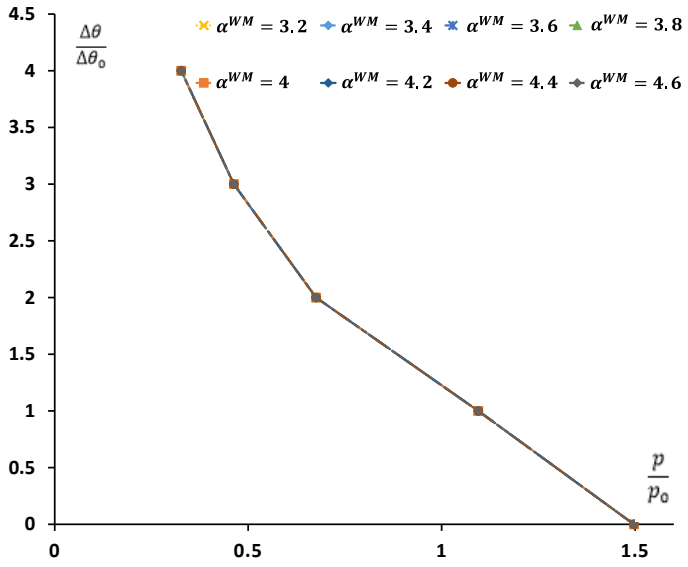

Figure 4-3 Ratcheting curves of the welded pipe for varying α^{WM}.

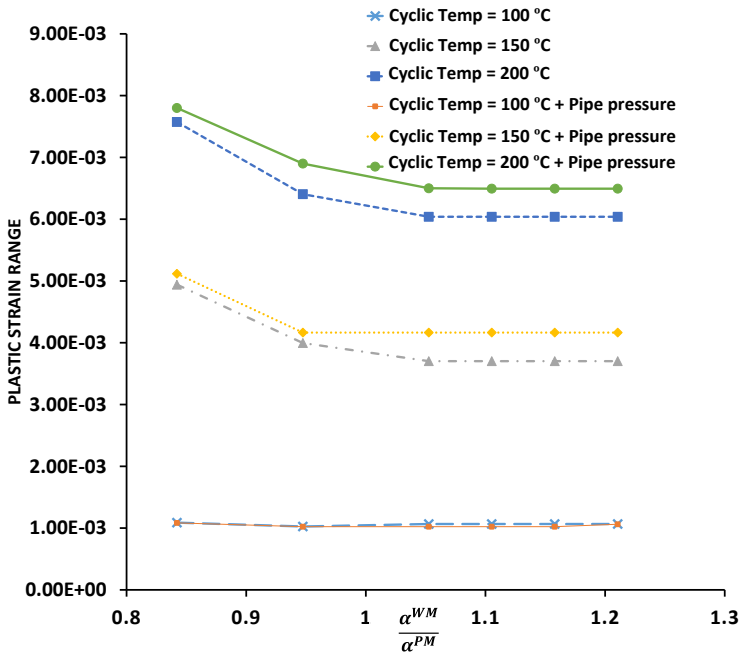

Figure 4-4 Comparison of plastic strain range for α^{WM}, with and without mechanical load.

4.3.1.2 Effect of Young's modulus of WM, E^{WM}

Young's modulus of the WM, E^{WM} is varied from 80 GPa to 560 GPa, in increments of 80 GPa. Figure 4-5 shows the ratchet limit curves obtained, they are congruent and exhibit Bree-like diagram. As reflected in Figure 4-5, the Young's modulus of the WM does not influence the ratcheting curve or the limit load. This is because, as mentioned in the previous subsection, ratcheting is a global mechanism and the Young's modulus has a localized effect only. Furthermore, the yield stress of the WM is twice that of the PM due to which ratcheting occurs in the PM region within the ranges adopted for this study.

Variation of the plastic strain range with increasing E^{WM} is presented in Figure 4-6. The plastic strain accumulation is concentrated at the HAZ-PM interface in all the cases. For $E^{WM}/E^{PM} > 0.8$ yielding is observed within the WM also which reduces the constraint it imposes at the HAZ-PM interface leading to a nearly constant plastic strain range. The converse is observed for $E^{WM}/E^{PM} < 0.8$, with the WM experiencing stress well within its yield stress and enhances the constraint it imposes at the HAZ-PM, resulting in a much larger plastic strain range. It is particularly interesting to note that the plastic strain range with and without mechanical load is almost the same for a particular cyclic thermal load. Figure 4-7

presents the stress contours of the elastic analysis done on the welded pipe, with E^{WM}= 560 GPa, for only pressure load, only temperature load $\Delta\theta/\Delta\theta_0$=2 (100 ℃) and $\Delta\theta/\Delta\theta_0$=4 (200 ℃) and combination of both mechanical and temperature load. It is evident from them that the stress due to pressure alone re-distributes in the presence of the thermal stress causing the resultant stress to be similar to that of thermal stress alone. Thereby resulting in similar maximum plastic strain range values. Similar results were observed for all other values of E^{WM} undertaken in this study. Ideally, the Young's modulus of the PM and WM must be similar or have their ratio close to one. This reduces the stress concentration at the weldment region due to the material mismatch.

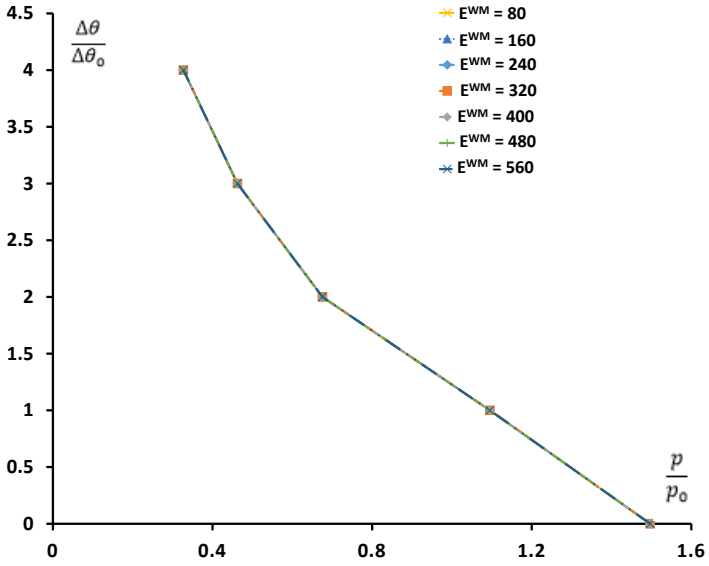

Figure 4-5 Ratcheting curves of the welded pipe for varying E^{WM}.

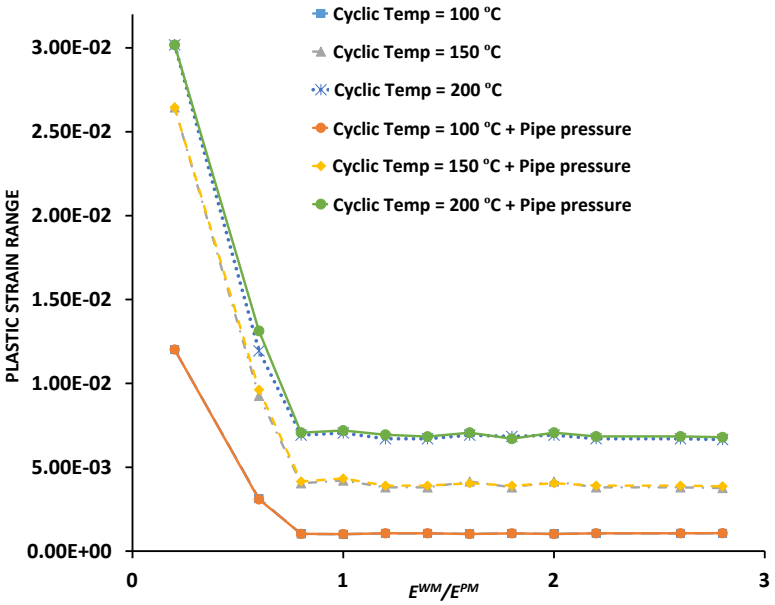

Figure 4-6 Comparison of plastic strain range for varying E^{WM}, with and without mechanical load.

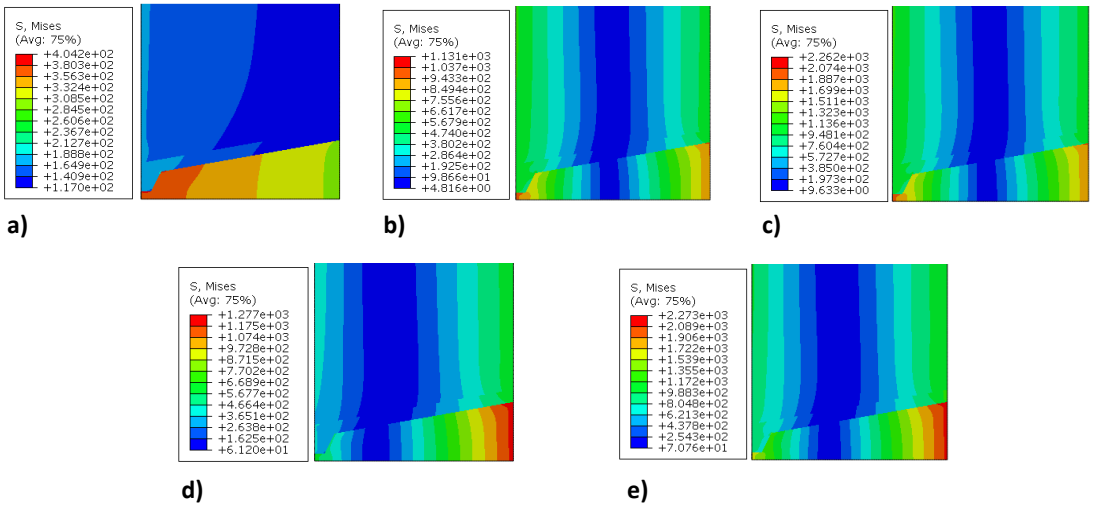

Figure 4-7 Stress contours for elastic analysis; a) Due to internal pipe pressure; b) Due to cyclic temperature load, 100 °C c) Due to cyclic temperature load, 200 °C; d) Due to combined load of internal pipe pressure and cyclic temperature load of 100 °C; e) Due to a combined load of internal pipe pressure and cyclic temperature load of 200 °C.

4.3.1.3 Effect of yield stress of WM, σ_y^{WM}

The yield stress of WM, σ_y^{WM}, was varied from 115 to 460 MPa. Figure 4-8 shows the ratchet limit interaction curves obtained. When $\sigma_y^{WM}/\sigma_y^{PM} \geq 1$, ratchet limit curves obtained are similar to Bree's like diagram and they superimpose each other. Ratcheting in these cases occurs in the PM. Analysis of limit load and ratchet limit curves at lower σ_y^{WM} values of 23 MPa, 46 MPa, and 69 MPa are done as special cases, represented in Figure 4-8.

When $\sigma_y^{WM}/\sigma_y^{PM} \leq 1$, the ratchet limit curve intersects the y-axis as the temperature is increased with ratcheting occurring in the WM region. The intersection of the ratchet curve on the y-axis indicates that the pipe experiences thermal ratcheting. At such low yield stress of the WM, the stress due to the thermal load, which is enhanced by the difference in the coefficient of thermal expansion of WM and HAZ and the stress due to the weld geometry is very high, and this may lead to ratcheting within the WM. To deeply understand the mechanism and validate the ratchet limit curves obtained from LMM, cyclic load conditions as indicated by the points A1, A2, A3, and A4 in Figure 4-8 and described in Table 4-4 are analysed by Abaqus step-by-step analysis. They are cyclic load points chosen with respect to σ_y^{WM}= 142 MPa. The results obtained are in agreement with the result from LMM analysis. The obtained histories of plastic strain magnitude, PEMAG, are given in Figure 4-9. Cyclic load points, A1 and A2 which are above the ratchet limit curve predicted by LMM exhibit ratcheting behaviour while cyclic load points, A3 and A4 which are below the ratchet limit curve exhibit global shakedown behaviour. For load points A1 and A2, the strain increment is around 25-30% in 20 cycles (40 steps). While for A3 and A4 the strain rates stabilise indicating that they are under global shakedown. Thus, we can confirm the ratcheting limit curves obtained by LMM.

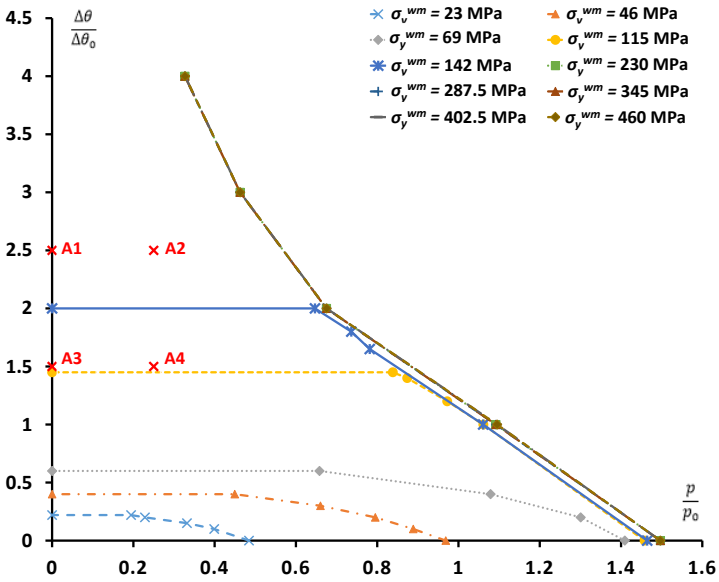

Figure 4-8 Ratcheting curves of the welded pipe for varying σ_y^{WM}.

Table 4-4 Cyclic load points analysed using step by step analysis.

Load Case	σ_y^{WM} (MPa)	p/p_0	$\Delta\theta/\Delta\theta_0$
A1	142	0	2.5
A2	142	0.2	2.5
A3	142	0	1.5
A4	142	0.2	1.5

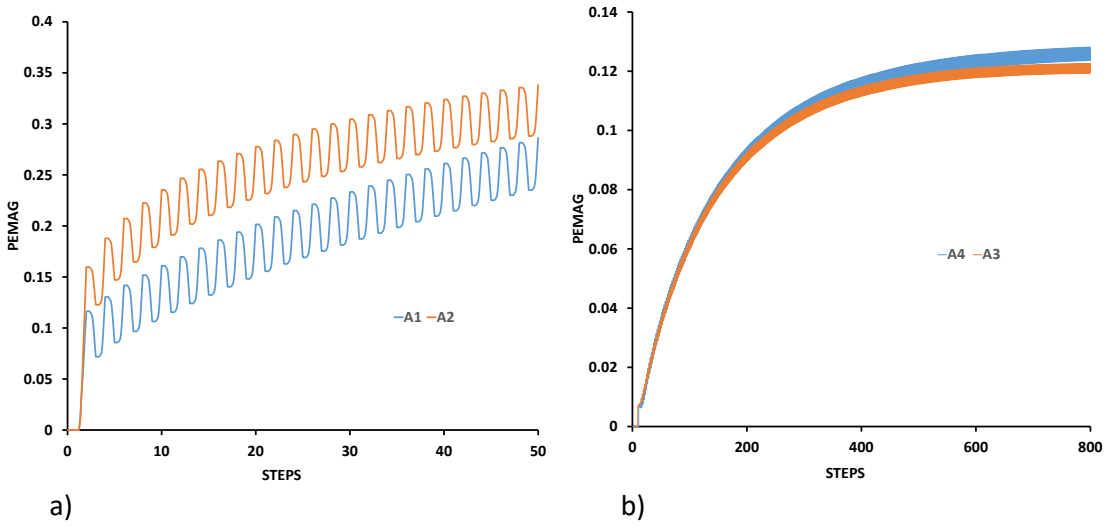

Figure 4-9 History of plastic strain for the cyclic load point evaluated by step-by-step analysis a) for A1 and A2; b) A3 and A4.

The limit load for $\sigma_y^{WM}/\sigma_y^{PM} \geq 1$ is constant. For σ_y^{WM}= 115MPa, only a slight reduction is observed in the limit load. This is because, at limit load, all the different material zones reach their respective yield stress (Figure 4-10 (a)), which results in only a slight reduction of limit load. Whereas for lower σ_y^{WM} values of 23, 46, and 69 MPa, the limit load significantly reduces with stress concentration in the WM region and the maximum strain region occurring at the HAZ-WM metal interface, Figure 4-10 (b).

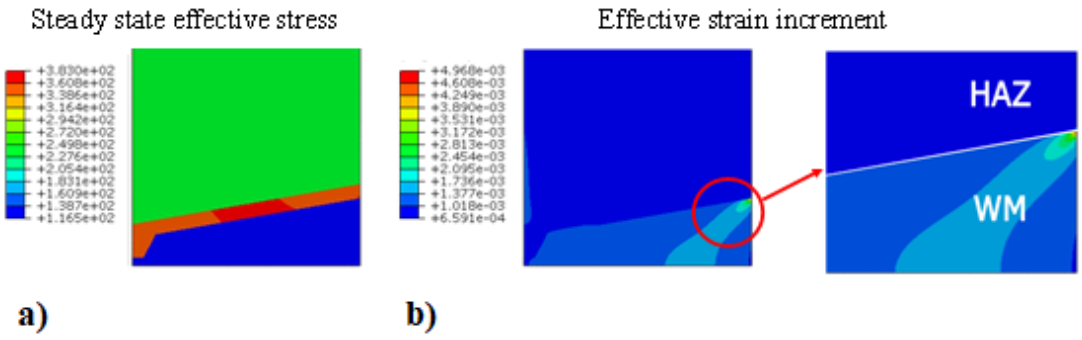

Figure 4-10 a) At limit load, both the PM and WM have attained their respective yield stress for σ_y^{WM} =115 MPa; b) The maximum strain region at limit load for σ_y^{WM}=115 MPa.

For $\sigma_y^{WM}/\sigma_y^{PM} \leq 1$, a strict Bree like diagram is not obtained and so the load points chosen for the plastic strain range analysis differ from the ones mentioned in Section 4.3. Figure 4-11 indicates the shakedown and ratchet limit curve for σ_y^{WM}= 115 MPa and σ_y^{WM}= 142 MPa along with the load points analysed for the the plastic strain range study. Figure 4-12 shows the variation of plastic strain range for $\sigma_y^{WM}/\sigma_y^{PM} \leq 1$, it is plotted with plastic strain range as the ordinate and $\Delta\theta/\Delta\theta_0$ as the abscissa. It is observed that for the particular cyclic load case analysed, the thermal load always dominates the internal pressure load and the plastic strain range remains the same with or without the mechanical load. Also, the plastic strain range increases with an increase in temperature.

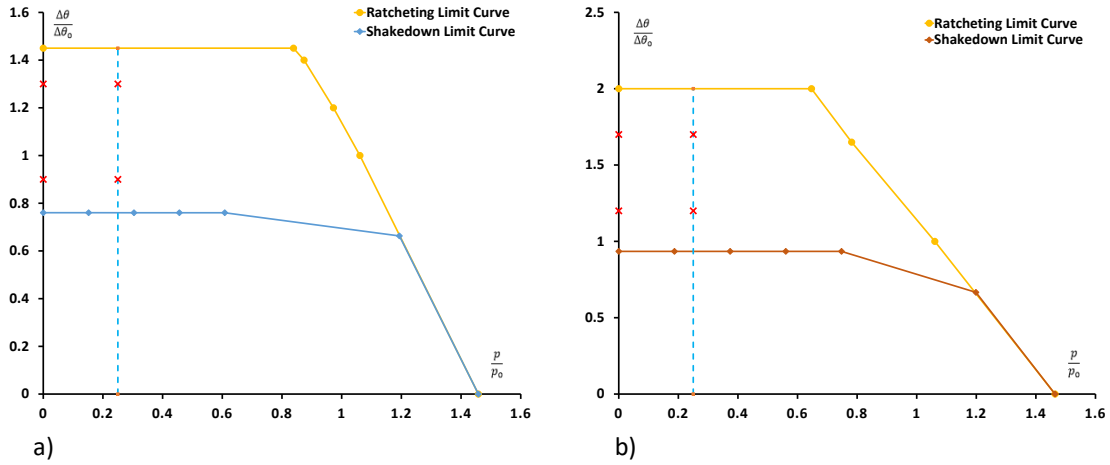

Figure 4-11 Shakedown limit curve, ratchet limit curve and load points analysed for fatigue study; a) For σ_y^{WM}= 115 MPa; b) For σ_y^{WM}= 142 MPa.

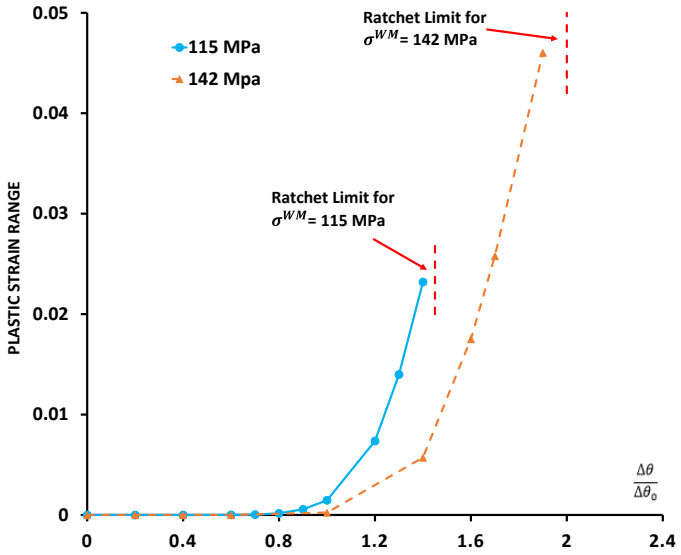

Figure 4-12 Variation of plastic strain range for $\sigma_y^{WM}/\sigma_y^{PM} \leq 1$.

Figure 4-13 gives the variation of plastic strain range with increasing σ_y^{WM} for $\sigma_y^{WM}/\sigma_y^{PM} \geq 1$. It is interesting to note that for a defined cyclic temperature load the plastic strain range decreases to reach a minimum, after which it attains a constant value.

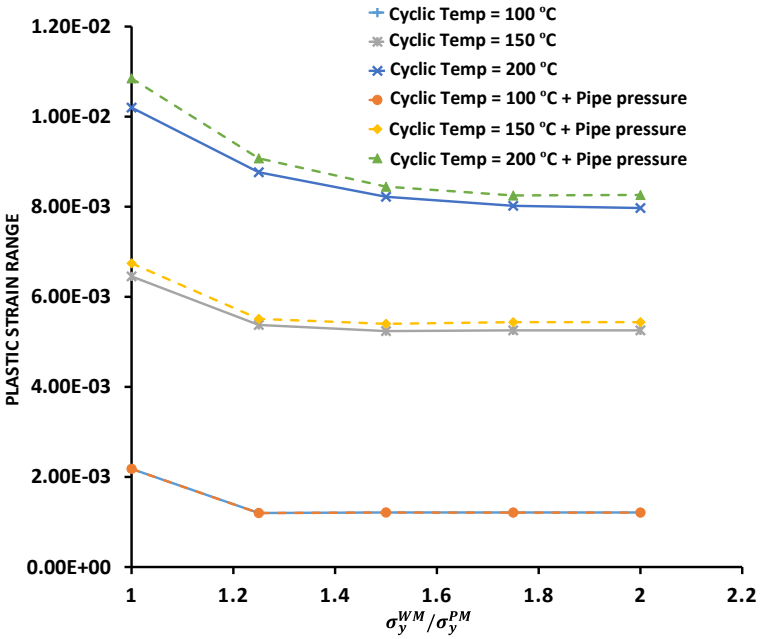

Figure 4-13 Variation of plastic strain range for $\sigma_y^{WM}/\sigma_y^{PM} \geq 1$, with and without mechanical load.

4.3.2 Influence of weld geometry

Five weld parameters *b, c, e, α* and *β* are individually varied to investigate the influence of weld geometry on ratcheting curve. They are varied as; *b* = 2, 3, 5 (mm); *c* = 2, 3, 4 (mm); *e* = 4.5, 6.5, 8.5 (mm), *α* = 43, 53, 63 (°) and *β* = 8, 10, 16 (°). Figure 4-14 shows the effect of the above parameters on the ratchet limit, they do not influence the ratchet limit curve. Hence, it can be concluded that for the range considered in this study, the weld geometry does not affect the ratchet curve.

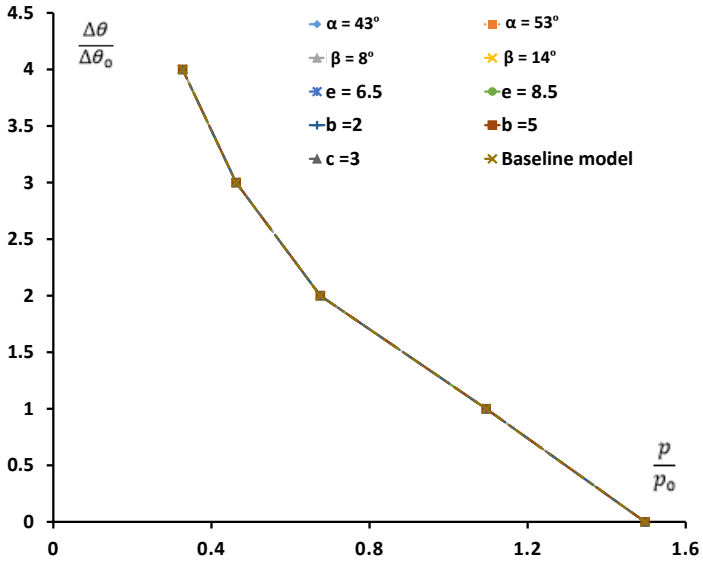

Figure 4-14 Ratcheting curves of the welded pipe for varying geometric parameters.

Figure 4-15 shows the variation of plastic strain range for different geometric parameters considered in this study. It can be seen that at lower temperatures the plastic strain range for all the parameters is similar, but as the temperature increases, there is an increase in the plastic strain range. The parameter β causes the maximum variation in plastic strain range with an increase in temperature.

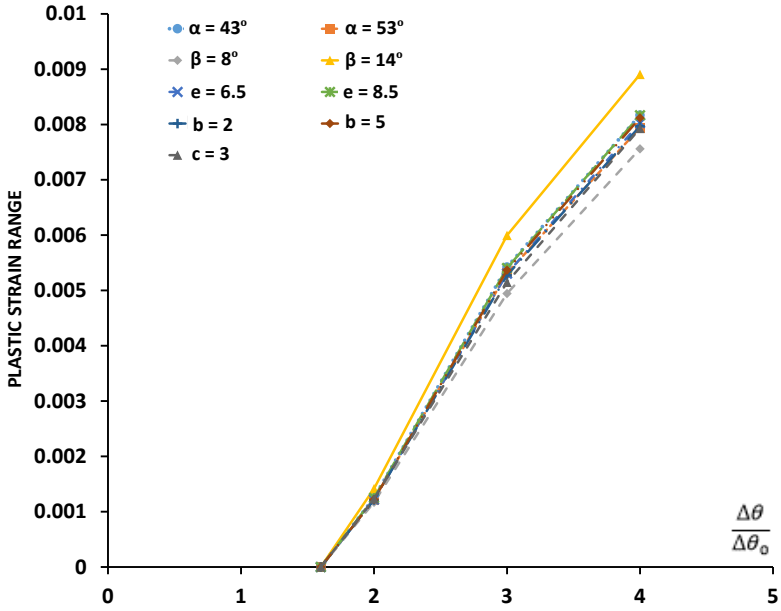

Figure 4-15 Variation of plastic strain range for varying geometric parameters.

4.3.3 Influence of ratio of inner radius to wall thickness, R_i/t

The effect of inner radius, R_i, to wall thickness, t, ratio (R_i/t) on the ratchet limit is investigated in this sub-section. The inner radius is varied from 40 mm to 600 mm and the thickness of the pipe is maintained at a constant value of 40 mm. The ratchet limit curves obtained are presented in Figure 4-16. For all R_i/t ratios, a typical Bree-like diagram is obtained. Increase in the R_i/t ratio decreases the limit load. This is because the increase in radii results in a larger area for pressure loading. The resultant high hoop and axial stresses lead to a reduced limit load and an overall movement of the ratchet limit curve towards the y-axis. It is also observed that the slope of the ratchet curve increases with an increase in the ratio of inner radius to wall thickness.

Figure 4-17, shows the effect of varying R_i/t on the plastic strain range for different cyclic temperature loads, with and without mechanical load. Compared to previous sections, the plastic strain range analysis with mechanical load is done for $p/p_0 = 0.1$. This is because $p/p_0 = 0.25$ would limit the comparison studies as for $R_i/t \geq 10$, the body would exhibit ratcheting behaviour at higher temperatures as evident from Figure 4-16. The variation of plastic strain range with and without mechanical load is minimal for a particular cyclic thermal load. This can be explained by the really high stress that is produced by the thermal shock occurring between the internal and external faces of the pipe. It can also be seen from Figure 4-17 that for a given cyclic thermal load, plastic strain range decrease as we go from a thick pipe to a thin pipe configuration. This is because the thick pipe which has a smaller surface area experiences higher stress due to the cyclic temperature load compared to the thin pipes which result in lower plastic strain range.

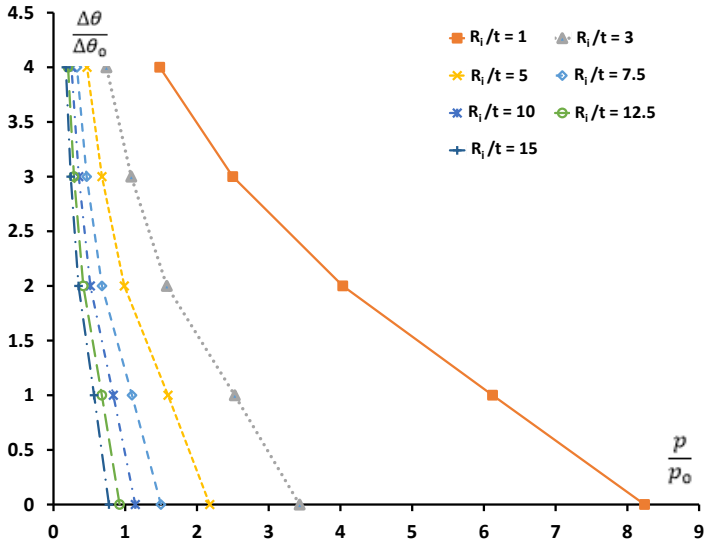

Figure 4-16 Ratcheting curves of the welded pipe for varying R_i/t ratio, at constant t = 40 mm.

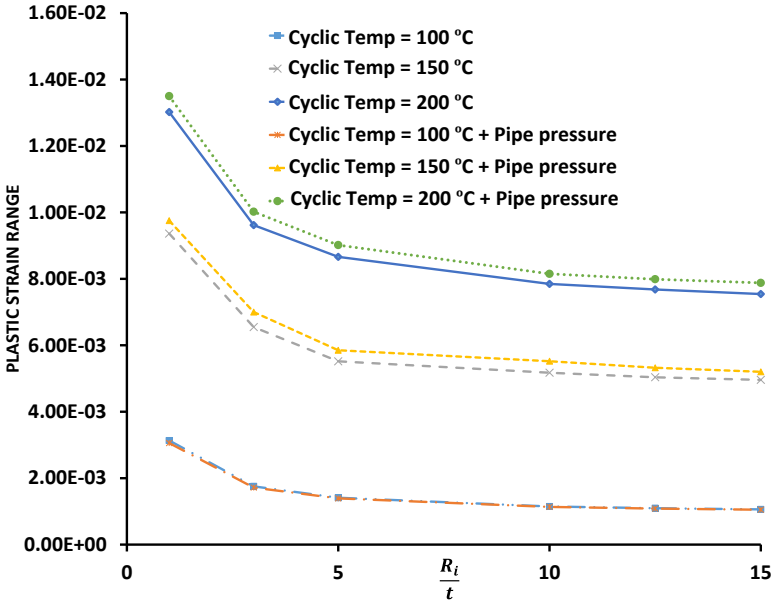

Figure 4-17 Plastic strain range for varying R_i/t, with and without mechanical load.

4.4 Creation of limit load envelope and further discussions

In the previous subsection, the results show how various material properties, weld geometry, and the ratio of inner radius to wall thickness affect the ratchet limit and the plastic strain range of the pipe. Of which, R_i/t and σ_y^{WM} are parameters that influence the ratchet limit curve and limit load the most. Whereas the coefficient of thermal expansion, Young's modulus and weld

geometry have minimal or no effect on the ratcheting limit curves for the range considered in the study. The limit loads obtained in Section 4.3.1.3 and Section 4.3.3 are normalized to the limit load of a pure PM pipe and replotted in Figure 4-18. The trend line fitted to the data gives the functions in Equations (4-2) and (4-3).

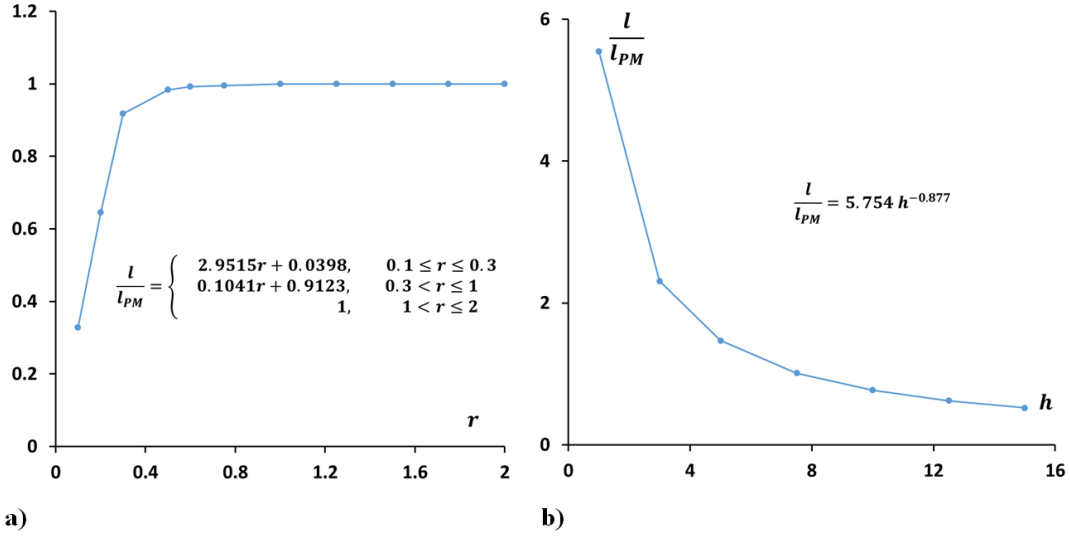

Figure 4-18 a) The effect of σ_y^{WM} on the limit loads b) The effect of R_i/t on the limit loads.

$$\frac{l}{l_{PM}} = \begin{cases} 2.9515r + 0.0398, & 0.1 \le r \le 0.3 \\ 0.1041r + 0.9123, & 0.3 < r \le 1 \\ 1, & 1 < r \le 2 \end{cases} \quad (4\text{-}2)$$

$$\frac{l}{l_{PM}} = 5.754h^{-0.877} \quad (4\text{-}3)$$

where l_{PM} is the limit load of a pure PM pipe, $r = \sigma_y^{WM}/\sigma_y^{PM}$ and $h = R_i/t$. Equation (4-3) is similar to the function obtained by Li *et al.* in [83] for a similar welded pipe.

For all the parametric study undertaken, the plastic strain range increases with an increase in the cyclic temperature load signifying a decrease in the LCF life of the pipe. The most prominent area for LCF failure is the PM-HAZ interface for the base model in this case study. The critical locations are indicated in Figure 4-19 (a) (highlighted by red circles and ordered for decreasing severity). Figure 4-19 (b) represents the hysteresis loop with increasing cyclic thermal load for location 1. Figure 4-19 (c) represents the hysteresis loop, with and without mechanical load for a cyclic thermal load of 150 ℃. The mechanical load has minimal

influence on the plastic strain range. This is because the stress produced by the thermal gradient due to the thermal shock is really high. By analyzing the shape and magnitude of the total strain range in location 1, a circumferential crack can be expected to start.

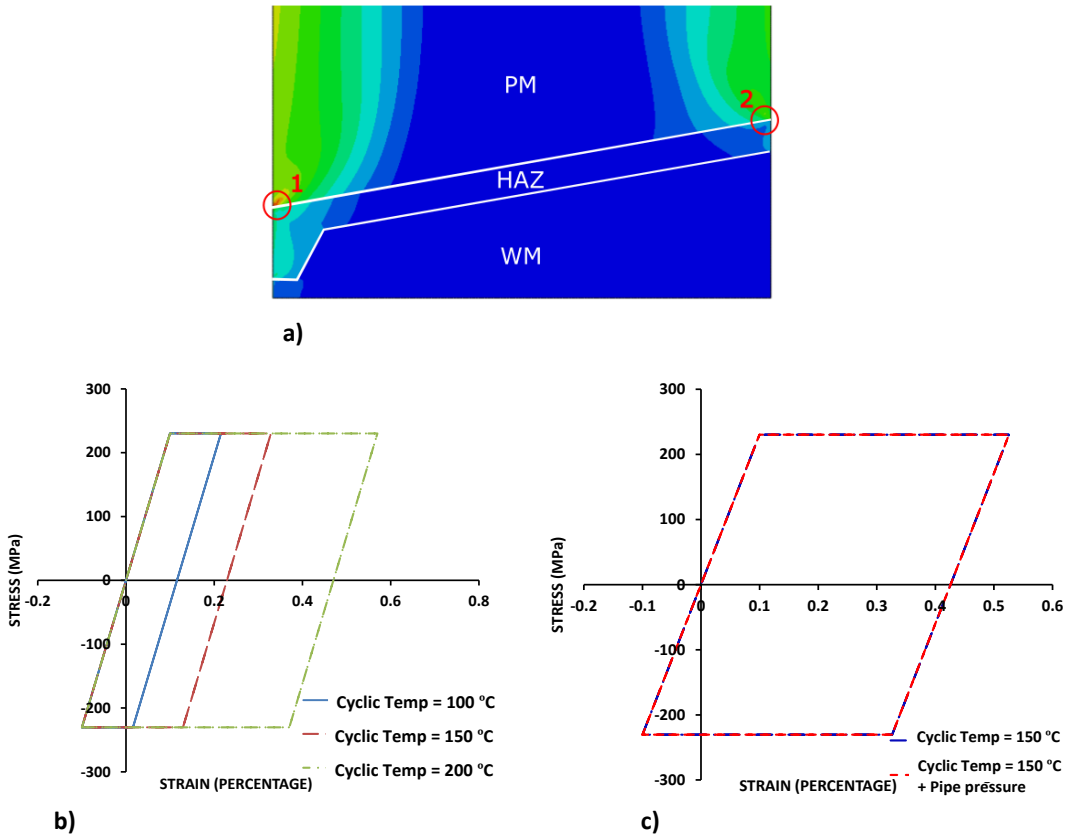

Figure 4-19 (a) Critical location for LCF failure; (b) Hysteresis loop with increasing cyclic temperature load for location 1; (c) Hysteresis loop with and without mechanical load for a cyclic thermal load of 150 °C.

4.5 Chapter summary

The ratchet limit analysis and cyclic response assessment of a welded pipe subjected to a constant pressure and a cyclic temperature load under various conditions are studied using the LMM and the main observation made are:

1. The coefficient of thermal expansion of the WM, Young's modulus of the WM and weld geometry have a localised effect only hence they do not affect the ratchet limit curves for the material properties and range considered in the study.

2. For lower σ_y^{WM} pipe experiences thermal ratcheting and in these cases the secondary load is more prominent. The ratcheting curve sharply intersects the y-axis with an increase in temperature.

3. The increase in the ratio of inner radius to pipe thickness leads to larger hoop and axial stress, and result in a decrease in the limit load. Further they shift the ratchet limit curve such that is reduces the reverse plasticity region.

4. Though many factors such as ductility etc, influence the failure region, based on the deformation analysis alone done it is expected that the failure occurs either in the WM region, for lower σ_y^{WM}, or at the WM-HAZ interface.

5. A safety limit envelope is created and empirical formulas are derived for designing any welded pipe within the considered range.

The study demonstrates that cyclic thermal load due to the thermal gradient plays a crucial role compared to the internal pressure in determining the LCF life of the pipe and may lead to thermal ratcheting in extreme cases. For nuclear power plants where the temperature build-up is in a controlled manner a thermal shock is not expected unless in the event of a malfunction or accident. Nevertheless, in case the piping system is exposed to a large thermal gradient due to an abnormal function, it will also affect the creep damage mechanism during any subsequent dwell. This is explored in the case study presented in the subsequent chapter. Moreover, with the rise of hybrid power plants which uses more than one type of energy source, frequent start-ups and shut-downs are expected with the piping system exposed to frequent thermal gradients and such damage mechanisms becoming more prominent.

Chapter 5 Fatigue and creep damage of welded connectors and joints

5.1 Introduction

Connectors such as elbows and flanges are an integral part of piping systems and welding is the only practical joining process to place them within the piping system. Their performance in terms of structural integrity is very important [84][85]. The previous generation of power plants used a single source of energy and operated for longer duration at sustained loads. With the development in the field of renewable energy, power plants are expected to accommodate flexible modes of operation which will have frequent start-ups and shut-downs, thereby subjecting the piping system to severe loading conditions.

Both the fatigue and creep resistance of a structure is influenced by a weldment. The extent to which they are altered depends on the geometry and loading condition [86]. Three numerical cases studies are presented in this chapter with each case study dealing with different facets of the fatigue and creep damage in welded structures. The difference in the material characteristics within the weldment region causes a stress raiser on the application of any load. This is even more profound during the application of a thermal load if there is a difference in the coefficient of thermal expansion. When subjected to cyclic thermal loads the structure often experiences reverse plasticity [87]. In such cases the presence of a weld will largely impact its fatigue tolerance. Hence the first case study presented is of a welded elbow which investigates the effect of various complex loading combinations of internal pressure, bending moment (BM) and thermal load on its fatigue life and compares it to that of a single material elbow. Compared to homogenous temperature build up, the presence of a large thermal gradient during loading will induce considerable stress. In addition to the effect on fatigue damage, such loading instances will have a detrimental effect on the creep damage too [80]. The presence of welds only enhances the severity. Hence, the second case study deals with the effect of initial thermal loading on the creep damage of a dissimilar welded flange (DWF) and provides a comparison between the DE and TF approaches. Welds also induce multi-axial stress within the component which significantly alters the damage evolution compared to uniaxial stress, and leads to different regions experiencing predominantly tensile or

compressive stress. It is critical to identify them especially during a creep dwell as the damage mechanism at compressive and tensile dominant regions are different. The third case study deals with the effect of multiaxial and compressive stress on the creep damage of a welded pipe. The creep damage calculation as recommended by both the RCC-MR and ASME are also presented.

.

Based on the case studies, the chapter is broadly divided into three sections. Each of them includes a brief introduction followed by details of the geometry, boundary conditions and material properties. For the case studies dealing with creep, further discussions on the creep damage model considered are also presented. Finally, Section 5.5 provides a summary of the chapter.

5.2 Case study 1: Low cycle fatigue of welded elbows under cyclic loading

To satisfy the load demands and maximise profits at the same time within the power industry, the power plants are cycled on an everyday basis [88]. This leads to significant fatigue damage. A typical elbow is subjected to pipe pressure, BM, thermal load or a combination of them. Considerable literature focused on the response of elbows under monotonic and cyclic loading conditions are available. However they do not consider the effect of the weldment on the LCF life of elbows under a complex combination of cyclic loads or are usually limited to room temperature studies.

Due to the excellent material properties such as a low coefficient of thermal expansion and higher weldability, P91 is among the preferred materials within power plants for the piping system. Nevertheless, failures are generally in the weldment region [89]. Studies within this section aim at investigating the LCF life and damage of a P91 welded elbow subjected to various cyclic load combinations.

5.2.1 Pipe geometry and material properties

The geometry of the welded elbow with two straight pipes is shown in Figure 5-1. The pipe dimensions correspond to a standard pipe size of 10 inches and schedule 80. The key dimensional parameters are presented in Table 5-1. C3D20R quadratic hexahedral elements are used for the structure analysis and DC3D20 quadratic hexahedral elements are used for the

heat transfer analysis. Following a mesh refinement study, the configuration of the welded elbow was meshed with 7, 425 elements.

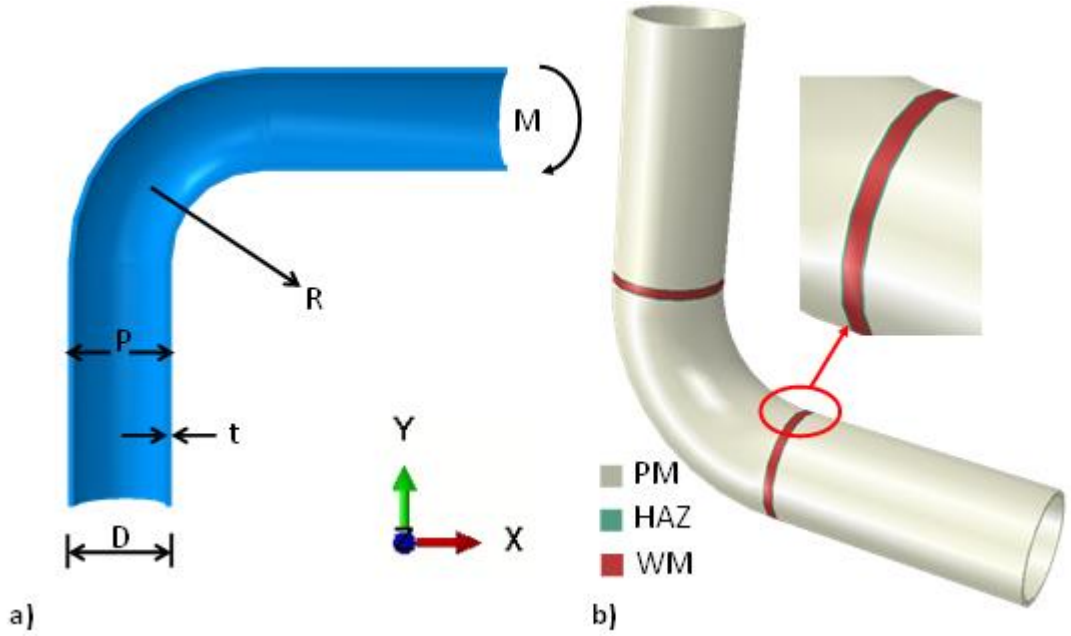

Figure 5-1 a) Geometry of the elbow with key parameters; b) Representation of the different zones.

Table 5-1 Key dimensions of the welded elbow.

$D\ (mm)$	$R\ (mm)$	$t\ (mm)$
263	381	40

The weldment comprises of three zones; 1) the PM, 2) the WM and 3) the HAZ. The cyclic stress-strain behaviour of the zones is modelled using the RO relationship defined as:

$$\frac{\Delta\varepsilon}{2} = \frac{\Delta\sigma}{2E} + \left(\frac{\Delta\sigma}{B_{RO}}\right)^{\frac{1}{\beta_{RO}}} \tag{5-1}$$

where $\Delta\varepsilon/2$ is the total strain amplitude, $\Delta\sigma$ is the total stress range, B_{RO} and β_{RO} are material parameters. The material properties of the weldment are largely obtained from the work presented by Farragher T.P *et al.* in [89] with reasonable interpolation for temperature

dependence. The key material properties are listed in Table 5-2. Considering the symmetry of the geometry, a 3-D half geometry model is used for the analysis within Abaqus. A symmetric boundary condition is applied on the x-y plane of the elbow. The bottom face is constrained using kinematic coupling allowing all motions of the nodes except the expansion/contraction in the axial direction. Plane end condition is applied on the free end of the pipe allowing it to expand in-plane along the length simulating thermal expansion of the structure.

The cyclic loads considered include an internal pressure, BM and thermal load. The pressure is applied to the inner surface of the connection. As a closed-end condition is considered, an equivalent axial tension is applied on the free end of the straight pipe section to replicate the axial stress. The pressure applied is normalised and restricted to 0.8 times the limit pressure (calculated as Equation (5-2)). The cyclic in-plane opening BM is obtained by imposing a clockwise moment about the z-axis. As a half model is used for the analysis, half moment for the entire structure is taken. The BM applied is normalised and restricted to 0.8 times the limit BM (calculated as Equation (5-3)). The pressure and BM are limited as such to provide the basis for reasonable discussions on various damage mechanisms else, the mechanism restricts to ratcheting alone.

$$P_L = \frac{2}{\sqrt{3}}\left(2\sigma_y t/D\right) \tag{5-2}$$

$$M_L = \sigma_y D^2 t \tag{5-3}$$

Table 5-2 Key material properties of the welded elbow.

	PM		HAZ		WM	
Temp (°C)	0	500	0	500	0	500
$\sigma_y(MPa)$	245	175	263	169	259	185
R.O. Constant-B_{RO}	934	467	910	455	1178	589
R.O. Constant-β_{RO}	0.068		0.049		0.066	
$E(GPa)$	175		161		195	

The Manson-Coffin-Basquin equation is used for the construction of the fatigue curve and the subsequent damage calculations.

$$\frac{\Delta\varepsilon}{2} = \frac{\Delta\varepsilon_e}{2} + \frac{\Delta\varepsilon_p}{2} = \frac{\acute{\sigma_f}}{E}\left(2N_f\right)^b + \acute{\varepsilon_f}\left(2N_f\right)^c \quad (5\text{-}4)$$

where σ_f' is the fatigue strength coefficient, *b* is the fatigue strength exponent, ε_f' is the fatigue ductility coefficient and *c* is the fatigue ductility exponent. The same EN curve is used for all the three zones due to limited data available for the HAZ and WM zones. To account for any uncertainty, the fatigue curve for a temperature higher (550 °C) than the maximum considered temperature is used. The values for the PM material are obtained from [90] as σ_f' = 454.61 MPa; $b = -0.05036$; $c = -0.48108$; and ε_f' = 0.12091.

5.2.2 Results for high-temperature fatigue – isothermal and non-isothermal loading

Before imposing complex loading conditions, the effect of isothermal and non-isothermal thermal loading is investigated. A cyclic isothermal temperature of 500 °C is applied throughout the cross-section of the connection. The loading cycle is presented in Figure 5-2 (a). The von Mises stress during loading and unloading is shown in Figure 5-2 (b). It can be observed that due to the difference in the coefficient of thermal expansion of the three zones, stress is concentrated within the weldment region during both the loading and unloading instances. Maximum stress accumulation is observed within the HAZ and the most critical location is at the interface between the HAZ and PM. For a single material elbow only a nominal stress accumulation will be observed within the elbow due to the isothermal loading. In traditional power plants, this loading condition is considered as the normal operating condition wherein no thermal gradient is observed. Maintaining this loading condition for a substantial amount of time will lead to the introduction of creep damage, which is discussed in the subsequent sections.

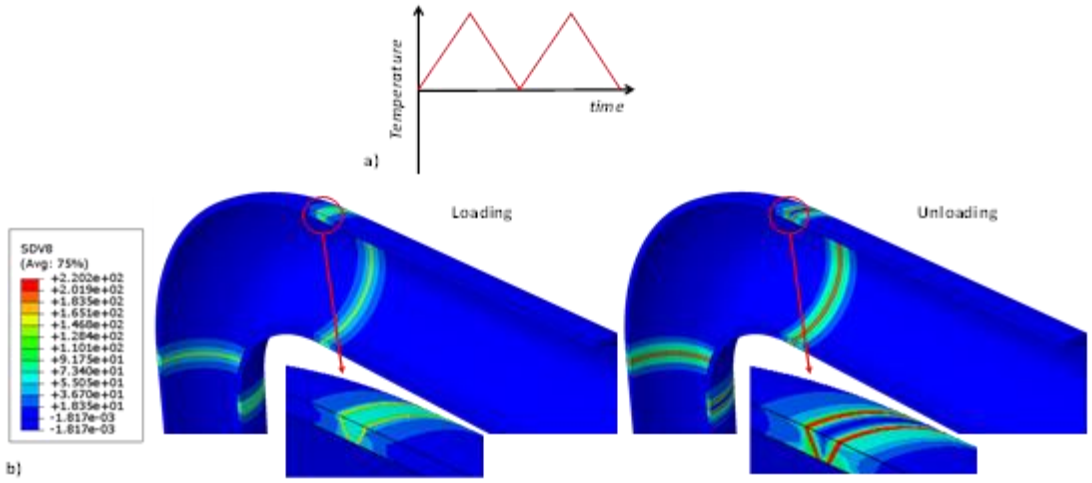

Figure 5-2 a) The loading cycle; b) Contours for von Mises stress history for isothermal loading and unloading.

For the non-isothermal loading, a high thermal gradient through the wall thickness of the elbow is considered with a temperature of 500 ℃ at the inside surface and 0 ℃ at the outside surface. The thermal gradient is cycled from zero to a maximum and back to zero over the time step. This is the most severe thermal loading condition during start-up. When the thermal gradient is imposed on the elbow, the results are quite different. During the loading cycle, the temperature at the inner surface of the component is higher compared to the outer surface. This results in larger stress accumulation at the outer side of the component, which is further exacerbated by the presence of the weldment, and larger plastic strain accumulation at the inner side of the component, due to the temperature-dependent material properties used. During the unloading phase, maximum stress accumulation is observed within the HAZ zone at the inner side.

Both the thermal loading conditions lead to different responses. They are presented in Figure 5-3. For the isothermal case, damage accumulation is only within the weldment region with the failure expected at the PM-HAZ interface. The total number of cycles is estimated to be 7250. On the other hand, the thermal gradient causes damage accumulation consistently throughout the structure but is exacerbated by the presence of weldment. The expected failure location shifts to the WM-HAZ interface. In this case, the number of cycles is reduced to 1010 cycles, which is only 1/7 times the former scenario. It is evident that the non-isothermal loading has a much more detrimental effect on the life of the components and this has been

observed in power plant components subject to severe thermal loads [26]. Only the non-isothermal loading condition is considered further for load combinations.

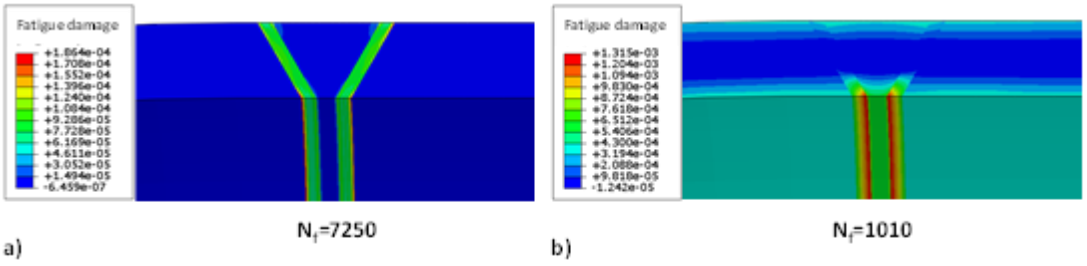

Figure 5-3 Failure mechanism a) isothermal; and b) non-isothermal loading.

5.2.3 Results for only pressure and only BM

Figure 5-4 presents the elastic solutions for pressure and BM loads. The pressure causes high stress at the intrados of the bend and the BM causes high stress at the crown.

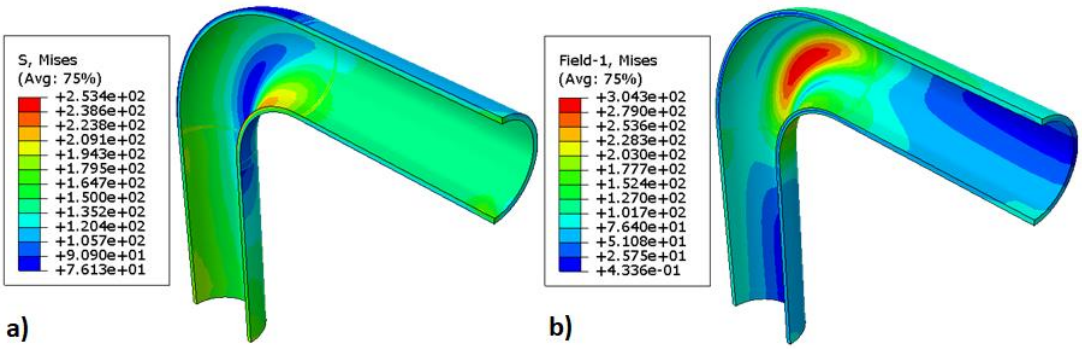

Figure 5-4 Elastic stress solutions for a) pressure; b) BM loads.

The damage mechanism for pressure only and BM only loads are quite different, though the presence of weldment has no effect. In both cases, the response is similar to that of a single PM material elbow. The fatigue damage distribution for both cases are presented in Figure 5-5. For cyclic BM loading, the maximum damage is spread in the middle of the bend at the crown region. With cyclic pressure, the maximum damage is at the intrados. Though maximum damage is confined in this region, certain damage is observed to spread away from the curvature along the straight pipe.

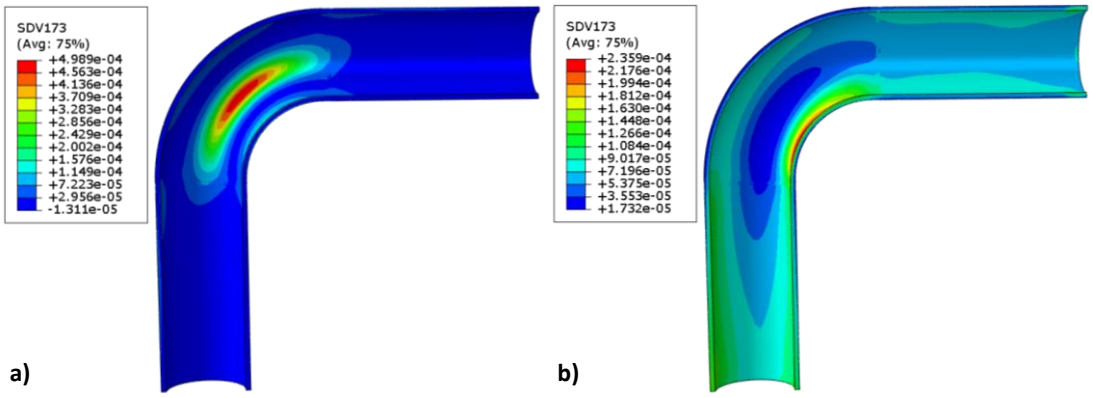

Figure 5-5 Contours for fatigue damage a) cyclic BM only; b) cyclic pressure only.

5.2.4 Results for BM and thermal gradient loading condition

The fatigue damage contour for in-phase (IP) BM and the thermal load is presented in Figure 5-6 (a). We can see that the weldment region has a damage accumulation, N_f=394, which is comparable with the damage accumulated at the crown, N_f=440. For out of phase (OP) BM and thermal loading condition, the damage accumulation at the middle of the bend at the crown is reduced and the damage is confined at the weldment region, N_f=425 (Figure 5-6 (b). This is because at the crown region the resultant stress during loading and unloading falls considerably such that it is much lower than the yield stress of the PM. Figure 5-7 presents the comparison of unloading von Mises stress for both IP BM and thermal loading, and OP BM and thermal loading scenarios.

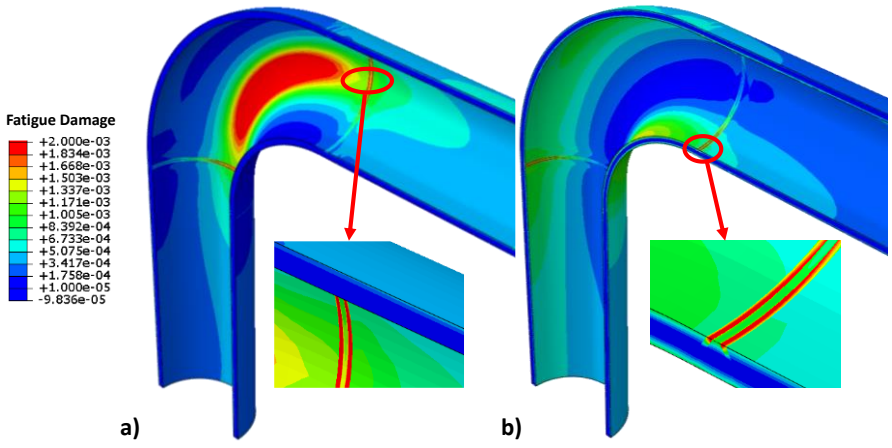

Figure 5-6 Contours for fatigue damage a) IP bending moment and thermal load; b) OP bending and thermal load.

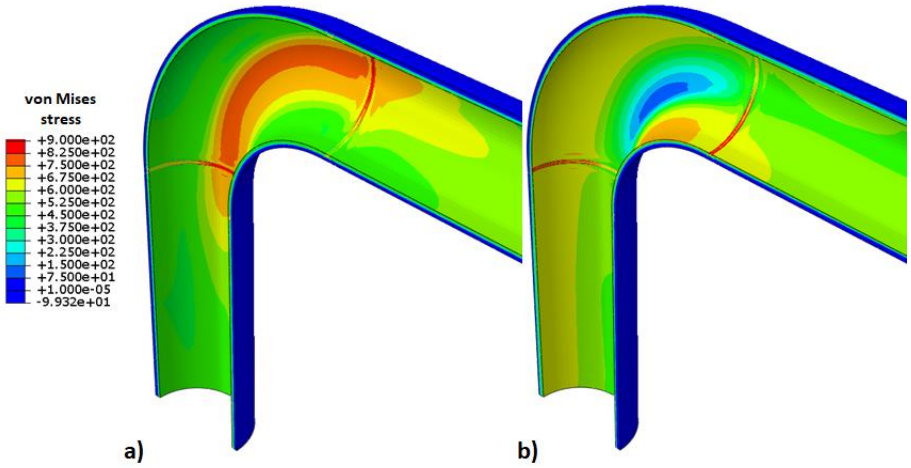

Figure 5-7 Contours for unloading von Mises stress a) IP BM and thermal load; b) OP BM and thermal load.

5.2.5 Results for pressure and thermal loading condition

It is interesting to note that for IP pressure and thermal load, the elastic strain range is comparable to the total strain range, Figure 5-8 (a & b). This indicates that the structure experiences elastic shakedown, which means HCF rather than LCF would be the damage mechanism in this case. Nevertheless, though elastic, high strain concentration is observed at the weldment region with the maximum peaking at the extrados of the elbow. For the OP pressure and thermal load, maximum damage, N_f=350 is observed in the weldment region similar to the OP BM and thermal load case, Figure 5-8 (c). However, here considerable damage accumulation is observed throughout the inner side of the pipe along the length. This is due to the hoop stress element of the inner pressure which has its effect throughout the length of the pipe.

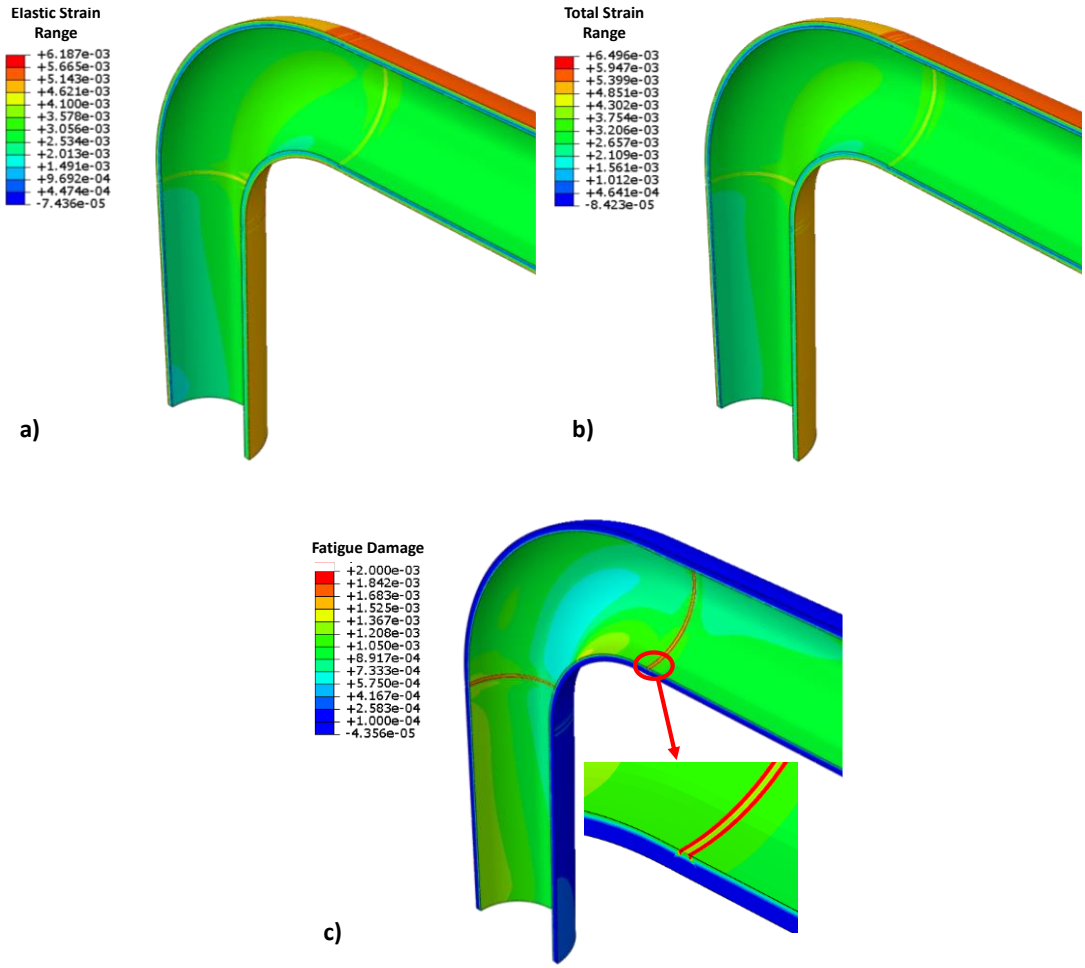

Figure 5-8 Contours for a) Elastic strain range-IP pressure and thermal load; b) Total strain range-IP pressure and thermal load; c) Fatigue damage-OP pressure and thermal load.

5.2.6 Results for BM and pressure loading condition

The cyclic BM and pressure in the absence of thermal load do have a critical impact on the structural integrity of the elbow. For both IP and OP loading conditions, different damage mechanisms are observed, though they are not within the weldment region. This is because at ambient temperature the change in the coefficient of thermal expansion doesn't induce any stress concentration in the weldment region. As material properties of the PM, HAZ and WM are within comparable range, BM and pressure do not create a stress notch at the weldment. Hence, in these loading scenarios, the behaviour of the elbow is comparable to that of a pure PM model. In the case of IP loading condition, substantial plastic strain is accumulated during

loading at the intrados and the crown of the elbow. This is not compensated during the unloading phase, which leads to ratchet strain accumulation, Figure 5-9.

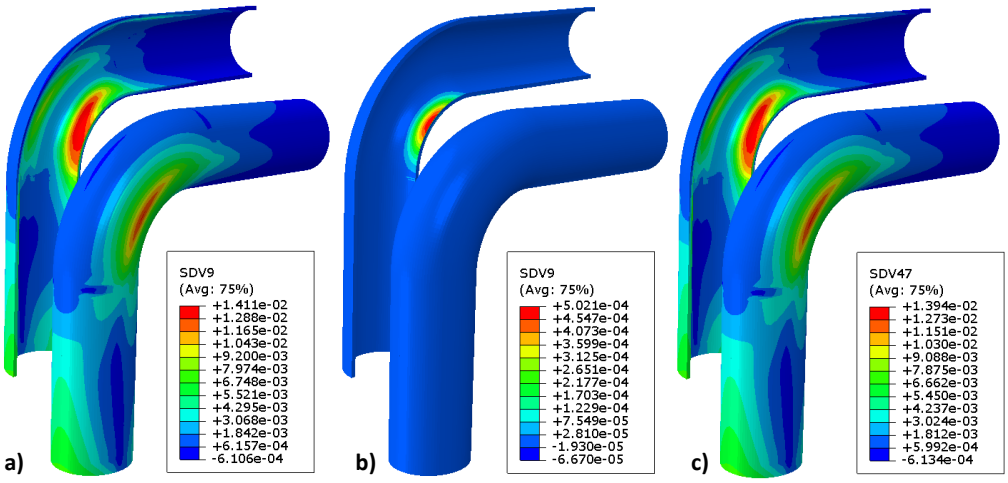

Figure 5-9 Contours for IP pressure and BM a) Plastic strain for loading; b) Plastic strain for unloading; c) Ratchet strain per cycle.

For OP loading condition, plastic strain accumulation occurs during both loading and unloading at the crown region of the elbow where maximum damage corresponds to N_f=2000, Figure 5-10. In the pure BM case, plastic strain accumulation was observed at the crown. The OP pressure augments this resulting in large strain accumulation.

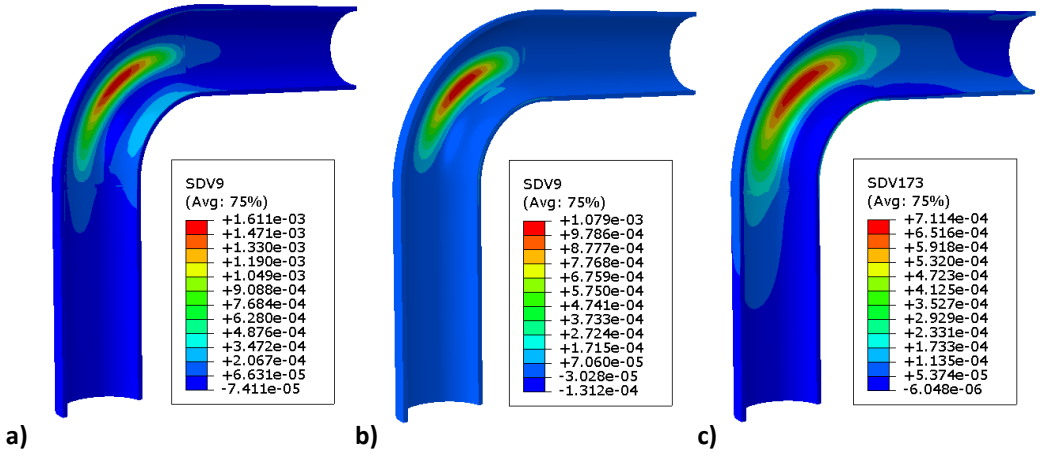

Figure 5-10 Contours for OP pressure and bending moment a) Plastic strain for loading; b) Plastic strain for unloading; c) Fatigue damage.

5.2.7 Results for BM, pressure and thermal loading condition

IP cyclic pressure and BM initiated a ratcheting mechanism at the intrados of the elbow. Applying an IP thermal load on the structure has two effects on the damage mechanisms; firstly, the application of the thermal load decreases the yield stress, which in turn exacerbates the ratcheting strain accumulated per cycle, Figure 5-11 (a). Secondly, LCF damage initiates at the crown, N_f=525 and at the weldment, N_f=650, Figure 5-11 (b).

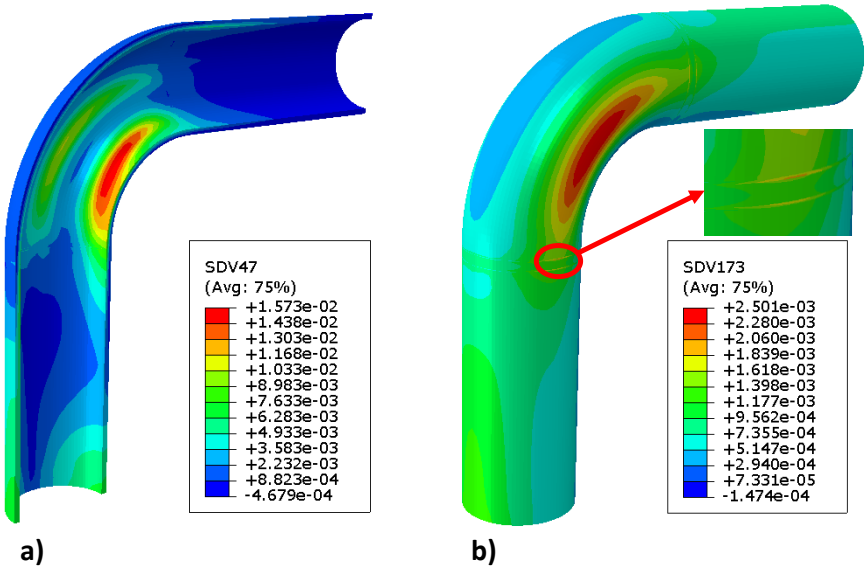

Figure 5-11 Contours for IP pressure, BM and thermal load a) Ratchet strain per cycle; b) Fatigue damage.

When IP thermal load and BM is imposed along with an OP pressure, maximum fatigue damage is observed at the weldment towards the inner side of the elbow though substantial damage is observed at the crown of the elbow also, Figure 5-12 (a). It should be noted that in the absence of thermal load, the maximum damage is observed at the crown of the elbow only. When IP thermal load and pressure is imposed with an OP BM, the maximum fatigue damage shifts to towards the intrados of the elbow, Figure 5-12 (b).

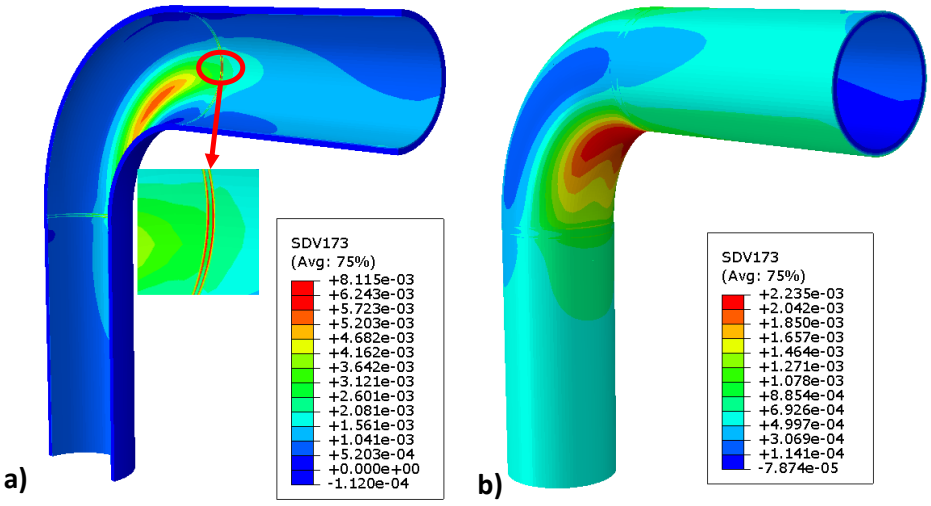

Figure 5-12 Contours for fatigue damage a) IP BM and thermal load with OP pressure; b) IP pressure and thermal load with OP BM.

5.2.8 Conclusion and summary for LCF of welded elbows under cyclic loading

Table 5-3 Comparison of results for welded elbow and single material (PM) model.

Loading Condition	PM model		Weldment Model	
	Position	Mechanism	Position	Mechanism
a) In Phase P & BM	Intrados	Ratcheting	Intrados	Ratcheting
b) Out of Phase P & BM	-	Elastic Shk	-	Elastic Shk
c) In Phase T & BM	Crown	LCF	HAZ-WM	LCF
d) Out of Phase T & BM	Intrados	LCF	HAZ-WM	LCF
e) In Phase T & P	-	Elastic Shk	HAZ-WM	LCF
f) Out of Phase T & P	Intrados	LCF	HAZ-WM	LCF
g) In Phase T, BM & P	Intrados /Crown	Ratcheting /LCF	Intrados/Crown and HAZ-WM	Ratcheting/ LCF
h) In Phase BM & P; Out of phase T	Intrados	LCF	HAZ-WM	LCF
i) In Phase BM & T; Out of phase P	Crown	LCF	HAZ-WM	LCF
j) In Phase P & T; Out of phase BM	Intrados	LCF	Intrados	LCF

The fatigue structural assessment against crack initiation is carried out for a welded elbow subjected to complex loading combinations by means of the LMM. Table 5-3 compares the location and prominent damage mechanism of the welded elbow with a single material elbow (PM only). For 7 of the 10 loading combinations considered the presence of the weldment either increased the fatigue damage, changed the critical location or caused both these effects. For loading scenarios (e), the presence of the weldment introduced LCF damage compared to a single material model which experienced elastic shakedown.

The bending moment has a larger effect compared to pressure. In the absence of thermal load, the response is similar to that of a single material model with the damage predominantly due to ratcheting for OP pressure-BM loading. With isothermal thermal loading, the structural response at the weldment region changes remarkably. This is even more prominent when non-isothermal loading is considered. Therefore, the thermal stress should be thoroughly considered during the integrity assessment of the welded elbows. The combination of non-isothermal thermal load with BM results in the increase of LCF and ratcheting damage simultaneously at the weldment region and crown region respectively.

5.3 Case study 2: Creep damage studies of a dissimilar welded flange

The effect of thermal stress on creep damage of a dissimilar welded flange (DWF) is analysed within this section. The creep damage is compared using both the DE and the TF methods. The temperature build-up within the structure is considered to occur in two ways, the first scenario is when the structure is gradually heated such that it experiences no thermal gradient or with a small thermal gradient before the commencement of creep dwell. The second scenario is when the fluid/steam is injected to the structure, and it experiences a temperature gradient before achieving a homogenous temperature throughout the structure and commencement of creep dwell. The temperature of injected fluid/steam will be less than the operating temperature else, it may lead to a very high thermal gradient leading to thermal shock. Hence, the thermal loading conditions studied in this section include a) homogenous thermal loading of 650 ℃ all the way to the start of creep dwell, hereafter referred to as load case NTG, and b) with the addition of a thermal gradient step, of internal temperature 150 ℃ and ambient outer temperature, during the initial loading before achieving a homogenous temperature of 650 ℃ across the structure and the commencement of creep dwell, hereafter

referred to as load case TG. A DWF joint is opted as it provides a basis for a comprehensive discussion considering the material mismatch and the geometric irregularity.

5.3.1 Creep constitutive and creep damage models

The Norton creep model is adopted for assessing the creep strain within this study. The uniaxial form of which is given by:

$$\dot{\varepsilon}^{cr} = A\sigma^{n} \tag{5-5}$$

where $\dot{\varepsilon}^{cr}$ is the creep strain rate, σ is the applied stress ; A, and n are the creep constants.

The creep damage is discussed considering both DE and TF models. R5 recommends the use of DE method for the calculation of creep damage. The uniaxial creep damage per cycle is calculated by:

$$d_C^{DE} = \int_0^{t_h} \frac{\dot{\bar{\varepsilon}}_C}{\bar{\varepsilon}_C(\dot{\bar{\varepsilon}}_C,\ T)} dt \tag{5-6}$$

where $\dot{\bar{\varepsilon}}_C$ is the instantaneous creep strain rate and $\bar{\varepsilon}_C(\dot{\bar{\varepsilon}}_C,\ T)$ is the creep ductility which is a function of the creep strain rate and temperature [41]. The creep ductility has a lower shelf, ε_L, at lower strain rates and an upper shelf, ε_U, at higher strain rates. In between the ε_U and ε_L, the transition region may be defined as a function of the creep strain rate. As such the $\bar{\varepsilon}_C$ may be defined as:

$$\bar{\varepsilon}_C = min\left[\varepsilon_U, Max\ \left(\varepsilon_L, B^{DE}{\dot{\varepsilon}_C}^{n^{DE}}\right)\right] \tag{5-7}$$

where B^{DE} and n^{DE} are material constants. Equation (5-7) may be further improved to consider the effect of multiaxial stress by including the multiaxial ductility factor (MDF) defined as:

$$\bar{\varepsilon}_{MDF}(\dot{\bar{\varepsilon}}_C, T) = \bar{\varepsilon}_C(\dot{\bar{\varepsilon}}_C, T)\ \ MDF = \varepsilon_d(\dot{\bar{\varepsilon}}_C, T) exp\left[p\left(1 - \frac{\sigma_1}{\bar{\sigma}}\right) + q\left(\frac{1}{2} - \frac{3\sigma_H}{2\bar{\sigma}}\right)\right] \tag{5-8}$$

where σ_1 is the principal stress, σ_H is the mean or hydrostatic stress; p and q are constants dependent on the material and temperature. Creep damage per cycle is calculated with respect to σ_{avg}, the average stress, over the dwell period using the TF method as:

$$d_c^{TF} = \int_0^{\Delta t} \frac{dt}{t_f(\sigma_{avg}, T)} \tag{5-9}$$

The creep rupture time, t_f can be represented using the reverse power law, with creep constants B^{TF} and k^{TF} as:

$$t_f = B^{TF} \sigma_{avg}^{-k^{TF}} \tag{5-10}$$

5.3.2 DWF geometry and material parameters

The flange and pipe is of SS304 material and weld material is SS347. The pipe considered has an outer diameter of 273 mm and a thickness of 30 mm which is within the realistic range of main steam pipe in UK power plants [91]. The flange dimensions matching the pipe dimension is selected from ASME B 16.5 [92] and corresponds to a rating of 2500. The plastic response is modelled using the EPP assumption. Considering the geometric symmetries, an axisymmetric model is used for the analysis with plain conditions imposed to the end of the pipe. The axisymmetric model with key dimensions are presented in Figure 5-13. The mesh consists of 5451 elements with the area at weldment highly refined. CAX8R 8-node biquadratic axisymmetric quadrilateral elements with reduced integration are used for structural analysis and DCAX8 8-node quadratic axisymmetric heat transfer quadrilateral elements with reduced integration are used for the heat transfer analysis.

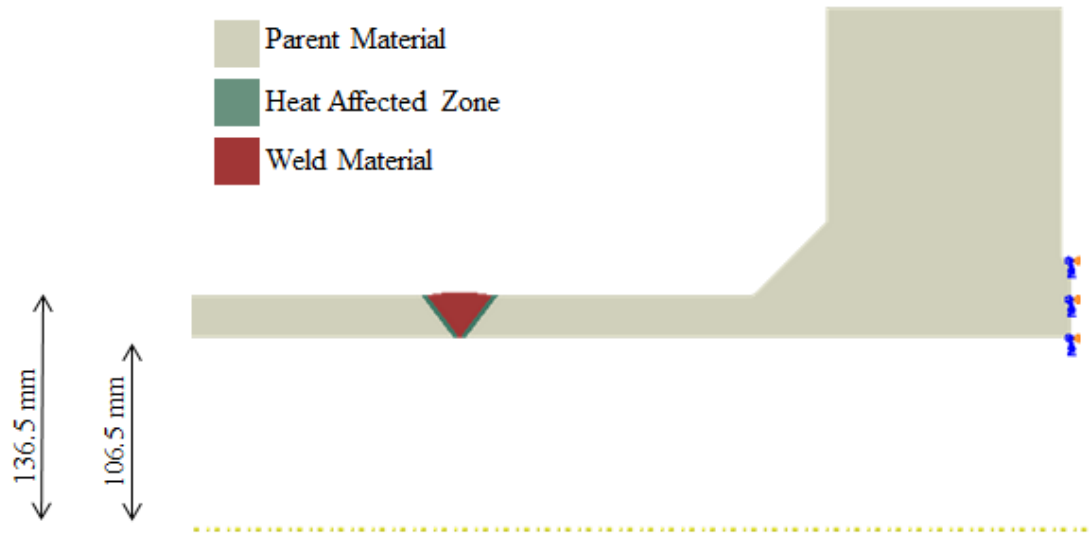

Figure 5-13 Axisymmetric DWF model with key dimensions.

The data required for the generation of creep constants for the PM and WM region are obtained from the NIMS database [93], [94]. Hossein A. and Tahami F. V. have presented the mechanical and creep data for the HAZ of an SS304 weldment in [95], [96]. Using a similar trend and the relevant HAZ data has been generated for use within this study. All the material properties within the study are presented in Table 5-4 to Table 5-7. Temperature-dependent yield stresses are used for the analysis.

Table 5-4 Temperature-dependent yield stress for DWF study.

℃	0	100	200	400	550	600	650	700
σ_y^{PM}(MPa)	260	236	201	167	160	151	137	131
σ_y^{HAZ}(MPa)	205	186	158	132	126	119	108	98
σ_y^{WM}(MPa)	238	238	200	173	163	162	156	142

Table 5-5 Coefficient of thermal expansion for DWF study.

℃	20	100	650
α^{PM}(x 10^{-5}℃$^{-1}$)	1.69	1.7	1.75
α^{HAZ}(x 10^{-5}℃$^{-1}$)	1.95	2.0	2.1
α^{WM}(x 10^{-5}℃$^{-1}$)	1.79	1.8	1.85

Table 5-6 Parameters for Norton creep equation at 650 °C for DWF study.

	$A(MPa^{-n}h^{-1})$	n
PM	2.79×10^{-22}	9.03
HAZ	2.27×10^{-21}	8.27
WM	5.46×10^{-21}	7.54

Table 5-7 Parameters for creep damage calculation for DWF study.

	TF model		DE model			
	B^{TF}	k^{TF}	ε_U	B^{DE}	n^{DE}	ε_L
PM	4.34×10^{13}	4.89	0.011	0.098	0.3423	0.000157
HAZ	3.62×10^{14}	5.15	0.011	0.274	0.3929	0.000157
WM	2.02×10^{17}	6.17	0.020	0.024	0.1389	0.001512

5.3.3 Results and discussions

For baseline discussions, a creep dwell of 100 hours is considered. Figure 5-14 presents the start of dwell stress for both of the NTG and TG loading conditions. For load condition NTG, stress is concentrated only within the weldment region. For load condition TG, the thermal gradient during the initial loading phase enhances the area under high stress in the HAZ and induces stress concentration at the flange neck. This is because of the geometric irregularity, and as temperature-dependent yield stress is used, the outer part of the pipe/flange experiences lower temperature leading to larger stress concentration. After the temperature becomes homogenous and the stress redistributes itself and the magnitude of stress concentrated at these regions reduces.

In line with the regions were maximum stress and subsequent relaxation is observed, for NTG loading creep strain accumulation is observed only within the HAZ while for TG loading, creep strain accumulation is observed within the HAZ and the flange neck, as indicated in . For TG loading, it is further observed that for shorter dwell the creep strain at the flange neck is not significant, but at larger dwell, the creep strain becomes more prominent spreading towards the inner side of the pipe. Nevertheless, for larger dwell periods the creep strain accumulation at both the weldment and flange neck is within a comparable range. Considering the severity of the imposed loading condition this is realistic.

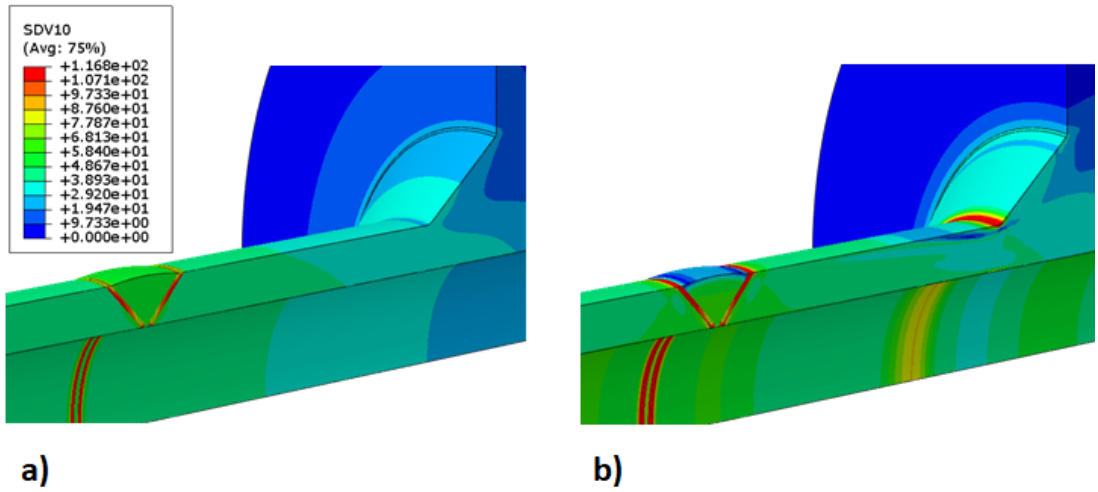

Figure 5-14 von Mises stress at the start of dwell a) NTG loading; b) TG loading.

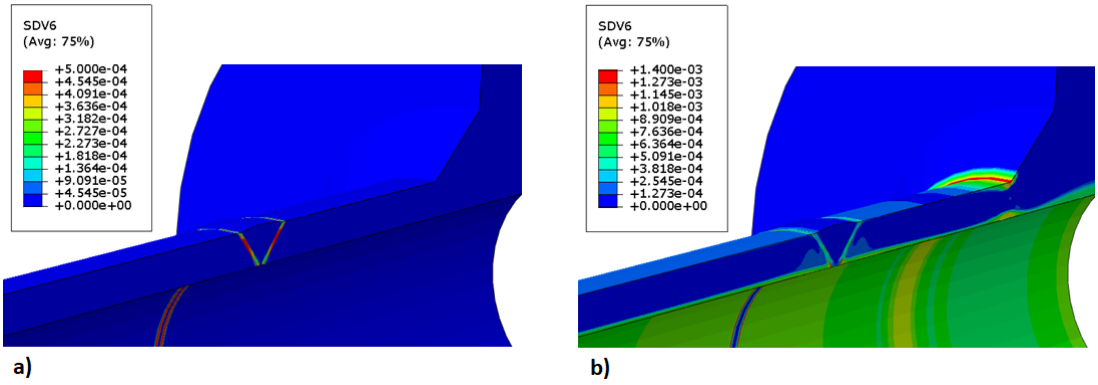

Figure 5-15 Effective creep strain for dwell of 100 hrs a) NTG loading; b) TG loading.

Figure 5-16 presents the TF and DE creep damage for dwell of 100 hours considering NTG loading. It can be observed that the spread of creep damage is different. The DE method which is inherently a strain-based method indicates substantial creep damage only within the HAZ where large creep strain is observed. TF method on the other hand, which is stress-based, predicts considerable creep damage within the PM region adjacent to the HAZ. Table 5-8 provides the comparison between the TF and DE damage model for a dwell time of 10, 100 and 1000 hours. It can be seen that the DE model predicts a larger creep compared to the TF method. Takahashi *et al.*, in their work in [97] have reported that for SS316 stainless steel, for smaller total strain ranges, TF tends to predict non-conservative results. Considering SS304 and SS347 falls within the same branch of austenitic steel a similar trend is observed here.

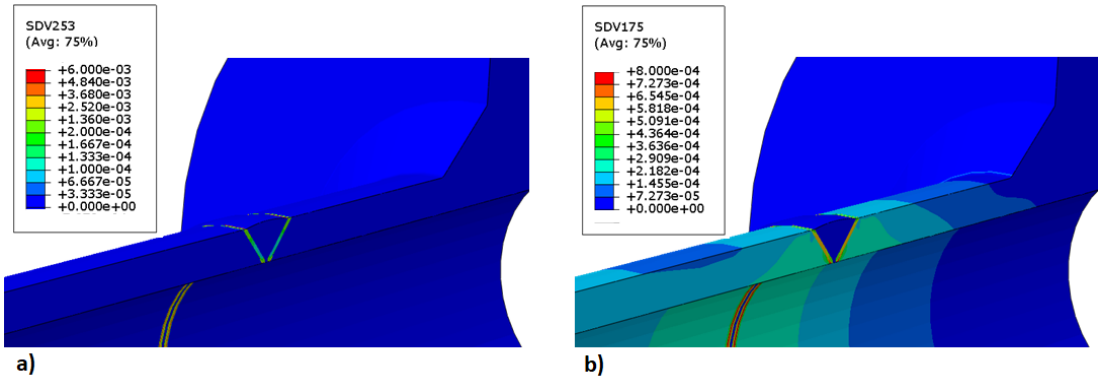

Figure 5-16 Creep damage distribution for NTG loading a) DE model; b) TF model.

Table 5-8 Comparison of creep damage for NTG loading.

Dwell	DE	TF
10	0.0032	0.0004
100	0.0048	0.0011
1000	0.012	0.0032

For TG loading condition, the critical locations for the TF model (Figure 5-17 (a)) remains within the same region as NTG loading, though substantial damage is observed at the flange neck also. Considerable stress relaxation is observed within the critical location with an increase in the dwell time but the increase in the creep damage is only marginal as evident from Figure 5-17 (b). In effect, for both the TG and NTG loading conditions, TF approach predicts high non-conservative results. For instance, consider the dwell time of 1000 hours for TG loading, TF predicts a damage of 0.0043, this seems to be highly unlikely considering the harsh loading condition imposed. This non-conservatism can be attributed to the relatively lower start of dwell stress and the absence of using multiaxial stress. Similar results are presented in [98] where the low start of dwell predicted highly non-conservative results. The effect of multiaxial stress is discussed in the next section with a case study.

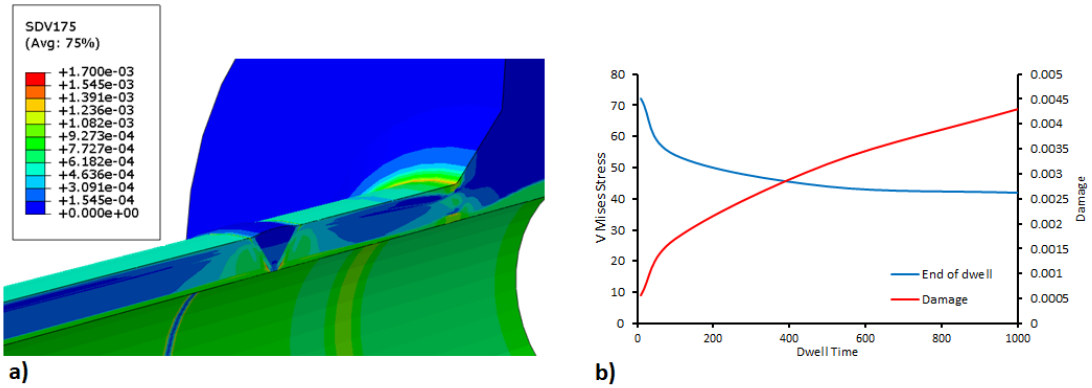

Figure 5-17 For TG loading a) TF Creep damage distribution; b) Stress relaxation and TF damage at the critical location with increasing dwell time.

The most interesting results are obtained in the DE model in TG loading. The critical location, in this case, shifts to the centre of the pipe at the HAZ-PM interface as shown in Figure 5-18 (a). Tanner, D. *et al.* [99] has presented similar results in the case of P91 weld where the creep damage initiates within the centre of the pipe weldment for lower end axial loads wherein the maximum principal stress direction is similar to the hoop stress direction. It should be noted that the shift of the maximum creep damage location is despite maximum creep strain accumulation at the PM-HAZ interface towards the inner side of the pipe. The shift in the location is driven by the MDF which accounts for the multiaxial stress, Figure 5-18 (b), arising due to the thermal gradient during loading and the inhomogeneous material composition in the weldment. Compared to the PM, the HAZ has a much larger Norton creep law constant. In this case during the creep dwell the deformation of the HAZ will be restricted by the PM leading to significant triaxial stress state at their interface. Similar results have been reported in [100]–[102] where prominent creep damage was observed within the mid-thickness of the component at the HAZ due to the triaxial stress state. Without the consideration of MDF, the maximum creep damage is at the PM-HAZ interface towards the inner side of the pipe where maximum creep strain is observed. Further DE predicts minimal damage accumulation at the flange neck. Compared to the damage predicted by the TF model, DE predicts much higher damage, as reported in Table 5-9. A reason for this is the low start of dwell stress. Similar results are reported in [40] where low initial stress predicted conservative results while high initial stress predicted non-conservative results.

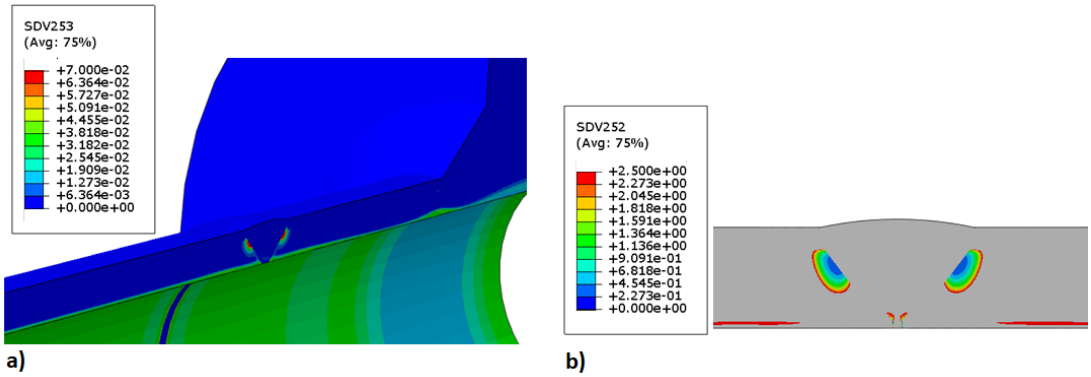

Figure 5-18 For TG loading a) DE Creep damage distribution; b) MDF spread.

Table 5-9 Comparison of creep damage for TG loading.

Dwell	DE	TF
10	0.016	0.0006
100	0.043	0.0017
1000	0.082	0.0043

5.3.4 Conclusion and summary for creep damage studies for DWF study

The creep damage assessment of a DWF has been carried out using both the TF and DE methodologies. For all the cases the effect of the mechanical load is ignored while two types of thermal loading configurations are analysed. The thermal loading configurations includes an isothermal heating process before the commencement of creep dwell and the addition of a thermal gradient step during loading. The LMM UMAT code is modified to accommodate both the damage models and post-process the results.

The addition of thermal gradient step during loading led to a higher damage prediction. This signifies the importance of avoiding such loading steps is a power plant. For all the loads and dwell periods consider, the start of dwell stress was relatively low but well in the range expected in power plants. This low start of dwell stress led to non-conservative creep damage by TF but large creep damage by DE. With the TF model, the increase in the dwell time, though relaxed the stress had only a minimal effect on the creep damage increase. The most interesting result was observed in the TG loading case where the MDF shifts the creep damage location, by DE method, to the mid-thickness of the weldment. This reiterates the importance

of considering the effect of multiaxial stress while conducting creep damage analysis for welded structures.

5.4 Case study 3: Creep damage evaluation considering multiaxial stress and compressive dwell

Structures are at large designed based on uniaxial creep data, however, a change in the geometry or the presence of multi-material such as MMCs or welds induces multi-axial stress. In such cases, the creep damage calculations must account for the multiaxial effects too [103]. They also help in reducing the pessimism involved in the creep damage calculation at regions experiencing compressive dwell.

The effects of compressive dwell on creep damage is an area that has had only limited studies as in most cases it has been reported that tensile dwell is more prominent and damaging. An example of the converse, as discussed by Borkowski, L.B. and Staroselsky [104], would be of a gas turbine blade which experiences OP TMF, wherein localised areas are restricted to expand by the surrounding cooler region inducing compressive loading and consequently compressive creep accumulation. Similarly in the cases of welded structures, during a hold period, certain areas experience compressive dwell whereas other areas experience tensile dwells [105]. Under such circumstances, damage evaluation must be done considering multiaxial and compressive stress to accurately calculate the safe life. The effect of compressive dwell is quite complex and varies from material to material [106]–[108]. It should be noted that for compressive dwells the deformation is usually due to dislocation motion as any porosity or cracks remain closed [104]. Figure 5-19 presents a pictorial comparison between stress-strain evolution for tensile and compressive dwell holds.

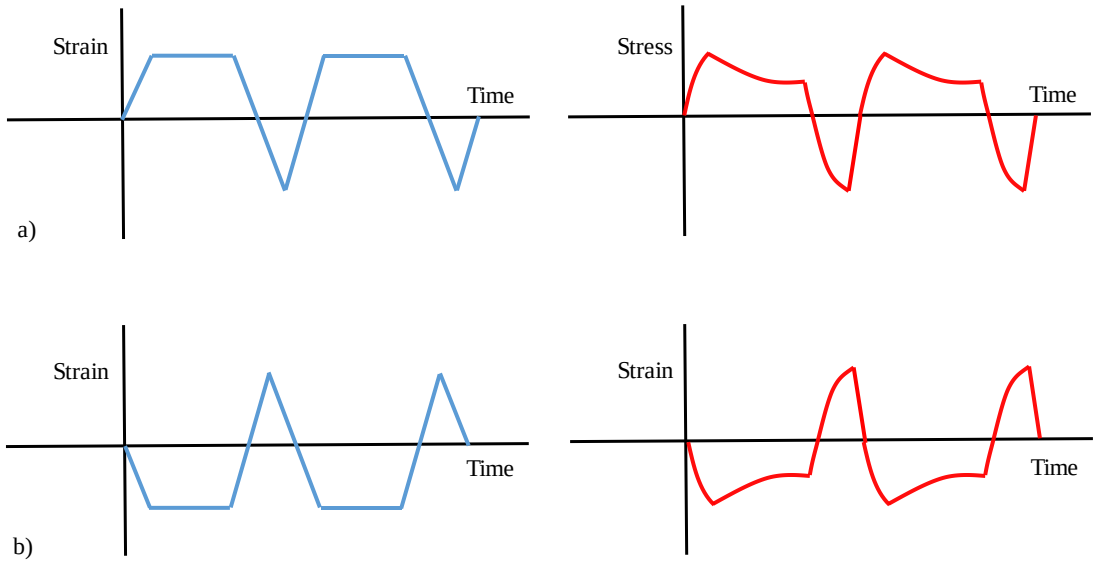

Figure 5-19 Stress-strain evolution for a) tension creep hold; b) compression creep hold [109].

5.4.1 Creep constitutive and creep damage models

The Norton-Bailey model which accounts for both the primary and secondary creep strain is used to model the creep behaviour. The uniaxial form of Norton-Bailey model is given by:

$$\dot{\varepsilon}^{cr} = A\sigma^n t^m or\ \varepsilon^{cr} = \left[A/(m+1)\right]\sigma^n t^{m+1} \tag{5-11}$$

where $\dot{\varepsilon}^{cr}$ is the creep strain rate, σ is the applied stress, t is the time; A, n and m are the creep constants.

The creep damage is calculated by the TF approach with the rupture stress modified as per the recommendation of ASME and RCC-MR for multiaxial and compressive stress. ASME recommends calculating the rupture stress as:

$$\sigma_{rup} = \bar{\sigma} exp\left[0.24\left(\frac{3\sigma_H}{\sqrt{\sigma_1^2+\sigma_2^2+\sigma_3^2}} - 1\right)\right] \tag{5-12}$$

RCC-MR recommends calculating the rupture stress as:

$$\sigma_{rup} = 0.133 \times 3\sigma_m + 0.867\bar{\sigma} \tag{5-13}$$

where σ_1, σ_2 and σ_3 are the principal stresses, $\bar{\sigma}$ is the von Mises stress and σ_m is the mean or hydrostatic stress.

5.4.2 Calculation of instantaneous stress during the creep dwell

The LMM eDSCA calculates the end of dwell stress at steady-state directly, but this is not sufficient for the ASME or RCC-MR creep damage calculation as the dwell stress, principal stress and mean stress history is required. Hence the UMAT is modified as per the recommendations/suggestions in [62] to calculate the instantaneous end of dwell stress and instantaneous effective creep strain increment as:

$$\bar{\sigma}_{c,i} = \left\{ \bar{\sigma}_{s,i}^{-n+1} + \frac{1}{Z}\left(\frac{n-1}{m+1}\right) B_i \bar{E} \Delta t_i^{m+1} \right\}^{\frac{-1}{n-1}} \tag{5-14}$$

$$\Delta\bar{\varepsilon}_i^c = \frac{B_i(n-1)\Delta t_i^{m+1}\left(\bar{\sigma}_s - \bar{\sigma}_{c,i}\right)}{\left(\frac{1}{\bar{\sigma}_{c,i}^{n-1}} - \frac{1}{\bar{\sigma}_s^{n-1}}\right)(m+1)} \tag{5-15}$$

where $\bar{\sigma}_{s,i}$ is the instantaneous start of dwell stress, $\bar{\sigma}_{c,i}$ is the instantaneous end of dwell stress and B_i is the creep coefficient for the instantaneous time increment. The principal stress history and mean stress history is then calculated from the dwell stress history. They are then used as inputs for the creep damage calculations. The instantaneous creep damage is calculated as per ASME and RCC-MR recommendations and summed over the dwell period to calculate the total creep damage. The code is also capable of identifying the different zones within the weldment and applies the relevant material data to the respective zone for the analysis.

5.4.3 Geometry and material parameters for multiaxial stress studies

The pipe geometry used in this study is shown in Figure 5-20. It is comparable to a realistic steam pipe dimension in the UK power plant, with an outer diameter, o.d. = 287.6 mm and thickness, t = 33.8 mm. The plastic response is modelled using the EPP assumption. The residual stresses caused by the welding process is nullified by PWHT such that its effect on the creep behaviour of the welded pipe can be neglected.

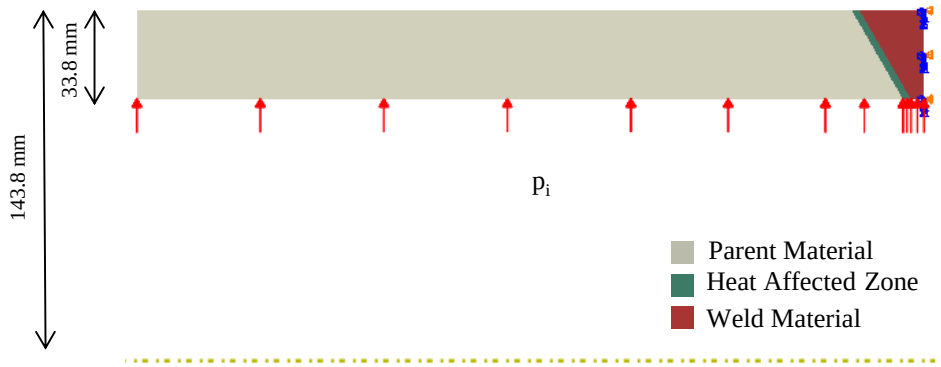

Figure 5-20 Axisymmetric FE model for the pipe weld.

Material parameters, creep constitutive parameters and creep damage parameters are listed in Table 5-10 to Table 5-12. The base values at 550 ℃ are obtained from [110], [111] and the data for other temperatures are traced considering the trend presented in NIMS. An axisymmetric model is adopted for the analysis, Figure 5-20. CAX8R 8-node biquadratic axisymmetric quadrilateral elements with reduced integration is used for structural analysis and DCAX8 8-node quadratic axisymmetric heat transfer quadrilateral elements with reduced integration is used for the heat transfer analysis, with a total no of elements of 3, 350.

Table 5-10 Temperature-dependent material parameters for multiaxial stress study.

Temp. [℃]	0	500	550	600	650	750
Yield stress (MPa)						
σ_y^{PM}	634	301	271	266	257	245
σ_y^{HAZ}	677	321	289	284	274	262
σ_y^{WM}	721	342	308	303	292	279
Young's modulus (GPa)						
E^{PM}	207	172	166	160	154	130
E^{HAZ}	199	165	160	154	148	125
E^{WM}	158	131	127	122	117	99

Table 5-11 Parameters for Norton-Bailey model for multiaxial stress study.

	$A\ (MPa^{-n}/h^{m+1})$			n			m
Temp. [℃]	575	600	625	575	600	625	
PM	2.97×10^{-19}	1.33×10^{-19}	6.01×10^{-20}	6.27	6.78	7.29	0.5
HAZ	2.96×10^{-21}	1.33×10^{-18}	5.99×10^{-22}	7.27	7.86	8.45	0.525
WM	7.17×10^{-23}	7.76×10^{-23}	8.34×10^{-23}	8.26	8.93	9.60	0.55

Table 5-12 Parameters for creep damage calculation for multiaxial stress study.

	B^{TF}			k^{TF}		
Temp. [℃]	575	600	625	575	600	625
PM	$1.74\times10^{+26}$	$1.39\times10^{+26}$	$1.10\times10^{+26}$	10.08	10.53	10.96
HAZ	$1.03\times10^{+28}$	$8.22\times10^{+27}$	$6.56\times10^{+27}$	11.03	11.52	11.99
WM	$6.77\times10^{+29}$	$7.07\times10^{+29}$	$7.36\times10^{+29}$	11.98	12.51	13.03

5.4.4 Results for creep damage evaluation

It is considered that during start-up and shut-down, the temperature increment within the pipe is gradual such that no significant temperature gradient occurs and the temperature is homogeneous across the pipe. Using the LMM shakedown-ratchet analysis a shakedown-ratchet limit interaction curve is calculated, as shown in Figure 5-21, to provide a benchmark to define reasonable cyclic load conditions for the creep damage assessment of the welded

pipe. A reference uniform cyclic temperature, ranging from 0 °C to θ_0 (where θ_0 = 600 °C), and an internal pipe pressure (p_o) of 25 MPa is applied over the entire model. The ordinate and abscissa axes in Figure 5-21 show the temperature and mechanical load respectively, normalised to the reference temperature and internal reference pipe pressure.

The cyclic load points C1, C2 and C3 which lie within the reverse plasticity region are chosen for further discussions. The dwell time considered is of 100 hours. Figure 5-22 (a) & (b) presents the equivalent stress distribution at the start and end of creep dwell respectively for cyclic load point C2. During loading, the maximum equivalent stress with yielding occurs at the HAZ-WM interface towards the outside of the pipe and at the HAZ-PM interface towards the inside of the pipe. During the creep dwell, the stresses relax throughout the HAZ with the stress relaxing to approximately one-third at these two locations and the maximum equivalent stresses shifts to within the PM. Figure 5-22 (c) presents the effective creep strain with the maximum effective creep strain occurring at locations of maximum equivalent stress. The two locations are identified as A* and B*.

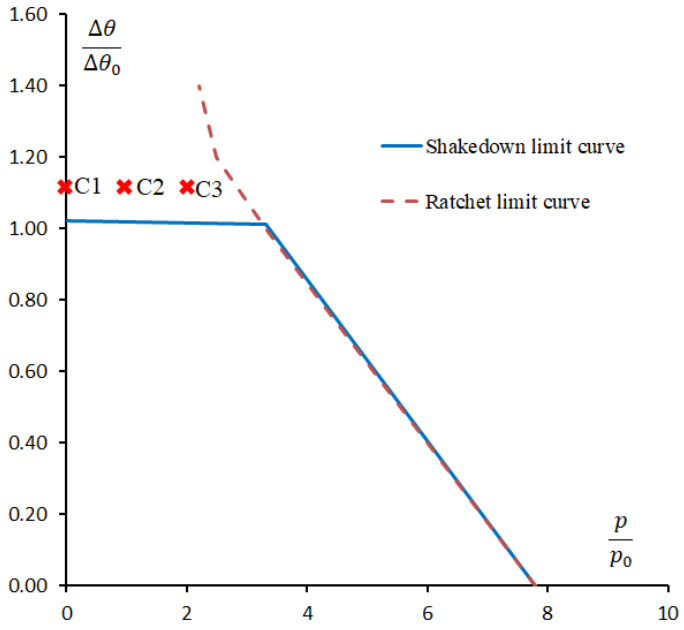

Figure 5-21 Shakedown and ratchet limit interaction curve.

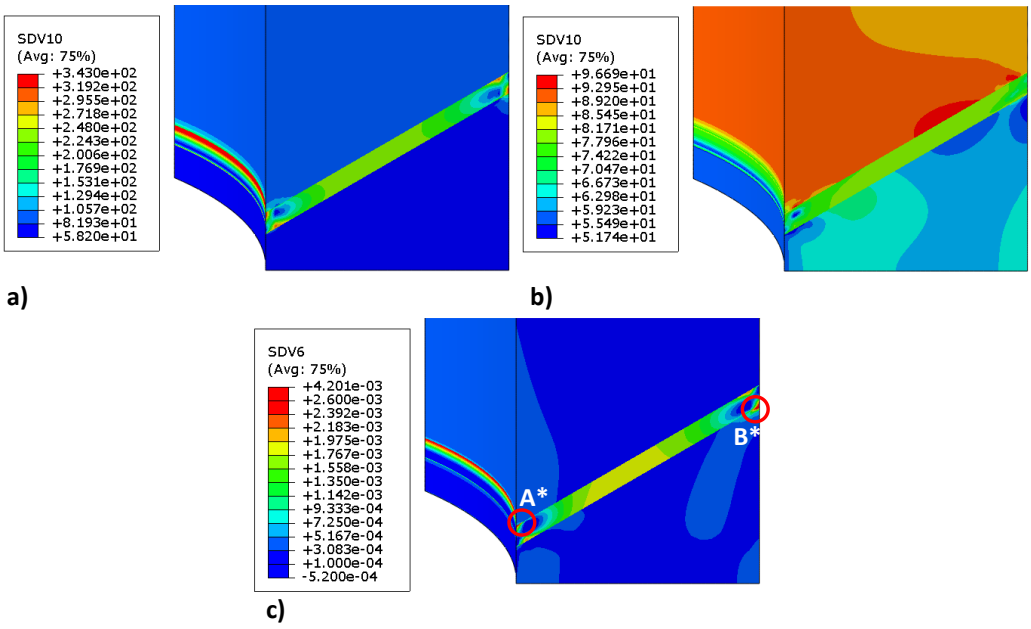

Figure 5-22 Cyclic load point C2-Contours for a) equivalent stress distribution for loading; b) equivalent stress distribution for unloading; c) effective creep strain increment.

The sign/direction of the equivalent stress is accessed using the Rule of Sign for Dominant Principal Direction [112]. For A*, the minimum principal stress shows the maximum stress magnitude among the three principal stress components and is in compression. Whereas, at B* the medium principal stress shows the maximum stress magnitude among the three principal stress components and is in tension. Hence, it can be deduced that A* experience compressive loading while B* experiences tensile loading. The high temperature coupled with the difference in the coefficient of thermal expansion, causes compression at A* as the applied load is dominated by the compressive thermal stress while at B* the load is dominated by tensile thermal stress. The creep dwell then causes inelastic strain increase in compression at A* and in tension at B* as the stresses relax.

Experimental lab data available for comparison with the results from the LMM analysis is limited, hence inelastic step-by-step (SBS) analysis is done. Table 5-13 shows a comparison between SBS and LMM results for stress and strain at B* for a dwell period of 100 hours. The results provided by LMM are comparable and close to the ones given by SBS analysis. Also, the computational time required by LMM was far less than SBS. The configuration of the system used for analysis was Intel(R) Core(TM) i7-6700 CPU @ 3.40 GHz.

Table 5-13 Equivalent stress and strain at B* for the LMM and SBS analyses for creep dwell of 100 hours.

	Stress – loading (MPa)	Stress-Creep Dwell (MPa)
SBS	279	83.2
LMM	279.5	82.3

	Plastic Strain at loading	Creep Strain	Computational Time (seconds)
SBS	4.32×10^{-03}	2.98×10^{-03}	5200
LMM	4.9×10^{-03}	3.2×10^{-03}	660

5.4.4.1 Effect of increasing mechanical load

The effect of internal pipe pressure is analysed to understand the variation in the compressive and tensile creep damages. From Figure 5-21, cyclic load point C1 indicates only thermal load while cyclic load point C2 indicates an increase in internal pipe pressure of 25 MPa, which is the recommended working pressure for the welded pipe, and cyclic load point C3 indicates a higher working pressure of 37 MPa. Pressure above this causes creep rupture. Table 5-14 presents a comparison between the creep strain, ASME and RCC-MR damages for the considered load points. It should be noted that for all the cases the creep strain accumulated is comparable at A* and B* but the damage is prominent at the tensile stress dominated B*. This highlights the importance of using multiaxial stress for creep damage calculations in welds. Though both RCC-MR and ASME predict similar damages (generally well within 10%), RCC-MR predicts slightly larger damage for compressive loads while ASME predicts slightly larger damage for tensile loads.

Table 5-14 Comparison of ASME and RCC-MR creep damage at critical elements for increasing pressure.

	Creep Strain		RCC-MR		ASME	
	A*	B*	A*	B*	A*	B*
A1	0.0013	0.0013	0.0007	0.0007	0.0001	0.0002
A2	0.0030	0.0032	0.0008	0.0020	0.0001	0.0033
A3	0.0050	0.0050	0.0020	0.0150	0.0010	0.0190

5.4.4.2 Effect of the hoop to axial stress ratio

The effect of axial load is investigated by introducing different end loads, σ_{ax}. The value of which is defined using an axial stress ratio parameter, k_a.

$$k_a = \frac{\sigma_{ax} - \sigma_{ax}^c}{\sigma_{mdh} - \sigma_{ax}^c} \tag{5-16}$$

where, σ_{mdh} is the mean diameter hoop stress; σ_{ax}^c is the axial stress due to the internal pressure only, in a closed-end situation. k_a can range from 0 to 1 only as permitted by piping design codes [99].

As to be expected, with increasing axial load, the creep damage within the structure increases. Even in the presence of additional axial load, A* indicated that compressive stress was more dominant within this region. The increase in axial load for both the applied internal pressure had a larger effect on B* compared to A* as indicated in Table 5-15. This is because, despite the presence of axial load, the stresses due to the difference in the coefficient of thermal expansion and thermal load is more dominant at A* resulting in lower rupture stress. While at B* the axial load combines with the already present tensile stress resulting in larger rupture and creep damage. The difference in the creep strain and creep damage between A* and B* are over 10%. Finally, for the most extreme case with P=37 MPa and k_a=1, creep rupture is predicted from B* region. Here again, the RCC-MR predicts slightly larger damage for compressive loads while ASME predicts slightly larger damage for tensile loads.

Table 5-15 Comparison of ASME and RCC-MR creep damage at critical elements for increasing k_a.

Pressure	k_a	Creep Strain		RCC-MR		ASME	
		A*	B*	A*	B*	A*	B*
25 MPa	0	0.003	0.0032	0.0004	0.002	0.0001	0.0033
	0.5	0.0032	0.0042	0.0009	0.0041	0.0006	0.0068
	1	0.006	0.011	0.0062	0.034	0.0038	0.053
37 MPa	0	0.01	0.01	0.002	0.02	0.001	0.02
	0.5	0.02	0.03	0.03	0.20	0.03	0.28
	1	0.19	0.26	-	CR	-	CR

5.4.5 Conclusion and summary for creep damage evaluation considering multiaxial stress and compressive dwell

A creep damage assessment considering multiaxial and compressive stress has been carried out for the welded pipe with the LMM UMAT modified to facilitate this. The creep behaviour is modelled using the Norton-Bailey relationship. For all the cases without any additional axial load, maximum effective creep strain accumulation is observed at two distinct locations. It is identified that one of the locations experience tensile stress while the other experience compressive stress. The creep damage at the tensile region was much more prominent in all the cases except for with a low dwell hold of 1 hour. This highlights the importance of using multiaxial and compressive stress effect in structures such as welds where the inhomogeneity of the material is prominent. Both the results, through RCC-MR and ASME calculations, show reasonable comparison within a 10 % range. A semi-circular crack is expected to initiate at the interface between the WM and HAZ towards the outer side of the pipe.

To understand the effect of pressure, the analysis is carried out considering only thermal load and with a higher pressure. In both instances, the maximum creep strain accumulation at the tensile and compressive stress dominated regions was within a comparable range. The damage though as expected increased within the increasing load. The damage at the tensile stress region was much more prominent. At the highest pressure applied, both ASME and RCC-MR predict the damage at the tensile stress region to be over 7 times the damage at the compressive stress dominant region.

To investigate the effect of end load, the axial stress ratio, k_a, is varied from 0 to 1 for two pressure values. The creep damage significantly increased when an additional axial load was applied and spreads from within the HAZ to within the WM also. The prominence of compressive damage diminishes such that the tensile stress creep damage is over 10 times as per ASME and over 5 times as per RCC-MR calculations for the internal pressure of 25 MPa and k_a=1. For internal pressure of 37 MPa, creep rupture is expected to initiate from the tensile dominant region. The results show that larger damage is accumulated in the same region when an additional axial load is applied.

5.5 Chapter summary

Three case studies, each dealing with different commonly found welded components within a power plant, are undertaken and presented in this chapter. The first case study focuses on evolution of fatigue damage while the latter two focuses on creep damage analysis. The LMM subroutine was modified to accommodate welds and assess damage based on the models opted in each case study. The main observations are as follows:

1. The results demonstrate that the thermal loads have the most detrimental effect and highlights the requirement of in-depth understanding of their effect on the structural integrity of welds.

2. The presence of weld substantially influences the fatigue damage mechanism of structures under complex loading conditions. The numerical results demonstrate that they severely enhance the fatigue damage and shift the critical location to the weldment region, or introduce fatigue damage to a body otherwise experiencing elastic shake down. In extreme cases they also introduce ratchetting.

3. The presence of a large thermal gradient or thermal shock prior to creep dwell has a significant impact on its damage mechanism. This is exacerbated by the presence of a weld or any geometric variation. Hence it is recommend that in the unlikely event of a piping system experiencing a large thermal gradient due to a malfunction in the process, a detailed and thorough study be done on its effective creep resistance too. Further the critical location changes drastically due to the multiaxial stress.

4. With respect to the TF and DE creep damage models, various factor such as the start of dwell stress and total strain range should be considered before choosing them as both of their accuracy is limited to a certain range only and requires further research to widen their applicability range.

5. The inherent material heterogeneity introduces multiaxial stress at the weldment region on the application of any load with some areas experiencing tensile stress while the other areas experience compressive stress. Even for comparable creep strain accumulation, areas under experience tensile stress experience larger creep damage. This throws light on the importance of considering multiaxial and compressive stress for creep damage analysis of welds.

Chapter 6 Creep-cyclic plasticity and damage assessment of an SS304 weldolet

6.1 Introduction

The introduction of a dwell period at high operating temperature introduces creep effect on the structure. The presence of welds further complicates the structural response. Considering both the economic and safety aspects, the life assessment of welds under creep-fatigue loading is a critical issue in reactors [113]. Creep-fatigue damage evaluation has seen significant progress over the years with the development and further refining of standard codes such as ASME and R5, nevertheless, it is still observed in industries as the actual problems are far more complex than the well-controlled research environment in a lab [114]. The introduction of flexible operations within the power plants increases the susceptibility of creep-fatigue and thermo-mechanical fatigue damage at the weld.

Similar to creep-fatigue, creep-ratcheting is another dangerous and complex mechanism that occurs when inelastic strain accumulates within the structure due to either dominant creep or plasticity strains. As the inelastic strain is not compensated in a cycle, creep-ratcheting produces an open hysteresis loop at steady-state. For welds, different regions may experience different damage mechanisms and it is important to identify each of them to assess the safe life of the component.

Weldolets are used within a piping system to connect branch pipes with the header pipe. They and known to experience large stress levels under severe loading conditions [115]. With damages such as creep being reported to be found at weldolets [116]. Hence, the work presented within this chapter aims at investigating the creep-fatigue and creep-ratcheting damage of a weldolet, under a constant mechanical load and a cyclic temperature load, considering full interaction between creep and cyclic plasticity via 3D FE analysis using the eDSCA within the LMMF. The geometry of the weldolet is similar to one typically found at the steam header in a combined cycle gas turbine plant [5], [117]. SS304 is the material considered due to its extensive use in the power plant piping systems. The impact of applied load level and creep dwell on the failure mechanism and location is investigated. The effect of

two internal pressures is investigated, one is in the range of a typical operating pressure while the other is significantly higher.

Section 6.2 discusses the assessment procedure followed in this chapter. The FE model of the weldolet connection including the geometry, material properties and boundary conditions are presented in Section 6.3. Section 6.4 and Section 6.5 discusses the cyclic plasticity and the creep-cyclic plasticity interaction of the weldolet respectively. Section 6.6 presents the creep-fatigue damage calculation and Section 6.7 summarises this work.

6.2 The creep-fatigue damage assessment procedure

The general methodology followed in evaluating creep-fatigue damage of the component is illustrated in Figure 6-1. It consists of four main steps.

1. Estimation of saturated hysteresis loop using LMM.
2. Estimation of fatigue damage using E–N diagrams.
3. Estimation of creep damage using TF rule.
4. Estimation of total damage using the interaction diagram.

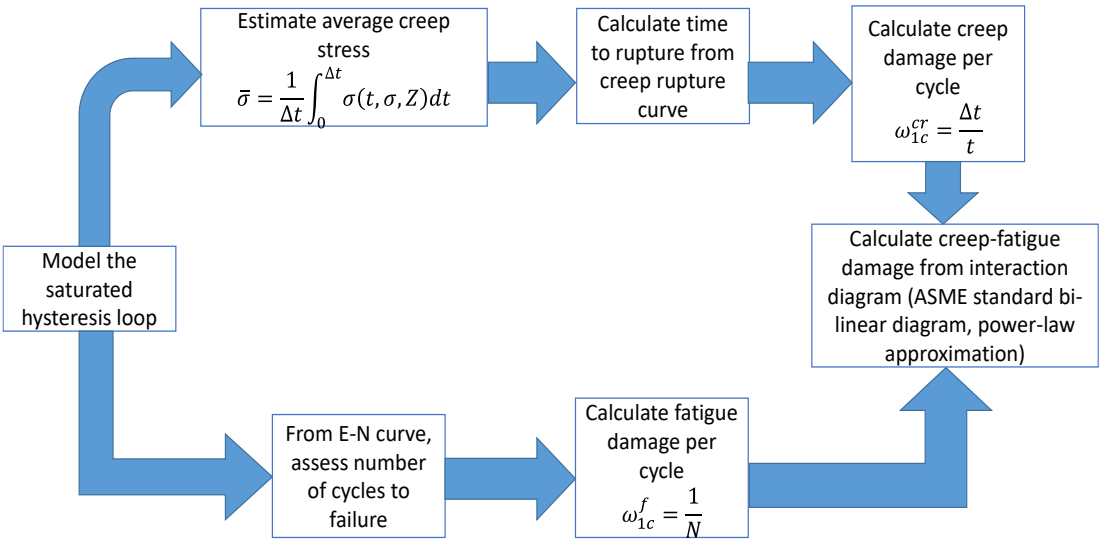

Figure 6-1 Flow-chart for the general creep-fatigue evaluation procedure [111].

Step 1: Estimation of saturated hysteresis loop using eDSCA within LMM framework

This step involves modelling the saturated hysteresis loop. The eDSCA within the LMM framework, discussed in Section 3.4, provides all the required parameters such as the effective von Mises stress at the end of all load points, the plastic strain, the total strain range, the creep strain etc. They are used in the subsequent steps for fatigue and creep damage calculations.

Step 2: Estimation of fatigue damage

The number of cycles to LCF damage is related to the total strain range. The total strain range at steady-state is obtained from the previous step. Based on the experimental data, a quadratic polynomial, cubic polynomial, or a power-law function is obtained which relates the number of cycles to failure and the total strain range. The obtained expression is used within the LMM subroutine for post-processing and obtaining the fatigue damage per cycle. Fatigue damage accumulated per cycle calculated as:

$$d_f = \frac{1}{N^{\circ}(\Delta\varepsilon_{tot})} \tag{6-1}$$

where d_f is the fatigue damage per cycle and N° is the number of cycles to crack initiation due to pure fatigue corresponding to the total strain range, $\Delta\varepsilon_{tot}$.

Step 3: Estimation of creep damage

Considering that the dwell times used for the study within this chapter is over 720 hours (1 month), it is safe to assume that the secondary creep strain will be the most prominent. Hence, Norton creep law, introduced in Section 2.3.1 is used to compute the creep strain, the uniaxial form of which is given by:

$$\dot{\varepsilon}^{cr} = A\sigma^{n} \tag{6-2}$$

where $\dot{\varepsilon}^{cr}$ is the creep strain rate, σ is the applied stress; A and n are the creep constants. In order to implement the non-isothermal effects, the creep constant A is modified using the Arrhenius law as:

$$A = A^{\star} exp\left(\frac{-Q_{act}}{R_{gas}T}\right) \tag{6-3}$$

where Q_{act} is the activation energy in kJ/mol; R_{gas} is the global gas constant $kJ\ /\ mol\ /\ K$; T is the temperature in Kelvin and $A^{\star}$ is the frequency factor. The TF rule, discussed in Section 2.4.3.1, is used for the creep-damage assessment. The time to creep rupture t^{rup} is described by the reverse power-law mentioned below:

$$t^{rup} = B^{TF}\sigma_{avg}^{-k^{TF}} \tag{6-4}$$

with B^{TF} and k^{TF} are the creep constants and σ_{avg} is the average stress over the dwell period Δt which is calculated as:

$$\sigma_{avg}(\Delta t, \sigma_1, Z) = \frac{1}{\Delta t}\int_0^{\Delta t} \sigma(\Delta t, \sigma_{cs}, Z)dt \tag{6-5}$$

where Z is the elastic follow up factor and σ_{cs} is the stress at the beginning of dwell period. Both of them are obtained from step 1. The creep damage per cycle is then defined as:

$$d_c = \frac{\Delta t}{t^{rup}(\sigma_{avg})} \tag{6-6}$$

Step 4: Creep-fatigue interaction

The next step is to calculate the total number of cycles under creep-fatigue interaction using the creep-fatigue damage interaction diagram. Creep damage per cycle, d_c and fatigue damage per cycle, d_f are calculated in the previous steps. This is used to calculate $D_c = N^{\Delta}d_c$ and $D_f = N^{\Delta}d_f$, where D_c and D_f are the creep and fatigue damage accumulated by the structure until failure and N^{Δ} is the total number of cycles under creep-fatigue interaction. As per continuum damage mechanics, it is assumed that

$$D_f + D_c \leq 1 \tag{6-7}$$

The detailed procedure, approximations, and solutions to calculate N^{Δ} is provided in [110], [118], hence, only equations relevant to this study is provided below. N^{Δ} is calculated by solving Equation (6-8)

$$aN^{\Delta 2} - bN^{\Delta} + 1 = 0 \tag{6-8}$$

where the root is

$$N^{\Delta} = \left(-b - \sqrt{b^2 - 4ac}\right)/2a \tag{6-9}$$

with

$$a = [d_c]^2 + \left[\, d_f\right]^2 + d_c \,.\, d_f \tag{6-10}$$

$$b = -2d_c - 2d_f \tag{6-11}$$

6.3 Weldolet geometry, FE model and material properties

An SS304 weldolet consisting of two weldments, as shown in Figure 6-2, is used within the study, one connects the weldolet to the main pipe while the second weldment connects the weldolet to the branch pipe. The weldolet geometry corresponds to one typically found in a steam header in a combined cycle gas turbine plant, similar to the study in [5], [117]. Due to the symmetry condition of the model, a quarter of the weldolet connection is used for the simulation. A symmetric boundary condition is applied on the x-y and y-z plane of the elbow, and plane end condition is applied on both the free ends of the pipe. Quadratic hexahedral elements of type C3D20R are used for structural analysis and quadratic hexahedral elements of type DC3D20 are used for heat transfer analysis. Both the end of the main pipe and branch pipe are constrained to expand in-plane. The total no of elements is 6, 495 with the mesh finely refined near the weldment which is the weakest area.

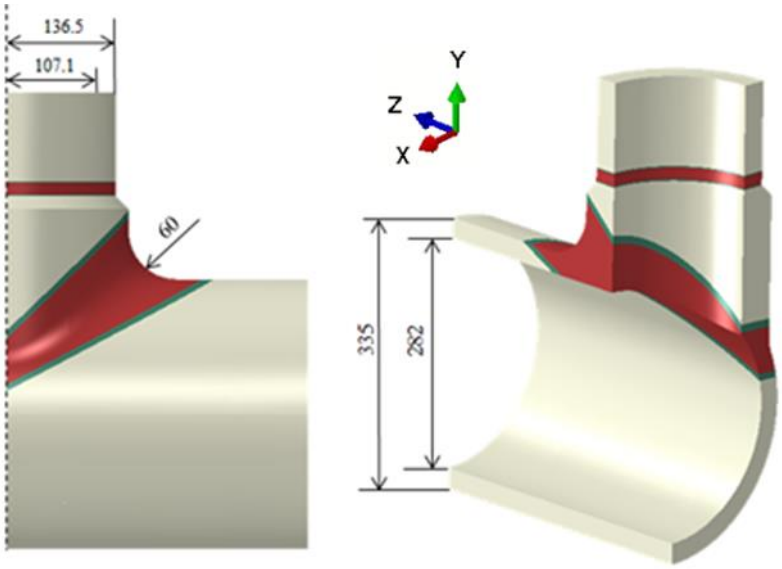

Figure 6-2 3D weldolet model with key dimensions (in mm) [5], [117].

The weldment comprises of three zones; 1) the PM, 2) the WM and 3) the HAZ. It is considered that all the three zones exhibit EPP material properties and that they satisfy the von Mises yield condition. The residual stress in the pipe due to welding is assumed zero due to the PWHT. The accuracy of the analysis greatly depends on the material properties of the three different zones considered in the weldment. It is quite challenging to obtain all of them from a single source; hence, from the available literature, a general database is generated and used for the analysis. A. Hossein *et al.* [95], [96] in their study have presented a range of mechanical properties, generated creep constitutive parameters, and temperature and stress-dependent creep properties for the SS304 PM, HAZ, and WM, which is used within this study. The EN curve for the PM at room temperature is initially generated from the NIMS database and then modified for higher temperatures and the WM. The material is considered to have a thermal conductivity of 43 $Wm^{-1}K^{-1}$ and a Poisson's ratio of 0.3. Certain reasonable modifications and assumptions are made to account for any unavailable material property. When material properties for the WM and HAZ are available only for a certain temperature, they are assumed to follow a trend similar to that of the parent material and are extrapolated/interpolated. The complete set of material properties and the EN curve used are presented in Table 6-1 to Table 6-5 and Figure 6-3 respectively.

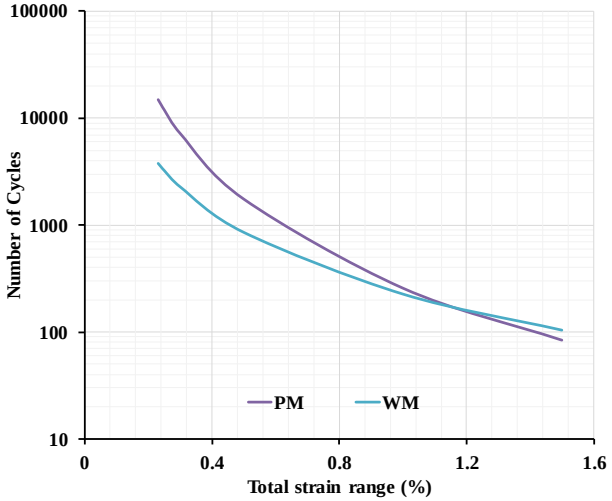

Figure 6-3 Strain-life Curve (E-N Curve) at 600 ℃.

Table 6-1 Temperature-dependent yield stress for SS304 weldolet study.

Temp ℃	25	680	700	720
$\sigma_y^{PM}\ (MPa)$	426	319	305	290
$\sigma_y^{HAZ}\ (MPa)$	151	113	108	98
$\sigma_y^{WM}\ (MPa)$	298	223	213	194

Table 6-2 Temperature-dependent Young's modulus for SS304 weldolet study.

Temp ℃	25	680	700	720
$E_y\ (MPa)$	179500	145200	116200	116000

Table 6-3 Coefficient of thermal expansion for SS304 weldolet study.

Material Zone	PM	HAZ	WM
α(x 10^{-6}℃)	1.8	1.9	2.1

Table 6-4 Norton creep strain parameters for SS304 weldolet study.

Material Zone	$A^{\star}(MPa^{-n}h^{-1})$	$Q(J/mol\,K)$	n
PM	6.0121 x 10^{-5}	2.6 x 10^5	5.72
HAZ	92.448 x 10^{-3}	2.6 x 10^5	4.76
WM	97.838 x 10^{-3}	2.6 x 10^5	4.59

Table 6-5 Creep rupture properties for SS304 weldolet study.

	B^{TF}			k^{TF}
Temp ℃	580	600	620	
PM	$5.37\times10^{+18}$	$2.31\times10^{+18}$	$1.03\times10^{+18}$	5.77
HAZ	$1.92\times10^{+15}$	$8.39\times10^{+14}$	$3.81\times10^{+14}$	4.70
WM	$1.58\times10^{+15}$	$6.91\times10^{+14}$	$3.14\times10^{+14}$	4.50

For baseline studies, an internal pressure of 17 MPa, which is in range with the typical pipe pressure in a power plant, and a cyclic thermal load with a fluctuation of 40 ℃ across the thickness of the weldolet is considered. The inner temperature is 580 ℃ and the outer temperature is 620 ℃. The effects of higher pressure and temperature are investigated by carrying out additional studies by increasing the internal pressure to 25 MPa and the thermal load by a factor of 1.2.

Linear elastic analysis is performed for the weldolet subjected to mechanical load and thermal load to understand their individual loading effects. The resultant von-Mises elastic stress contours for the mechanical load at ambient temperature, and the thermal load are illustrated in Figure 6-4. From the contours, it can be inferred that the magnitude of equivalent stress under the thermal load is slightly larger than that under the mechanical load, but well within a comparable scale. The stress concentration due to the mechanical load is enhanced by the geometric feature whereas it is the material property that influences the concentration of thermal load.

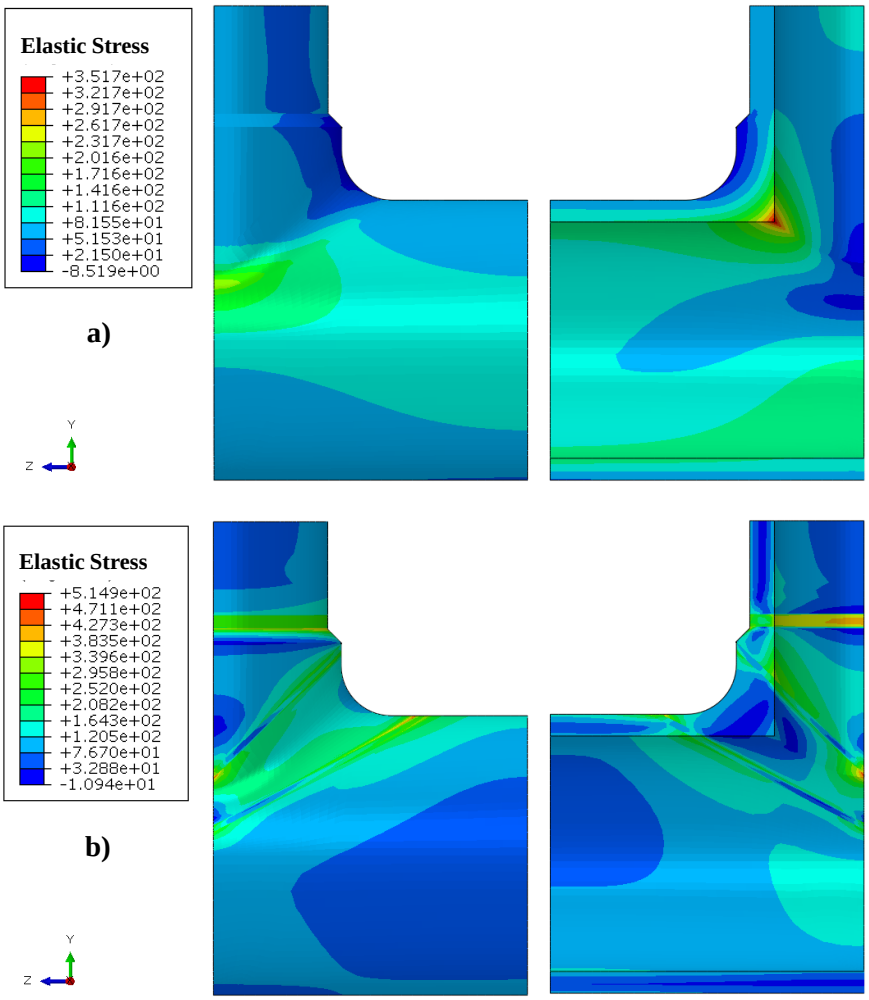

Figure 6-4 von-Mises elastic stress solutions a) mechanical load at ambient temperature; b) thermal load

6.4 Cyclic plasticity behaviour

As an initial step, before imposing a creep dwell, high-temperature fatigue analysis is carried out. Figure 6-5 presents the contours of effective total strain range and fatigue damage per cycle at steady-state (at the end of cycle). It is evident that there is substantial damage accumulation at both the weldment regions. But the most critical region is at the HAZ-WM intersection at the inner side of the pipe where the weldolet connects to the header pipe, where the strain accumulation is enhanced by the geometric irregularity.

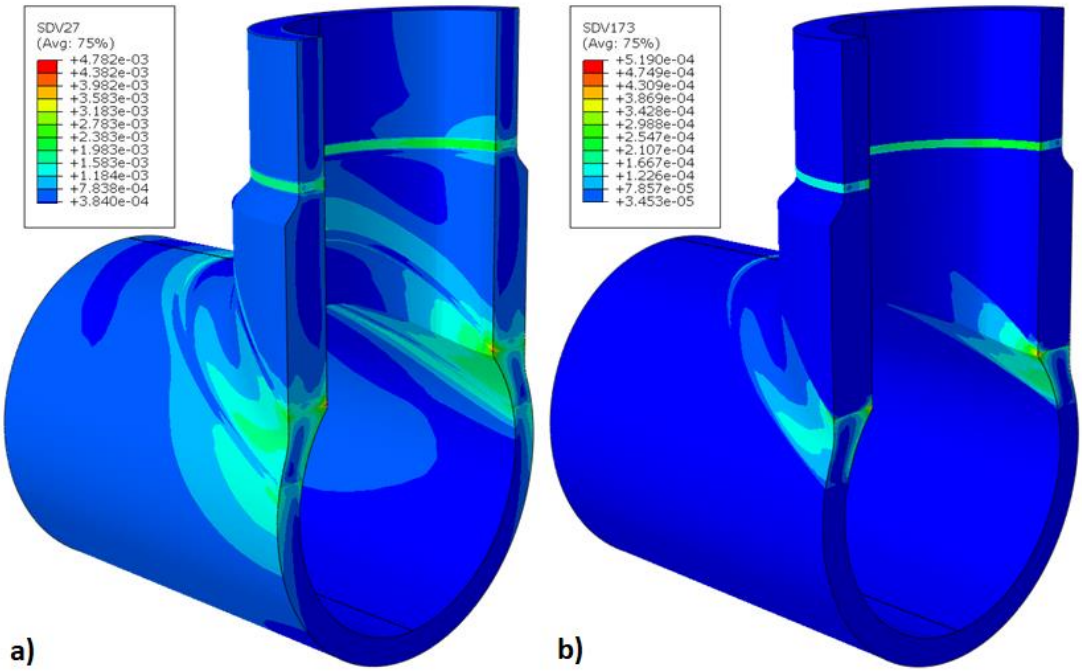

Figure 6-5 Contours for a) Effective total strain range and b) Fatigue damage per cycle.

The open hysteresis loop in Figure 6-6 indicates that the component experiences a small accumulation of plastic strain with each cycle, indicating ratcheting. The yield stress at higher temperature is considerably lower than at room temperature. This results in larger plastic strain accumulation during loading that is not compensated equally during the unloading sequence. It should be noted that the net plastic strain accumulation per cycle is very small, hence though present, ratcheting is not considered to be the major damage mechanism in this case whereas LCF damage is prominent. The cycles to LCF failure are estimated to a total of 4295 cycles. It is to be noted that as the calculation does not consider any hardening of the material, hence, the results are conservative.

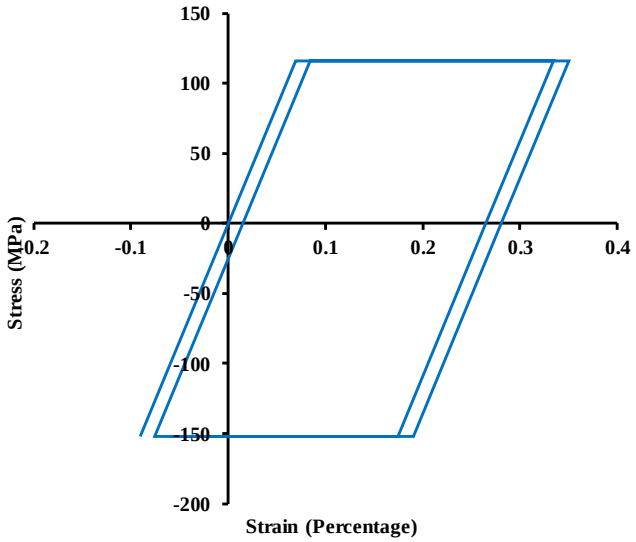

Figure 6-6 Steady-state hysteresis loop for pure fatigue case.

6.5 Creep-cyclic plasticity interaction

As introduced in Section 2.3.1 and further discussed in Section 6.2, the temperature-dependent function for the creep strain can be expressed using the Arrhenius law, $A = A^{\star} \exp\left(\frac{-Q_{act}}{R_{gas}T}\right)$. Since a thermal gradient is present across the thickness of the weldolet, the Norton law is combined with the Arrhenius law and used for the creep strain calculations. Figure 6-7 shows the isothermal thermal field applied and the creep parameter thus obtained.

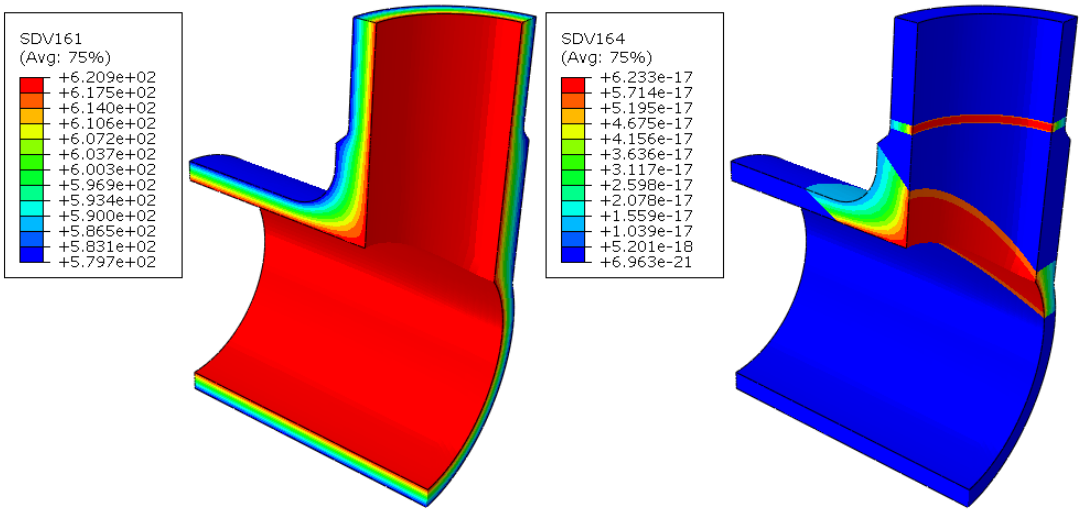

Figure 6-7 a) Thermal load applied; b) Temperature-dependent creep parameter.

The effect of dwell time on the end of creep and unloading stresses are presented in Figure 6-8. Generally, for a single material component, the stress reduces during creep dwell, but for a multi-material such as a weldment, the stress re-distribution during a creep dwell is not always straightforward. Some regions within the structure can experience stress relaxation while the other regions experience an increase in stress. For the weldolet considered here, with an increase in the dwell time, the stress near the weldment regions decreases while it increases at certain regions in the PM. The higher stress relaxation will lead to a larger strain accumulation during unloading. This will lead to larger hysteresis loops as shown in the subsequent sections.

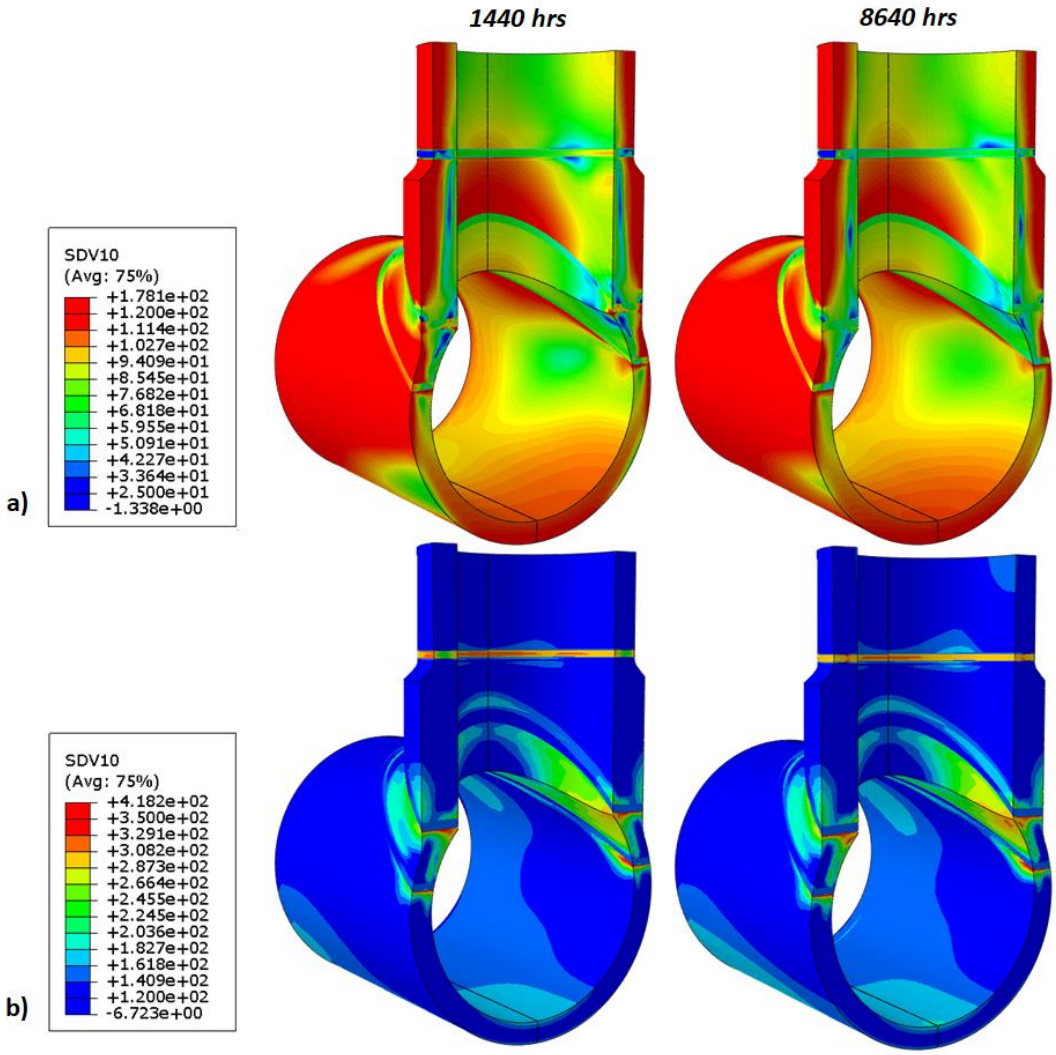

Figure 6-8 von Mises stress contours for different dwell times a) end of dwell; b) unloading.

Figure 6-9 presents the evolution of creep strain and total strain with increasing dwell time. For all the dwell times, the plastic strain accumulation during loading is very similar. With the increase in dwell time, the creep strain increases with the area of creep strain accumulation growing from the main pipe-weldolet weldment region to the inner pipe region. The branch pipe-weldolet region shows substantial creep strain accumulation only at very high dwell times. Hence, the most critical region for creep-fatigue crack initiation is at the main pipe-weldolet weldment. Unlike the plastic strain accumulation during loading, the plastic strain accumulated during unloading increases with increasing dwell time. The stress drop which happens as a result of increasing the dwell time increases the reverse plasticity. It is to be noted that the plastic strain accumulation is highly localised.

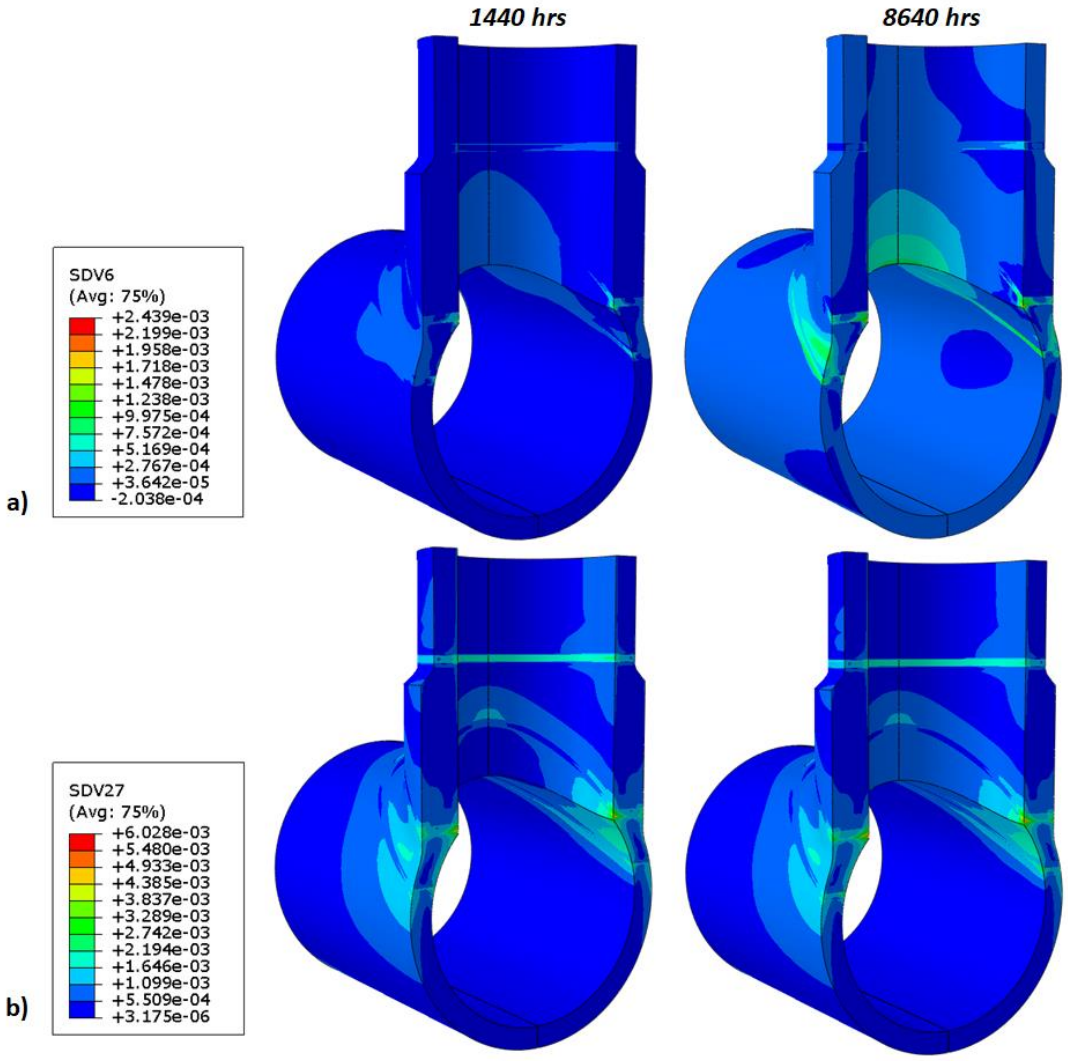

Figure 6-9 Effective strain contours for different dwell times a) creep; b) total strain range.

For further discussions, two of the most critical locations are identified, one where the total strain range is maximum; element - 583, within the HAZ, hereafter referred to as element T, and the other where the creep strain is maximum; element 4931, within the WM hereafter referred to as element C. For all the dwell times considered, the maximum creep strain is within the same element. It is interesting to note that this element is different from the elements that showed maximum stress concentration during the initial elastic stress analysis. The reasons for this can be better explained and discussed with the help of a hysteresis loop. Figure 6-10 shows the effect of various creep dwells for element T. The two most obvious effect of creep dwell on the component that can be visually inferred are that it enhances the reversed plasticity through the stress relaxation resulting in a larger hysteresis loop and the introduction of creep-ratcheting phenomena.

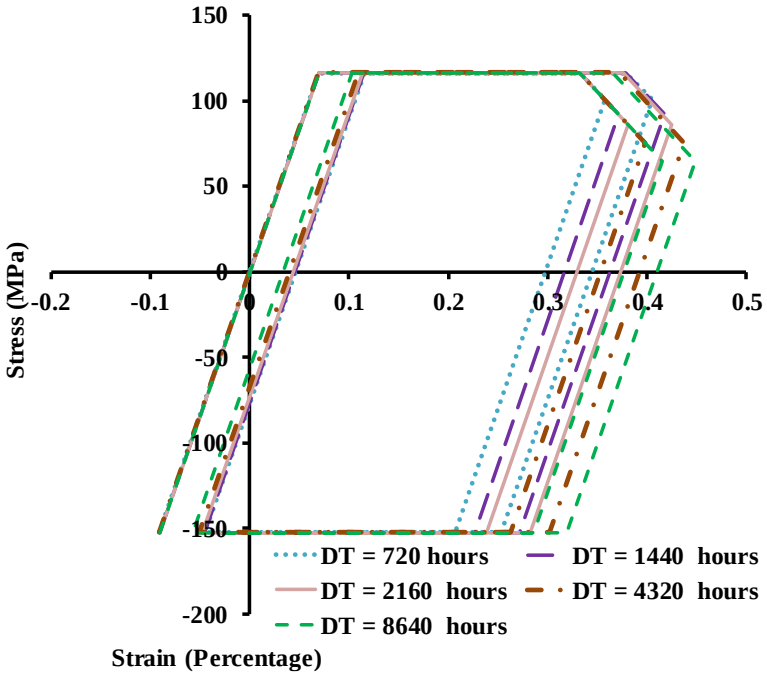

Figure 6-10 Steady-state hysteresis loop for increasing dwell times for element - T.

To have a deeper understanding on the effect of dwell time on the creep-cyclic plasticity response of the weldolet, a plot comparing the magnitude of the loading, unloading and creep strains are presented in Figure 6-11 (a). It can be seen that the plastic strain magnitude during loading is nearly constant, whereas the plastic strain magnitude during unloading increases gradually with increasing dwell times with the cross over at around dwell times of 1000 hours. The creep strain on the other hand increases in proportion to the increase in the reverse plasticity. The most significant changes occur up to a dwell time of 2000 hours after which the

increase is almost linear. Nevertheless, the net plastic strain is always higher than the creep strain resulting in the creep-ratcheting mechanism. Figure 6-11 (b) depicts a comparison between the accumulated creep strain and net plastic strain that can be used to understand the driving factor of the creep-ratcheting process. The 45° red line indicates a closed hysteresis loop, which occurs when the net plastic strain compensates the creep strain. For lower dwell holds, the points analysed are below the closed-loop limit whereas for larger dwell times the points are above the closed limit. This indicates creep-ratcheting is driven by reverse plasticity in the former case and cyclically enhanced creep in the latter case. The above discussions highlight the effects of creep dwell time on both the shape of the hysteresis loop and the creep-cyclic plasticity response of the weldolet. Unlike with the pure fatigue case, the accumulated net plastic strain is quite substantial here such that it cannot be neglected. Hence it is required that checks be performed to ascertain the creep-ratcheting damage and compare them with the creep-fatigue damage of the weldolet.

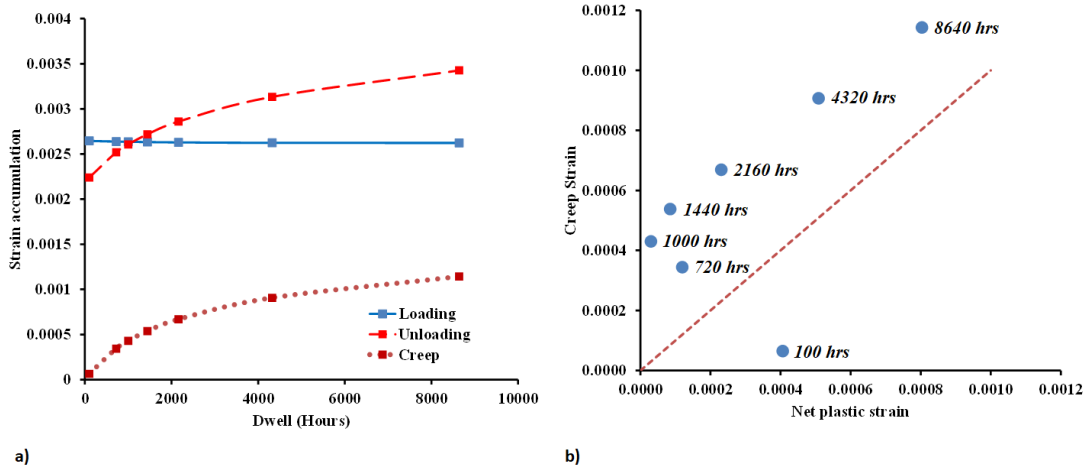

Figure 6-11 For element - T a) Plot comparing the magnitude of loading, unloading and creep strains; b) Creep-ratcheting interaction diagram for different dwell times.

Figure 6-12 presents the steady-state hysteresis loop for C. Compared to T, where an open hysterics loop is observed in the absence of creep dwell, C exhibits elastic behaviour. This is because element C is within the WM wherein the yield stress is higher than that of the HAZ and the overall stress level during loading is below the yield.

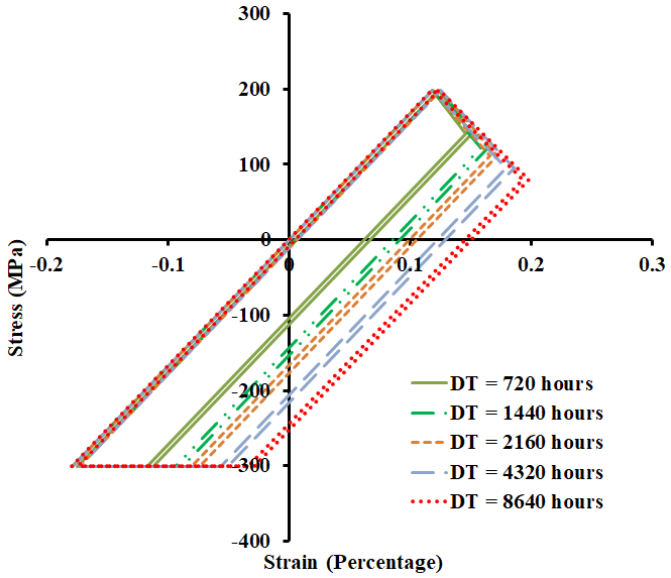

Figure 6-12 Steady-state hysteresis loop for increasing dwell times for element - C.

On introducing a creep dwell, the creep strain accumulates and the subsequent stress relaxation enhances the plastic behaviour during unloading. In effect, the introduction of a creep dwell induces both LCF damage as seen from the width of the hysteresis loop and creep damage as seen from the stress relaxation within this region. The plot comparing the magnitude of the unloading and creep strains for element-C are presented in Figure 6-13 (a). There is an exponential rise in the strain accumulation for dwell times up to 2000 hours, after which the increase follows a linear trend. Figure 6-13 (b) presents the comparison of the creep strain and net plastic strain. All the points considered lie on or are very close to the closed-loop limit.

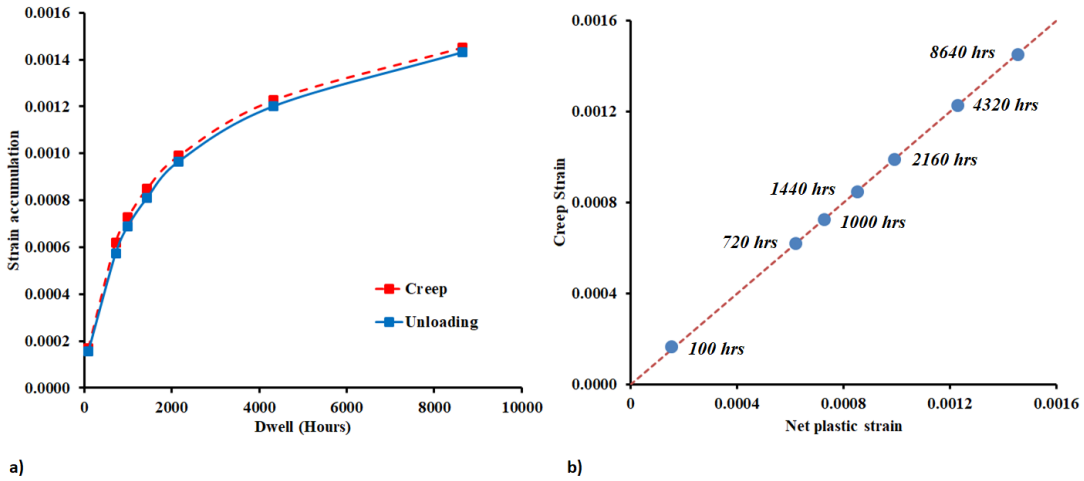

Figure 6-13 For element - C a) Plot comparing the magnitude of loading, unloading, and creep strains; b) Creep-ratcheting interaction diagram for different dwell times.

6.6 Creep-fatigue and creep-ratcheting damage calculations

In a single material structure, it is safe to assume that crack initiation will begin from T. But, as the component considered here is a weldment where the welding process has altered the creep and fatigue tolerance at the different zones, damage studies are required to assess the crack initiation region. Figure 6-14 presents the comparison between the hysteresis loop for element T and C for dwell times of 1440 hours. For element C, both the start and end of dwell stress are substantially larger than element T, this leads to higher average creep stress which will lead to a higher creep damage. On the other hand, as the width of the hysteresis loop of element T is much larger than that of element C, fatigue damage is more prominent within this region.

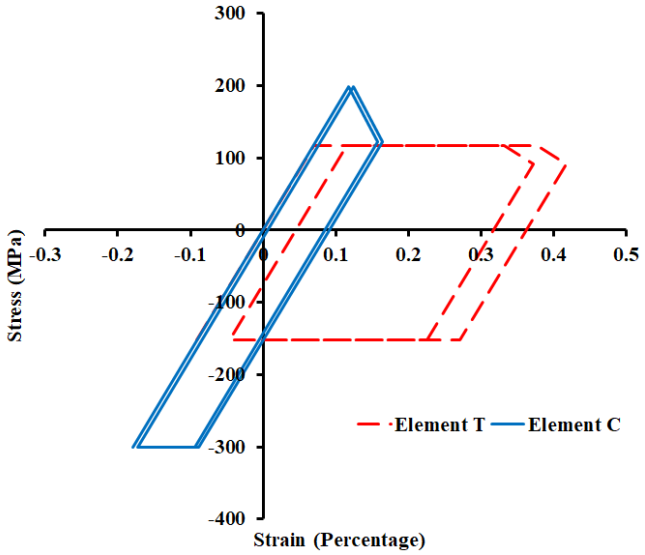

Figure 6-14 Hysteresis loop comparison for element T and C for dwell times of 1440 hours.

From the hysteresis loop in Figure 6-10 and the creep strain-net plastic strain comparison presented in Figure 6-11, it is clear that element T is subjected to creep-ratcheting. Hence before comparing the creep-fatigue cycles to failure at element T and element C, it is necessary to analyse whether creep-ratcheting or creep-fatigue damage is more prominent at element T. Kapoor A, in [119] suggested the below formula for the evaluation of the safe life of components subjected to ratcheting

$$N_r = \frac{\varepsilon_{cr}}{\Delta\varepsilon_r} \tag{6-12}$$

where N_r is the number of cycles to failure by ratcheting, $\Delta\varepsilon_r$ is the ratcheting strain per cycle and ε_{cr} is the accumulated strain at which the component is considered to fail.

Figure 6-15 presents the comparison between the creep-fatigue life and creep-ratcheting life for dwell times up to 8640 hours. For lower dwell times, the number of cycles to failure due to creep-fatigue is much larger than cycles to failure due to creep-ratcheting. On increasing the dwell time, creep-fatigue damage becomes more significant owing to the high creep damage. It is interesting to note that the creep-ratcheting damage is independent of dwell time. This is because the reverse plasticity is able to compensate for most of the inelastic strain but for a small plastic strain produced during loading which remains constant. Hence, it can be concluded that for dwell times over 720 hours creep-fatigue is the prominent damage mechanism at element T.

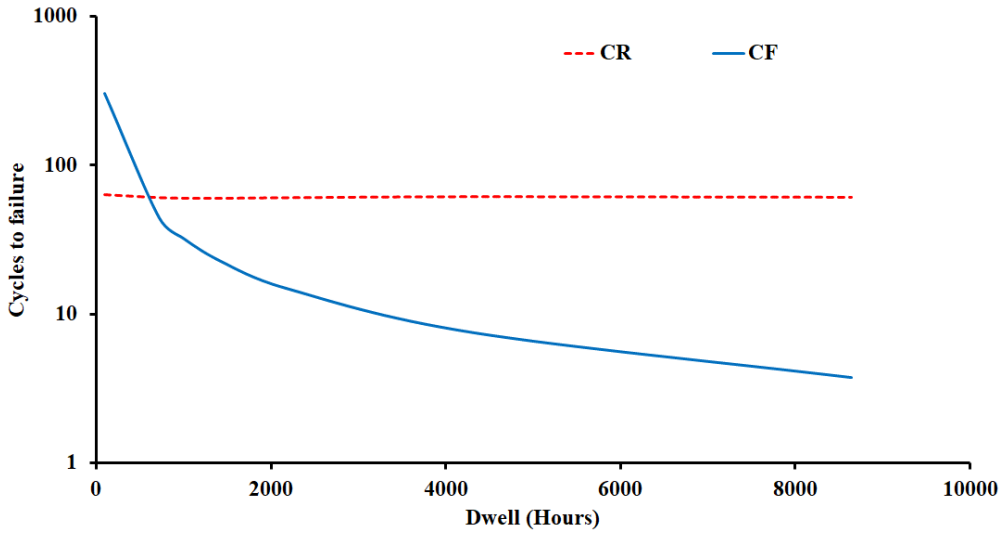

Figure 6-15 Comparison between creep-fatigue and creep-ratcheting life against dwell time.

Figure 6-16 reflects the number of cycles to failure and change in damage with increasing dwell times for both the elements. On increasing the dwell time, the cycle to failure decreases, with the decrease in the number of cycles being more prominent in element-C. For element T, though with the increase in dwell time, there is an accumulation of damage, it is not as steep as with element-C.

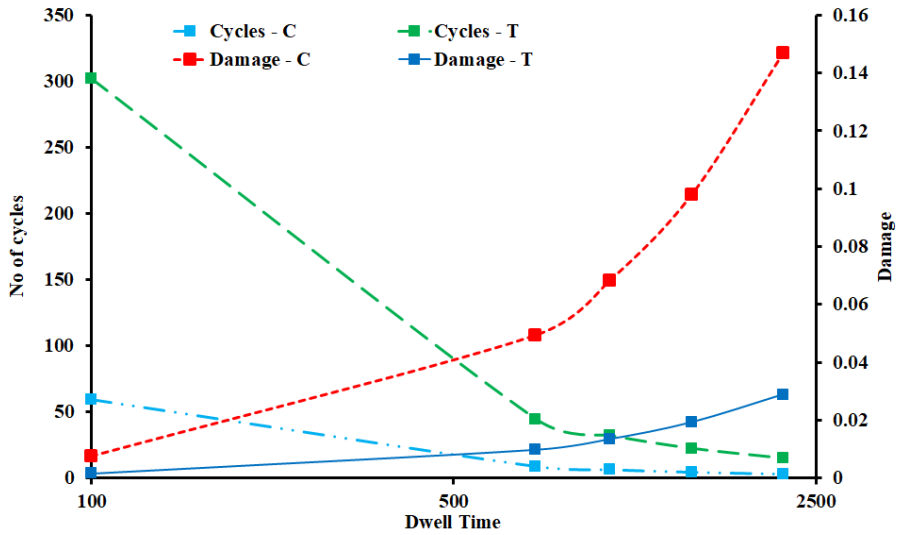

Figure 6-16 Total damage and cycle to failure against dwell times.

Figure 6-17 shows the variation of fatigue damage per cycle and creep damage per cycle with increasing dwell times. Both creep damage and fatigue damage increase with an increase in dwell time. But it evident that the total damage is driven by creep. The fatigue damage at element T is higher than element C for all dwell times considered while creep damage is much higher at element C compared to element T, this can be attributed to the higher average creep stress at element C coupled with the high damage constants in Equation (6-4) for the WM.

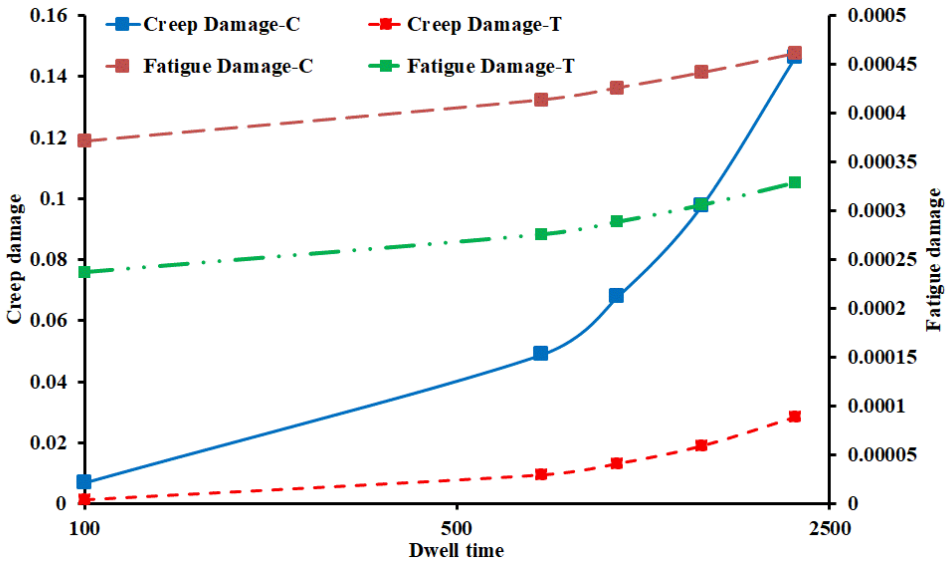

Figure 6-17 Creep and fatigue damage per cycle against dwell times.

The effect of a larger mechanical load is investigated for internal pressure of 25 MPa. Figure 6-18 presents a comparison between the hysteresis loops for both the elements T and C at a dwell time of 2160 hours. For element C, the hysteresis loop is similar indicating that the additional mechanical load has no effect whereas, for element T, a reduction in the ratchet strain accumulation is observed. This results from the lesser accumulation of plastic strain during loading, nevertheless, this is very minimal and is not expected to have any significant difference in the creep-fatigue damage life.

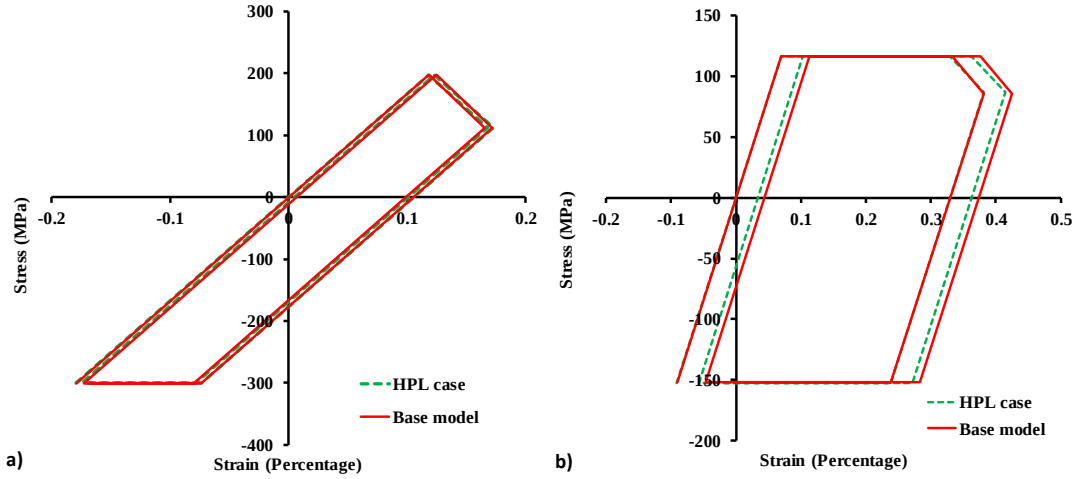

Figure 6-18 Steady-state hysteresis loop for High-Pressure Load (HPL) of 25 MPa and base model for DT of 2160 hours at a) element C; b) element T.

However, the increase in the mechanical load leads to very large ratchet strain accumulation towards the outer side of the weldolet at the HAZ-PM interface with the main pipe, Figure 6-19 (a). Figure 6-19 (b) provides a comparison between the creep-fatigue life at element C and creep-ratchet life at the element identified with maximum ratchet strain accumulation per cycle.

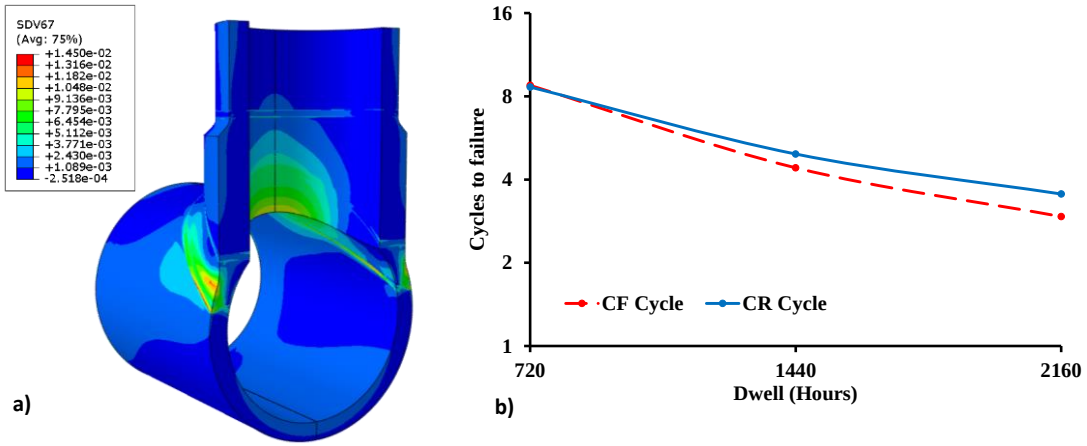

Figure 6-19 For larger internal pressure of 25 MPa a) Contour for effective creep-ratchet strain per cycle; b) Comparison between creep-fatigue and creep-ratcheting life against dwell time.

The number of cycles to creep-ratchet damage is very close to that to creep-fatigue damage such that the damage may initiate due to any of the mechanisms. Figure 6-20 presents the hysteresis loop for the element with maximum ratcheting strain. It can be observed that during creep dwell, no stress relaxation takes place within this element though large creep strain accumulation is quite observed.

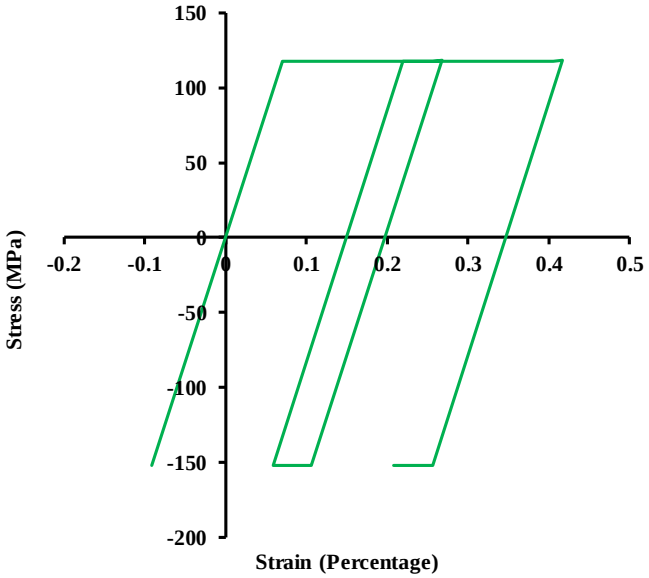

Figure 6-20 Steady-state hysteresis loop for HPL at the element with maximum ratcheting strain.

The effect of a thermal load is investigated by imposing an inner temperature of 740 ℃, 1.2 times the initial thermal load. The analysis is restricted to a maximum dwell time of 100 hours as above this the damage is similar to that of monotonic creep rupture. Figure 6-21 presents the comparison of the hysteresis loop for elements T and C for a creep dwell of 100 hours for the baseline temperature and the High-Temperature Load (HTL).

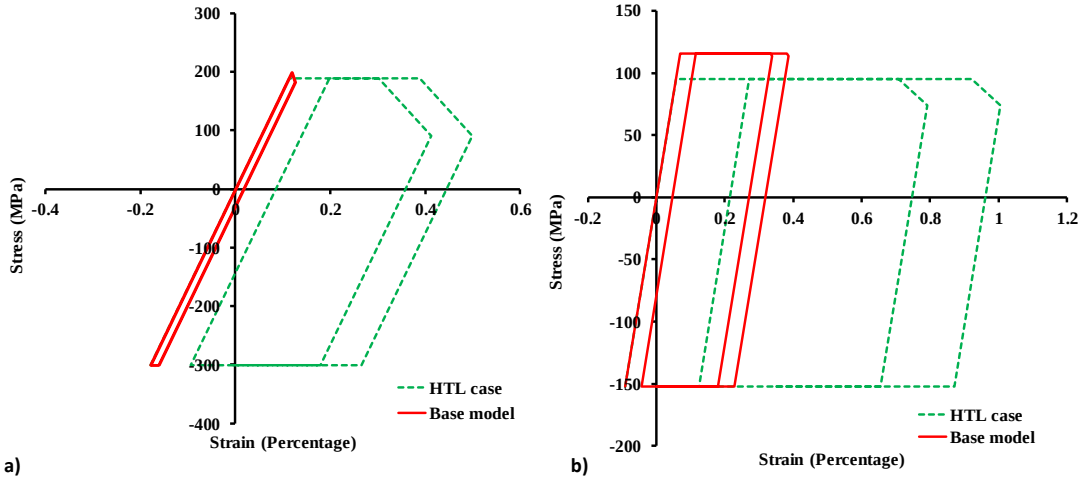

Figure 6-21 Steady-state hysteresis loop for HTL of 740 ℃ and base model for DT of 100 hours at a) element C; b) element T.

The plastic strain during loading is drastically enhanced by the increase in temperature. Element C which was otherwise exhibiting a closed-loop now has an open loop. One of the reasons for this is that as temperature-dependent material properties are used yielding starts at a much lower stress level. The creep strain also increases significantly for both the elements suggesting a more prominent creep-ratcheting mechanism.

6.7 Chapter summary

Creep-cyclic plasticity interaction and life assessment of an SS304 weldolet subjected to a combined mechanical and thermal load is investigated. The structure is modelled using a quarter 3D model and temperature-dependent material properties are used for the analysis to replicate a more realistic creep-cyclic plasticity behaviour and lifetime prediction. The main observations include:

1. The introduction of a creep dwell increase the total strain range. This is due to the creep strain resulting from the creep relaxation and the subsequent increase in the plastic strain during unloading. In effect this lead to creep-fatigue interaction.

2. Due to the different creep-cyclic plasticity behaviour of the PM, WM and HAZ. The creep-fatigue interaction results in creep-fatigue damage within the WM, and both creep-fatigue and creep-ratcheting damages within the PM. However due to the large creep parameters of the WM coupled with higher average creep stress, the creep damage within the WM is large, and the subsequent creep-fatigue interaction is expected to drive the crack initiation process. Hence, while conducting creep-fatigue damage analysis for weldments, due consideration should be given to all the different zones.

3. All the key parameters such as the mechanical load, the thermal load and dwell period are confirmed to have a significant effect on the creep-fatigue interaction. For shorter dwell time the creep-ratcheting within the PM is driven by reverse plasticity. Conversely, for larger dwell times creep-ratcheting is due to cyclically enhanced creep. The larger mechanical load results in large plastic strain accumulation during loading, driving the component towards creep-ratcheting mechanism initiating from the outer side of the weldolet at the PM-HAZ interface. While the larger thermal load indicated that the component experience creep-rupture for dwell holds above 100 hours.

Chapter 7 Effect of welding residual stress on creep-cyclic plasticity behaviour

7.1 Introduction

Residual stress is an inevitable by-product of almost all manufacturing or fabrication process [120]. The non-uniform rapid heating and subsequent cooling of joints during the welding process results in inhomogeneous mechanical characteristics and the formation of welding residual stress (WRS) [121]. In many of the cases reported, the residual stress at the weldments tends to reduce the safe life under cyclic loading conditions, especially if steps are not taken to reduce the residual stress [122]. The presence of a pre-stress or pre-strain on components are known to affect its fatigue damage due to the variation it causes in the mean stress (in case of HCF) or mean strain (in case of LCF). The WRS will have a similar effect on the LCF, as even if it relaxes during the PWHT, they will influence the mean strain. The effect of WRS on structural integrity is not straightforward to assess, many factors such as the magnitude, direction and the material property are to be considered.

LMM's capacity to accurately access the shakedown-ratcheting interaction curve has been widely recognized with the limit load and shakedown plugin incorporated into the R5. The LMM eDSCA can effectively evaluate the creep-cyclic plasticity behaviour at steady-state and when they are coupled with appropriate rule-based codes can predict the safe life of components. However, none of the LMM subroutines considers the effect of any additional residual stress such as the WRS. It has been identified that the WRS does have an effect on the overall life of the component. Hence, the LMM subroutine is modified to account for any additional WRS effect. It should be noted that the LMM cannot assess the structural behaviour during the initial cycles, hence step-by-step inelastic analysis is carried out to account for the WRS and the stress evolution during the initial cycles which are then used within LMM.

The work presented within this chapter aims at investigating the effect of WRS on the cyclic plasticity and creep-cyclic plasticity response of a welded flange. The finite element model of the welded flange, material properties and applied boundary conditions are presented in Section 7.2. The heat source modelling and residual stress calculation procedures are discussed

in Section 7.3. Investigation of the effects of WRS on the shakedown-ratcheting curve using the LMM is discussed in Section 7.4. Section 7.5 to Section 7.7 deals with the effect of WRS on transient and steady-state damage accumulation. Section 7.8 presents the summary of this chapter.

7.2 FE model and material properties

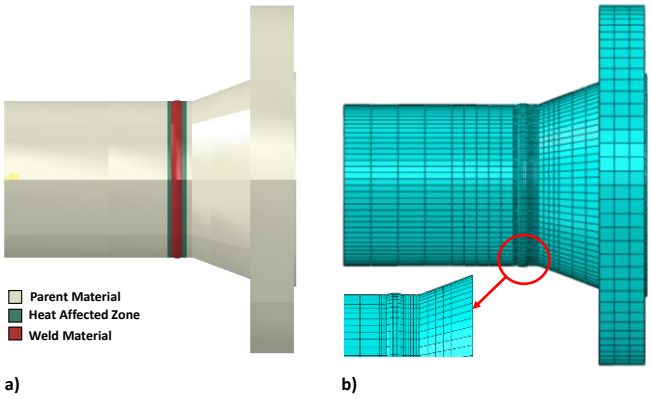

Figure 7-1 Flange-pipe weld a) Key material zones; b) Mesh used for FEA.

The case study undertaken in this chapter considers a P91 flange of rating #300 that is welded to a 4-inch pipe. The weldment consists of three material zones; a) the PM; b) the HAZ; and c) the WM as shown in Figure 7-1 (a). The study requires the simulation of a moving heat source to generate the WRS, hence, a 3D model is opted over a 2-D or an axisymmetric model for use in FE simulation. The software used within the study for FE simulation is Abaqus. The mesh used comprises of 10,640 elements. The critical area is identified to be within the region that includes the weldment and the geometrical change due to the flange head, hence, the mesh is finely refined in these areas as shown in Figure 7-1 (b).

To assess the WRS, a heat transfer analysis is carried out initially to determine the temperature history at all the nodes. This includes the temperature variation due to the moving heat source, followed by cooling to room temperature and the subsequent heat treatment (annealing). The temperature history is then used as an input for the static analysis to calculate the final WRS. DC3D20, quadratic hexahedral elements are used for the heat transfer analysis, and C3D20R, quadratic hexahedral elements are used for structural analysis. As the analysis involves two steps where the results from the initial analysis, estimation of WRS, are used as an input within the LMM framework, the boundary conditions and constraints adopted are such that the same

can be used in both the steps. A symmetric boundary condition about x-direction is applied at the flange head. Towards the pipe end, a plane constraint is implemented so that the pipe may expand radially or axially but the face remains in-plane. Further, the flange is modelled without any bolt holes, it is assumed that this geometrical simplification has minimal effect on the creep-cyclic plasticity response of the weldment.

An EPP model is considered to assess the plasticity behaviour of the structure. For normal operations, the structure is subjected to a constant internal pressure of 2 MPa, a cyclic thermal load of 600 ℃ and a dwell period of 4320 hours. The bulk of material and creep parameters for are obtained from the NIMS database [123] and [124]. The HAZ is assumed to be softer than the PM while the WM is considered to be harder than the PM and the variation of their properties with temperature is similar to that of the PM. The material properties and creep constants used are given in Table 7-1 to Table 7-4. The thermal conductivity and specific heat are assumed to be the same for all the three regions. The coefficients of thermal expansion for the different zones are as indicated in Table 7-4. A slight mismatch is introduced in the coefficient of thermal expansion for WM and HAZ to introduce a stress concentration at the weldment region. The Norton creep constants, *A* and *n*, adapted are such that a higher creep strain is introduced in the structure and an effective study on the creep-cyclic plasticity is possible.

Table 7-1 Temperature-dependent yield stress for WRS study.

Temp ℃	0	100	200	300	400	500	600	800	1000	1250
PM (MPa)	503	478	453	444	424	379	273	60	15	0.001
HAZ (MPa)	473	450	426	418	399	357	257	56	14	0.001
WM (MPa)	554	526	499	489	467	417	301	66	17	0.001

Table 7-2 Temperature-dependent Young's Modulus for WRS study.

Temp ℃	0	100	200	300	400	500	600	800	1000	1200
PM (GPa)	212	207	202	194	185	176	164	133	97	48
HAZ (GPa)	201	196	190	183	175	166	155	126	92	46
WM (GPa)	162	158	154	148	141	134	125	101	74	37

Table 7-3 Norton creep strain parameters for WRS study.

Temp℃	550	600	650	700	750	n
	$A(MPa^{-n}h^{-1})$					
PM	2.1×10^{-22}	1.7×10^{-21}	1.09×10^{-20}	5.8×10^{-20}	2.62×10^{-19}	8.462
HAZ	4.43×10^{-22}	3.57×10^{-21}	2.3×10^{-20}	1.22×10^{-19}	5.52×10^{-19}	8.462
WM	2.64×10^{-22}	2.13×10^{-21}	1.37×10^{-20}	7.28×10^{-20}	3.29×10^{-19}	7.65

Table 7-4 Coefficient of thermal expansion for WRS study.

Temp ℃	0	100	600	1200
PM ($℃^{-1}$)	9.77×10^{-6}	1.02×10^{-5}	1.28×10^{-5}	1.32×10^{-5}
HAZ ($℃^{-1}$)	1.22×10^{-5}	1.28×10^{-5}	1.6×10^{-5}	1.65×10^{-5}
WM ($℃^{-1}$)	1.1×10^{-5}	1.15×10^{-5}	1.44×10^{-5}	1.49×10^{-5}

7.3 Heat source modelling and calculation of WRS

The fundamental principle by which residual stress builds in a weldment is quite straightforward. However, accurately modelling the same is not easy, as it requires numerous time-dependent and independent material properties. They are not always readily available and so approximations should be made. The two main assumptions/approximations considered for this study include:

1. Use of sequentially coupled procedure for calculating the WRS: The residual stress within the weldment is introduced by first modelling a heat source and moving it along the circumference of the pipe. It is then used as an input for the static analysis which calculates the WRS. This sequentially coupled procedure is opted over a fully coupled procedure as it is assumed that the stress solution is dependent on the temperature field but the inverse does not hold.

2. The effect of phase transformation on material properties is disregarded: Various researchers have presented results both with the consideration of phase transformation [125]–[127] and without the consideration of phase transformation [128]. During cooling of the welding process, P91 generally experiences martensitic transformation which affect the residual stress. Yaghi, A. *et al.* [127] have compared the WRS with

and without the effect of phase transformation considerations for a P91 weld and have concluded that the phase transformation does have a moderate effect on the WRS.

For studies comparing the numerical results with experimental results, the above two assumption will limit the extend of a good agreement. Nevertheless, within this study the intend is not to compare the numerical results with experimental results but to discuss the effect of WRS on the shakedown-ratchet interaction curves and the creep-fatigue damage interaction. Hence this two assumptions/approximations are considered to be acceptable. Further with these assumptions/approximations the computational expense and time is also restricted.

A double ellipsoidal heat source model is used, Figure 7-2, which is similar to the model presented in [129], [130] within the analysis. The model uses two ellipsoidal sources to simulate the experimental effect, with a steep temperature gradient in the front and a slightly less steep temperature gradient at the rear.

The power density distribution of the model is given by:

$$q_f(x,y,z,t) = \frac{6\sqrt{3}f_f Q}{abc_f\pi\sqrt{\pi}} exp\left\{-3\left(\frac{x^2}{a^2}+\frac{y^2}{b^2}+\frac{(z+vt)^2}{c_f^2}\right)\right\} \quad (7\text{-}1)$$

for the front quadrant and

$$q_f(x,y,z,t) = \frac{6\sqrt{3}f_r Q}{abc_r\pi\sqrt{\pi}} exp\left\{-3\left(\frac{x^2}{a^2}+\frac{y^2}{b^2}+\frac{(z+vt)^2}{c_r^2}\right)\right\} \quad (7\text{-}2)$$

for the rear quadrant, where x, y and z are the local spatial coordinates, $Q=\eta VI$ is the input power of the welding heat source. A user subroutine in DFLUX is developed to apply the volumetric heat flux due to welding.

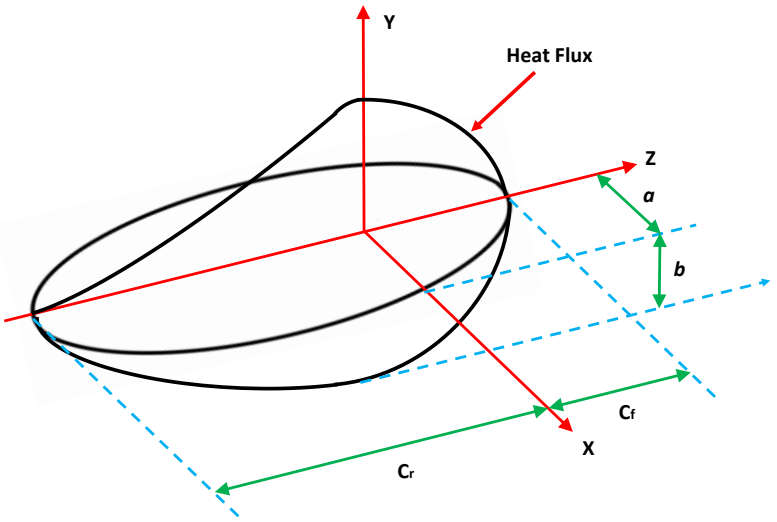

Figure 7-2 Double ellipsoidal heat source configuration [130].

Table 7-5 Numerical values for heat source parameters and welding parameters [130].

a_f (mm)	a_r (mm)	b (mm)	c (mm)	f_f (mm)	f_r (mm)
12.9	10.3	6	5	1.4	0.6

V (volts)	I (amp)	η (%)
22	225	85

For the heat flow simulation, the welding speed, *v*, is considered to be 6.25 mm/s. The flange has an outer diameter of 114.3 mm, it takes 58.7 s for the torch to complete one revolution. Once the moving heat source is simulated, the flange is allowed to cool down to the ambient temperature after which it is annealed to a temperature of 760 °C for 2 hours, during which the stress redistributes as per the Norton creep law, and then subsequently cooled down to room temperature. The thermal history obtained is used within a static analysis to compute the final residual stress. Figure 7-3 presents the as-weld residual stress and the PWHT residual stress. The PWHT almost completely relaxes the residual stress away from the weldment and reduces its magnitude within the weldment. As a larger difference in coefficient of thermal expansion among the three zones are used, the WRS after the complete procedure (when room temperature is obtained) is higher than the ones reported experimentally. However, this stress relaxes as soon as the structure is put into service at high temperature.

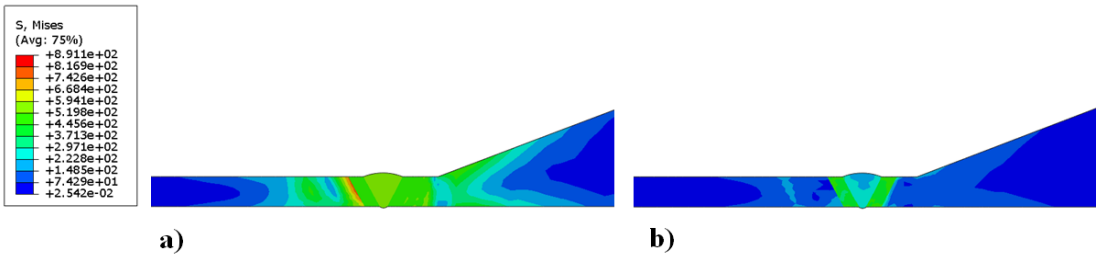

Figure 7-3 Welding residual stress a) As-weld; b) after PWHT.

7.4 Effect of WRS on shakedown and ratchet limit curves

Most of the shakedown limit studies undertaken consider the residual stress associated with the initial plastic deformation, little or no research is done considering the WRS [131], similar is the case with the studies regarding ratchet limit. Within this sub-section, the influence of the WRS on the shakedown and ratchet limit is investigated by modifying the LMM subroutine to account for the additional residual stress. Figure 7-4 presents the comparison between the shakedown and ratchet limit curve with and without WRS.

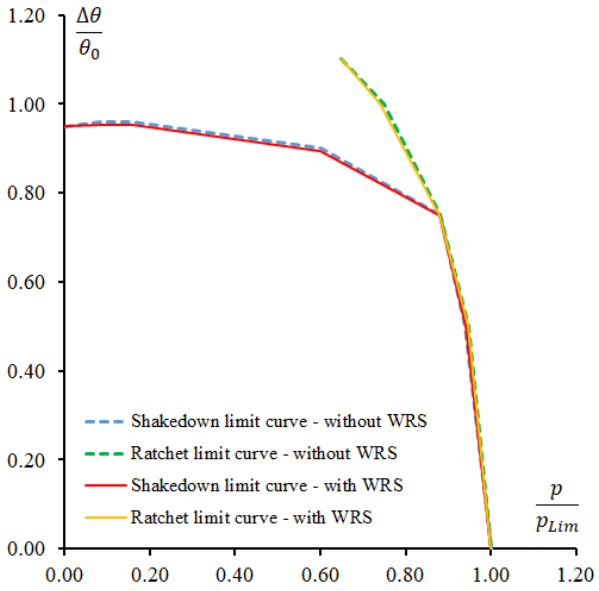

Figure 7-4 Influence of WRS on shakedown-ratchet interaction curve.

It can be observed that with and without WRS, the structure traces a similar shakedown and ratchet interaction curve. This is because the residual stress within the body redistributes itself to accommodate the additional WRS. Recalling Equation (3-2) from Chapter 3, the general

form of the elastic solution for cyclic loading cases contains the constant residual stress component, $\overline{\rho_{ij}}$ and the varying residual stress component, $\rho_{ij}^{r}(x_i,t)$. In the presence of WRS, $\overline{\rho_{ij}}$ modifies to $\overline{\rho_{ij}'}$ such that $\overline{\rho_{ij}'} + \rho_R = \overline{\rho_{ij}}$ in order to contain the structure within the shakedown or ratchet limit.

$$\sigma_{ij}(x_i,t) = \lambda\widehat{\sigma_{ij}}(x_i,t) + \overline{\rho_{ij}} + \rho_{ij}^{r}(x_i,t) \tag{7-3}$$

$$\sigma_{ij}(x_i,t) = \lambda\widehat{\sigma_{ij}}(x_i,t) + \overline{\rho_{ij}'} + \rho_R + \rho_{ij}^{r}(x_i,t) \tag{7-4}$$

Figure 7-5 presents the evolution of the internal residual stress with and without the WRS. In line with the equations presented above, the internal residual stress field is considerably changed in the presence of the WRS.

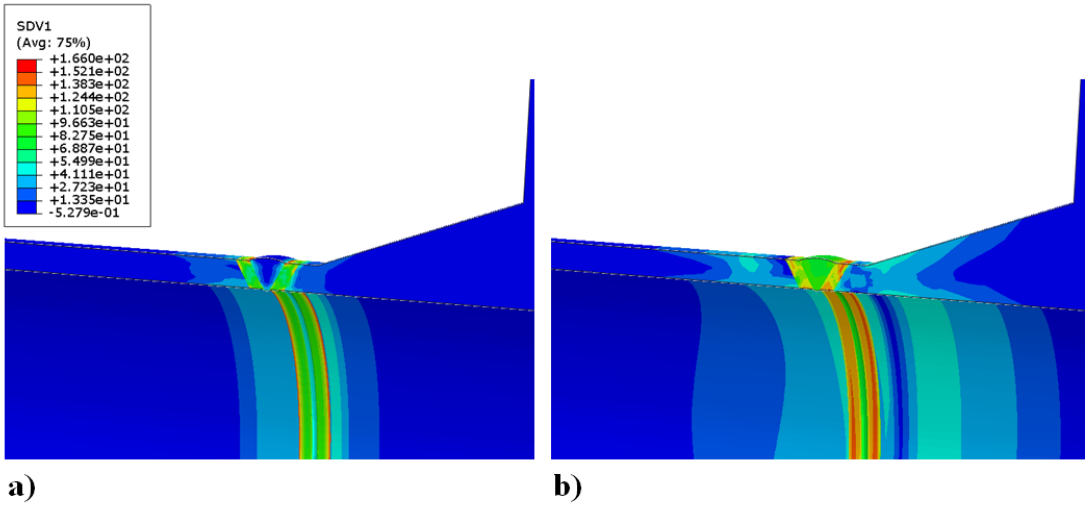

Figure 7-5 Internal residual von Mises stress a) without WRS; b) with WRS.

However, it should be noted that though shakedown and ratchet limits are not influenced by the presence of the WRS, its presence causes a difference in the relaxation and redistribution of the stresses. Hence, it will affect the damage mechanisms of the structure.

7.5 Effect of WRS on transient cycles

Within the first few cycles, if the structure experiences plasticity, the WRS tends to re-distribute within the structure. Hence, to study the effect of WRS, a comprehensive understanding of the evolution of stress and strain during the initial cycles is required. The LMM is only capable of assessing the cyclic response of the structure at steady-state, hence inelastic step-by-step analysis is used to study the effect of WRS during the transient/initial cycles. Figure 7-6 presents the contours for the plastic strain accumulated during the initial cycle with and without WRS. In the absence of WRS, substantial plastic strain is observed during both loading and unloading, whereas with the WRS, the plastic strain during loading is completely nullified, and the region and magnitude of the plastic strain during unloading becomes smaller. Figure 7-7 presents the contours of creep strain at the end of the first dwell with and without WRS. It is quite evident that the creep strain within the WM is considerably increased in the presence of WRS. This is because of the higher start of dwell stress within the WM. The reduction in the overall plastic strain and creep strain in the HAZ region is because the WRS and the resultant stress due to the applied loads are opposite in direction. The WRS is mostly tensile within the HAZ while the applied load results in compressive stress. This reiterates the importance of assessing the effect of WRS on the life of the structure.

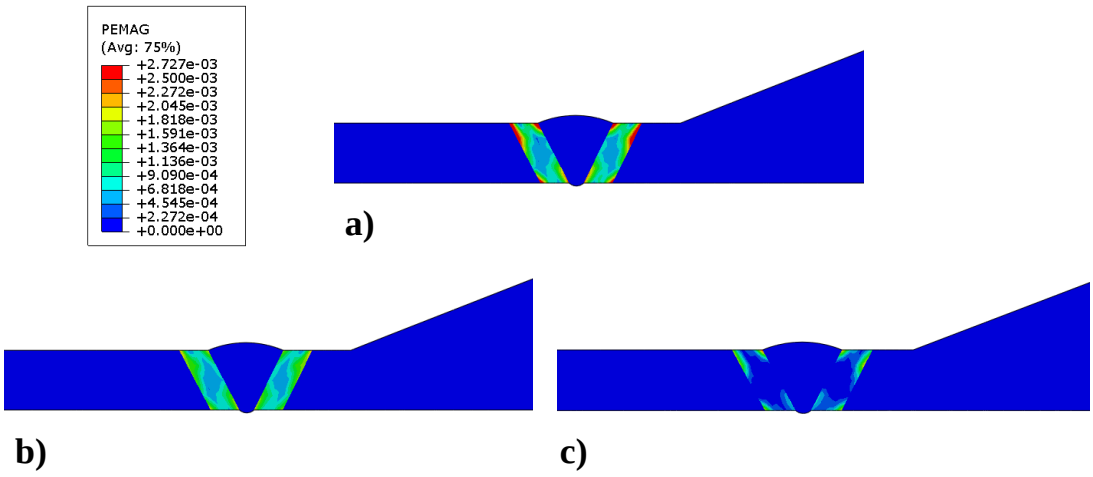

Figure 7-6 PEMAG for initial cycle a) loading without WRS; b) unloading without WRS; c) unloading with WRS.

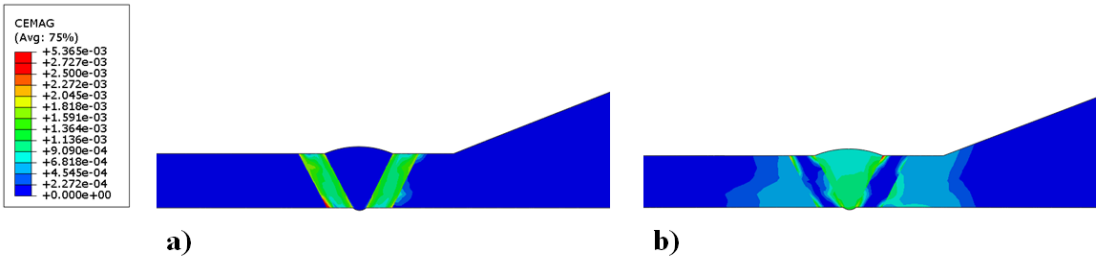

Figure 7-7 Comparison of the CEMAG at the end of first dwell a) without WRS; b) with WRS.

At different positions within the structure, depending on the state of the WRS and its magnitude, whether it is in tension or compression, it will have a different effect on the creep-cyclic plasticity interactions; hence, four critical elements are selected within the weldment region for further discussions, as presented in Figure 7-8. Figure 7-9 presents the hysteresis loops generated for the normal operation load, where the blue and red line corresponds to without WRS and with WRS loading respectively. For all the cases analysed, the steady-state response is obtained within the first few cycles itself. Under such scenarios, the general practice within R5 and ASME is to assume that the damage within the transient cycle is not prominent and the safe life is calculated with regard to the damage accumulation at steady-state. Nevertheless, if damage within the first few cycles is considerably high then R5 advises using an inelastic analysis to compute the damage accumulation within the transient cycles.

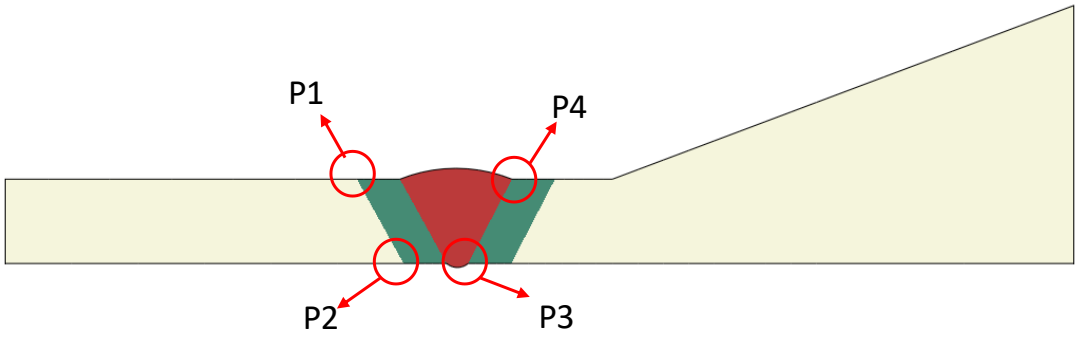

Figure 7-8 Positions of weld locations analysed.

At the element P1, the presence of WRS decreases both the plastic strain during the initial loading and the creep strain during the first dwell, resulting in a smaller hysteresis loop compared to the case without WRS. Similarly, at element P2, a decrease in the plastic and creep strain is observed. At both these elements, the resultant stress due to the thermo-mechanical loading is in compression, whereas the WRS is in tension. This results in a

decreased damage accumulation in the initial cycles, though they may have different effects at steady-state. For element P3, after the initial cycle, the structure exhibits an elastic response, the presence of the WRS exhibits a similar response but with a larger start of creep stress and a larger creep strain for the first cycle. Here, the mean stress increases in the presence of WRS, though this increase in the mean stress will only influence the HCF life. At element P4, the WRS is in compression while the resultant stress due to the thermo-mechanical loading is in tension. This again reduces the plastic strain, the creep strain and the start of dwell stress for the initial cycles. It should be noted that the change in the mean strain caused by the WRS at all the elements are quite different.

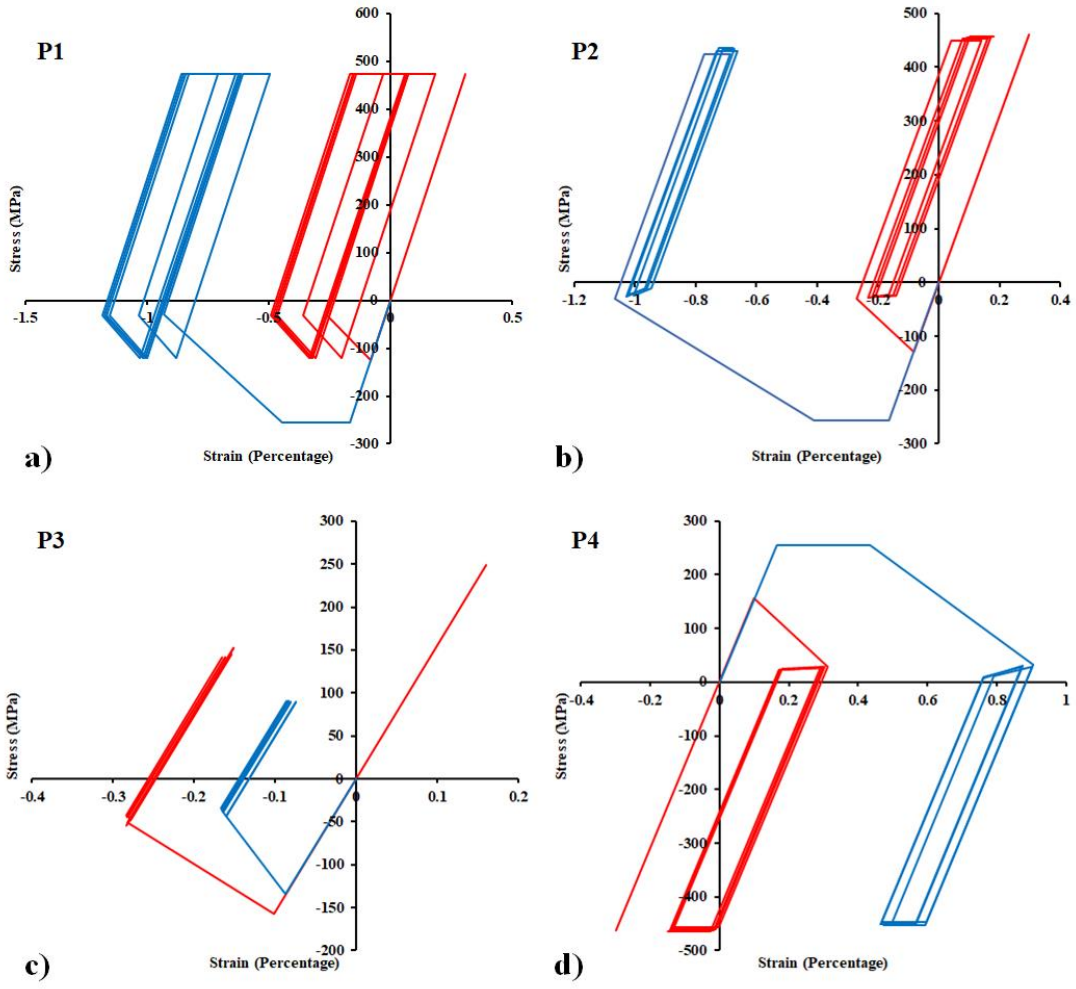

Figure 7-9 Comparison of hysteresis loop at the critical elements with (Red) and without WRS (Blue).

7.6 Effect of WRS on steady-state response

From the hysteresis loops presented earlier, it is clear that the WRS as such relaxes within the first few cycles and similar steady-state cyclic responses are observed with and without WRS. It has been reported extensively in the literature that the HCF of a component is affected by the mean stress; similarly, the LCF of a component is affected by its mean strain. Generally, a large mean strain is detrimental in terms of LCF life. Wenlan, W. *et al.* [132] has reported that for N80Q steel, a positive or negative mean strain results in a decrease in LCF life. For HS80H Wei, W *et al.* [133] has reported that the fatigue life decreases with an increase in the mean strain if the mean strain is greater than zero and the fatigue life increases for an increase in the mean strain if the mean strain is less than zero. Das, B. & Singh, A. [134] has reported that for P91 a reduction in the fatigue life was observed with an increase in the mean strain for the same strain amplitude. Hence, it can be understood that the mean strain has a significant role in the LCF damage of a component.

Though the WRS relaxes at an earlier stage, its effect on the mean strain might be significant. Revisiting the hysteresis loops presented in Figure 7-9, it is clear the WRS influences the resultant mean strain of the component. Figure 7-10 presents the evolution of PEMAG for P1, P2, and P4. In the case of P3, there is no plastic strain accumulation in any of the cycles. For all the three elements, the WRS results in a difference in the mean strain.

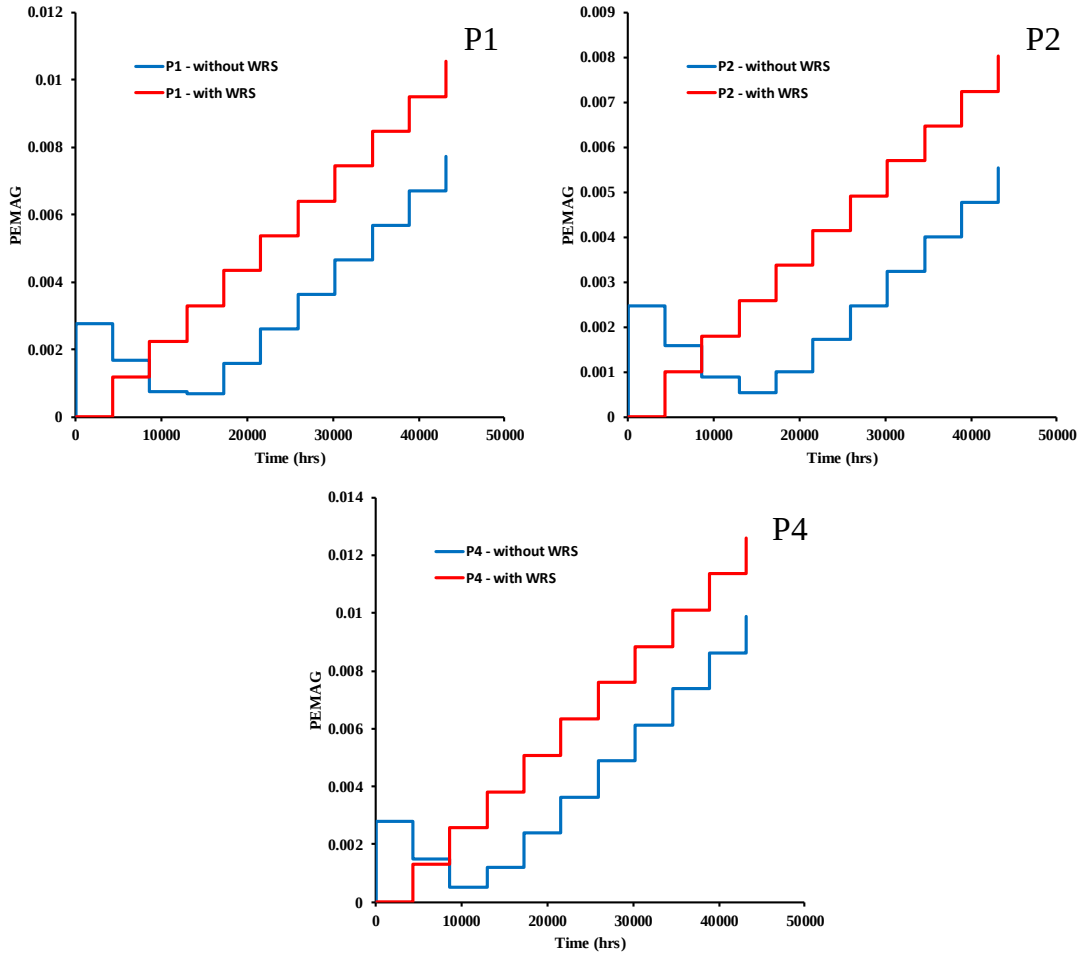

Figure 7-10 Evolution of PEMAG for critical elements.

It should be noted that Figure 7-10 is not an indication of ratcheting as the plastic strain accumulated during the steady-state cycle is compensated by the creep strain (presented in Figure 7-11). For P1, P2, and P4 the magnitude at which creep strain accumulation commences is reduced for the initial cycle with WRS, for the subsequent ones, the creep strain accumulated per cycle is very similar. For P3, WRS increases the magnitude at which creep strain accumulation commences but is restricted to the first cycle only after which no plastic or creep strain accumulation is observed.

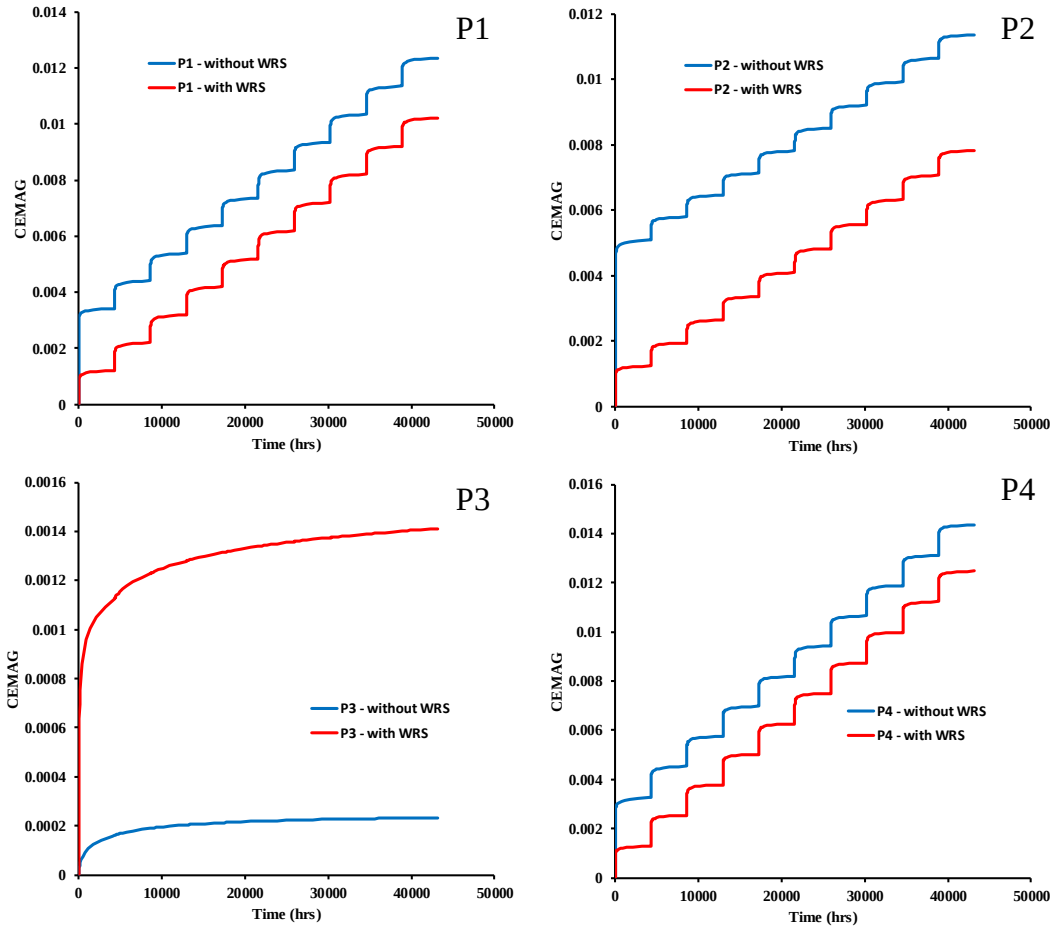

Figure 7-11 Evolution of CEMAG for critical elements.

7.6.1 Effect of mean strain on LCF life

Studies have shown that the detrimental effects of a tensile WRS on fatigue damage may be reduced by introducing a compressive residual stress [135]. A reason for this is that the mean strain is reduced resulting in lower fatigue damage and consequently a larger fatigue life. However an in-depth knowledge on the effect of mean strain on fatigue damage is still limited. The Manson-Coffin law introduced in Section 2.4.2, though widely used, does not account for the non-zero mean strain effects. Kondo Y. [136], has proposed a damage equation to account for the mean strain effects.

$$D_{FM} = \frac{N\left(\Delta\varepsilon_p/\varepsilon_0\right)^a}{\left(1-\frac{\left|\varepsilon_{pm}\right|}{\varepsilon_F}\right)^a} = 1 \tag{7-5}$$

where D_{FM} is the damage accumulated considering the mean strain, $\Delta\varepsilon_p$ is the plastic strain range, ε_0 and a are material constants, ε_{pm} is the mean strain and ε_F is the fracture ductility. This is based on the assumption that the mean strain affects the fracture ductility of the material, which in turn affects the LCF life. Equation (7-5) may be re-written in the following way to obtain the number of cycles.

$$\left(\frac{\left(\varepsilon_F - \left|\varepsilon_{pm}\right|\right).\varepsilon_0}{\Delta\varepsilon_p.\varepsilon_F}\right)^a = N \tag{7-6}$$

Another method discussed within the literature is based on the understanding that when the mean strain is greater than zero the tensile strain is greater than the compressive strain whereas when the mean strain is less than zero, the compressive strain is greater than the tensile strain [133]. For both instances, the amplitude used within the Manson-Coffin fatigue model is modified. When the mean strain is greater than zero, the half amplitude of the total strain is modified to ε_{pm} + ε_a. When the mean strain is less than zero, the half amplitude of the total strain is modified to ε_{pm} - ε_a. For the fatigue damage calculation in the next section, the Manson-Coffin fatigue model is used with the suggested modifications presented here to include the mean strain effects.

7.7 Creep-fatigue damage endurance

The aim of this section is not to provide a solid conclusion with respect to the life of the welded flange with or without WRS, instead, it compares the life considering the transient cycles and discusses the effect of WRS. The total damage is defined as:

$$D_{Total} = D_{CI} + D_{CS} + D_{FM} \tag{7-7}$$

where D_{Total} is the total damage, D_{CI} is the creep damage due to the transient cycles, D_{CS} is the creep damage at steady-state and D_{FM} is the fatigue damage considering the effect of mean strain. The initial data required for the damage assessment within the transient cycles are obtained using step-by-step inelastic analysis. This is then used as an input for the modified LMM eDSCA to account for the damage within the transient cycle and modify the fatigue

damage considering the mean strain. A flowchart is proposed in Figure 7-12 to exhibit the logic of the numerical investigation in this section.

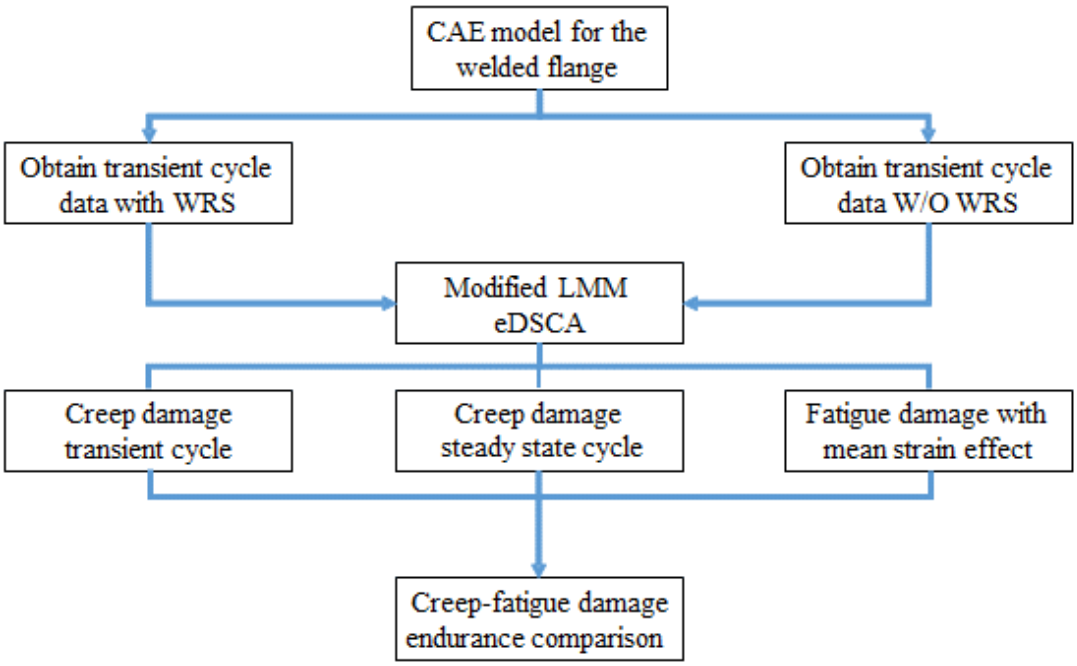

Figure 7-12 A flow chart for the creep-fatigue damage analysis through the modified LMM eDSCA method considering WRS.

The Manson-Coffin-Basquin equation is used for the construction of the fatigue curve for fatigue damage calculation. The same EN curve is used for all three zones. The values for the material constants for Manson-Coffin-Basquin equation for PM is obtained from [137] as σ_f' = 260 MPa; b = − 0.0319; c = − 0.5965; and ε_f' = 0.2918.

The TF method is used for assessing the creep damage. The creep-rupture properties are adopted from NIMS [123] and modified for the temperature of 600 ℃. The plot for creep rupture stress vs rupture time is presented in Figure 7-13.

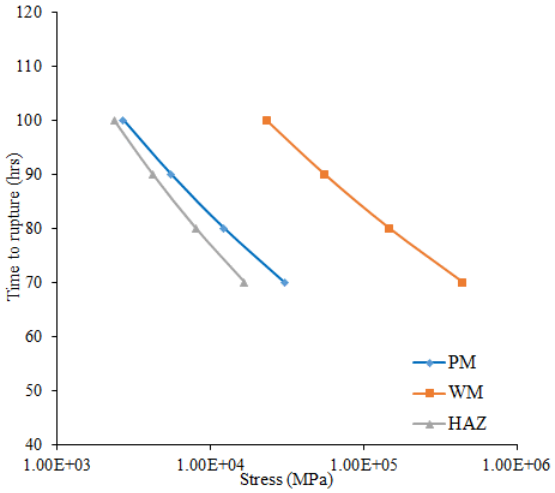

Figure 7-13 Creep rupture stress vs time to rupture diagram.

The rupture stress used for the creep damage is considered to be the average stress during the dwell period. It wouldn't be reasonable to use the arithmetic average of the start and end of dwell stress as it would produce overly conservative results considering the nonlinear stress relaxation during the dwell. Hence, the rupture stress is defined as below:

$$\sigma_{avg}(\Delta t, \sigma_1, Z) = \frac{1}{\Delta t}\int_0^{\Delta t} \sigma(\Delta t, \sigma_{cs}, Z)dt \tag{7-8}$$

where Z is the elastic follow up factor and σ_{cs} is the stress at the beginning of dwell period. For steady-state, the LMM subroutine calculates the elastic follow up factor, Z, which is used to calculate the average stress. For the initial cycle, the start of dwell stress, end of dwell stress, and creep strain obtained from the step-by-step analysis is used as an input in the modified LMM eDSCA subroutine which calculates the Z for the initial cycle and the subsequent average stress.

From the hysteresis loops and creep strain evolution plots presented in Figure 7-9 and Figure 7-10 respectively, it is clear that substantial creep strain/damage is accumulated within the initial cycles hence it is only reasonable that they are also accounted for in the damage assessment. Table 7-6 presents a comparison of the damage accumulation for the three main scenarios considered a) without transient/WRS effect and without the effect of mean strain on steady-state cycle (Scenario A); b) without WRS effect on transient cycle but with the effect of mean strain on steady-state cycle (Scenario B); c) with WRS effect on transient cycle and

with the effect of mean strain on steady-state cycle (Scenario C). In the absence of mean strain effect on fatigue damage, the equivalent fatigue damage per cycle is not significant. The maximum fatigue damage, which is observed in P4 is in the order of 10^{-4}. The total damage, which is calculated as the sum of the creep damage and the fatigue damage, as such is driven by the creep damage. In effect, the total damage is significant in the same order of creep damage with P1 and P4 indicating similar damage accumulation.

Table 7-6 Comparisons of creep, fatigue and total damage.

Creep Damage				
Element No.	P1	P2	P3	P4
Scenario A	0.0029	0.0025	0	0.0033
Scenario B	0.0074	0.0081	0.0011	0.012
Scenario C	0.0033	0.0036	0.003	0.0079

Fatigue damage				
Element No.	P1	P2	P3	P4
Scenario A	0.0006	0.0004	-	0.0006
Scenario B	0.0068	0.0029	-	0.0049
Scenario C	0.0021	0.0003	-	0.0011

Total damage				
Element No.	P1	P2	P3	P4
Scenario A	0.0036	0.0029	0.0002	0.0039
Scenario B	0.017	0.0135	0.0011	0.0203
Scenario C	0.0083	0.0064	0.003	0.0123

The creep damage within the transient cycle with and without WRS is quite substantial and larger than the creep damage per cycle at steady-state. At locations, P3 where the start of dwell stress is increased due to WRS, the magnitude of creep damage slightly increases, and at the other elements where the start of dwell stress is reduced, due to WRS, the creep damage also decreases.

For scenario B, the order and significance of fatigue damage changes substantially. In elements P1, P2, and P4, the fatigue damage per cycle increases on a scale comparable to the creep damage. At element P3, at steady-state, an elastic response is observed, hence the mean strain doesn't have an effect on the LCF but would have an effect in the HCF life. Considering the structure as a whole, the effect on the HCF life is not significant and crack initiation will be due to the LCF-creep interaction. The total damage is in the order of P4>P1>P2.

Considering scenario C, the presence of the WRS acts beneficial to the fatigue damage. Within elements P1, P2, and P4 the WRS, as discussed in the earlier sections, WRS reduces the plastic strain accumulation within the initial cycles and thereby the mean strain. As seen in Table 7-6, the fatigue damage is reduced within these three elements and the order in which it is reduced depends on the reduction in the mean strain.

From the results presented in Table 7-6, a concrete relationship between creep-fatigue-mean strain-WRS cannot be drawn. Nevertheless, it throws light on the importance of mean strain at steady-state. It is recommended that even for damage calculation at steady-state a thorough investigation considering the change in the mean strain during the transient cycle should be carried out. The presence of the WRS in this regard can act beneficially if its direction is opposite to that of the resultant forces during the initial cycle.

7.8 Chapter summary

Creep-cyclic plasticity and creep-fatigue damage analysis of a welded flange are analysed considering both the thermo-mechanical load and the WRS. The WRS is calculated in two steps using an in-elastic FE analysis. The first step involves simulating the temperature history which is then used within the static analysis to calculate the final WRS.

The presence of WRS is found to have a minimal effect on the shakedown and ratcheting interaction curve, though the stress distribution changes considerably in the presence of WRS. The residual stress within the structure redistributes itself to accommodate the WRS so that the shakedown-ratchet limit curve remains the same. The effect of WRS is predominant for the initial cycles after which it relaxes so that at steady-state the creep-cyclic plasticity response is similar for with and without WRS. The resultant load produced compressive stress within the HAZ compared to the tensile stress induced by the WRS, which was beneficial in

terms of creep-fatigue damage. However, within the root pass region in the WM, which exhibits elastic response at steady-state, large creep damage was observed during the initial cycles, which is exacerbated by WRS.

The LMM eDSCA subroutine was modified to assess the creep-fatigue damage considering both transient cycles and WRS. This is employed by obtaining critical data for the transient cycles such as the start of dwell stress, end of dwell stress, and mean strain by step-by-step analysis, which is then used as inputs within the LMM eDSCA subroutine to calculate the total damage. For the damage calculations undertaken, the consideration of WRS and mean strain, vary the damage distribution and peak considerably. In effect it can be observed that the WRS stress largely affects the fatigue tolerance due to the change it causes on the mean strain. In case of multiple bead the evolution of WRS will be even more complex but finally they will alter the mean strain and thereby the fatigue life.

Chapter 8 Conclusions and future work

8.1 Conclusions

The work presented in this thesis deals with the cyclic plasticity and creep-cyclic plasticity investigation of welded components commonly found in power plants. Chapter 1 provides a brief introduction and presents the thesis objectives. Chapter 2 provides an insight to the major damage mechanisms observed in high-temperature service structures, and discusses the R5 and ASME damage evaluation methodology. Chapter 3 introduces the LMMF and presents the numerical procedure for the shakedown, ratchet analysis and the eDSCA analysis. The results presented from Chapter 4 through Chapter 7 identify various damage mechanisms within welded components with the use of LMM. The main outcomes can be summarised as below:

1. Identified the effect of weld material properties and geometry on the ratchet limit curves.
2. Derived two semi-empirical equations based on the parametric studies which can be used to predict the limit load of welded pipes in the specified range without performing complex FE analysis
3. The creep damage, fatigue damage; creep-fatigue and creep-ratcheting interaction studies of welded components commonly found in power plant have been performed.
4. Enhanced the UMAT to account for additional stresses such as the WRS.
5. Combined the LMM with in elastic FE analysis to investigate the creep-fatigue endurance considering the transient cycles and WRS.

A parametric study on the ratchet limit and cyclic response assessment of a welded pipe subjected to constant pressure and cyclic thermal load is presented in Chapter 4. The results obtained demonstrate that the σ_y^{WM} and the R_i/t ratio have the most influence on the ratchet-interaction curve. As such for lower values of σ_y^{WM} the secondary stress becomes more prominent with the welded pipe experiencing thermal ratcheting. In general, from the most critical results, two semi-empirical equations have been derived which can be used to predict the limit load of welded pipes in the specified range without performing complex FE analysis.

To understand the creep damage, fatigue damage; creep-fatigue and creep-ratcheting interaction of welds, several case studies of components commonly found in power plant are undertaken within this work and presented in Chapter 5 and 6. The results demonstrate that the presence of welds have a significant influence on the damage mechanism and safe life of components. In addition to enhancing the already present damage mechanism, they also introduce additional damage mechanism. Studies also demonstrate that in most cases, the thermal load has a larger effect compared to mechanical load due to the difference in the coefficient of thermal expansion. The introduction of dwell time, leads to creep strain accumulation throughout the weldment. In certain areas, the reverse plasticity and creep strain compensate each other while at other areas they don't, this leads to creep-fatigue and creep-ratcheting at the same time at different locations. Hence it is critical that all the regions receive due consideration while conduction damage analysis.

Creep-cyclic plasticity and creep-fatigue damage analysis of a welded flange are analysed considering both the thermo-mechanical load and the WRS in Chapter 7. The presence of WRS has a minimal effect on the shakedown and ratcheting interaction curve, though the stress distribution changes considerably in the presence of WRS. The effect of WRS is predominant for the initial cycles after which it relaxes so that at steady-state the creep-cyclic plasticity response is similar with and without WRS. The LMM eDSCA subroutine was modified to assess the creep-fatigue damage considering both transient cycles and WRS. This is done by providing data for the transient cycles such as the start of dwell stress, end of dwell stress, and mean strain as inputs within the LMM eDSCA subroutine to calculate the total damage. Results further demonstrate that the presence of weldment induces tensile and compressive stress/strain at the vicinity of the weldment, which substantially influences the creep and fatigue damage. The presence of WRS further complicates this. Based on the location and direction of the resultant load, the WRS can have a beneficial or detrimental effect on creep-fatigue life.

8.2 Future work

Though the LMMF has been developed further compared to most direct methods, there are various areas with still scope for improvements.

Currently, EPP and RO models are used to account for the plasticity. When compared to actual structures that may experience isotropic, kinematic, or combined isotropic and kinematic hardening behaviour, the LMM tends to produce conservative results. The implementation of such hardening behaviours within the framework is an area of interest and requires further exploration. Further the LMM only considers structures that can attain steady state, but it is recognized that this is not the case always, and it is of interest to build in provisions within LMM to recognize such interactions and to extend the methodology to access the behavior during transient cycles.

Similarly, the current approach to calculate the creep strain is by using the time hardening power law, but it is known that in many scenarios more accurate creep behaviour is predicted by different creep constitutive models such as the strain hardening power-law or the hyperbolic sine law. Further, fatigue and creep crack propagation are areas equally important to crack initiation. It would be beneficial if the LMM can be further researched and improved to account for crack propagation also. But the implementation of this is a challenge that will require considerable modification within the framework.

The LMM plugin for limit load and shakedown analysis has been acknowledged and accepted by the R5. Plug-in for LMM eDSCA is currently being developed within Structural Integrity and Life Assessment (SILA) group. Though this will be helpful for engineers or researchers with minimal knowledge of the working of LMM or UMAT coding, it does not have the option to post-process the results. It would be beneficial if the plugin provides the user with options to choose between the high-temperature design code and provide results after post-processing. Another suggestion is to add an option within the plugin to export stress data from a previous analysis such a WRS, or strain data such as a body that is pre-strained before putting into service.

References

[1] A. N. S. Publication, “UK energy in brief 2019,” *DECC-Department Energy Clim. Chang.*, 2019.

[2] D. Contu and S. Mourato, “Complementing choice experiment with contingent valuation data: Individual preferences and views towards IV generation nuclear energy in the UK,” *Energy Policy*, vol. 136, p. 111032, 2020.

[3] R. Beesley, “Crack growth modelling from stress concentrations under cyclic loading histories,” *EngD Thesis, Univ. Strat.*, 2017.

[4] The Role of Nuclear Energy in a Low-carbon Energy Future, *OECD/NEA*, vol. 6887. 2012.

[5] M. Li, R. A. Barrett, S. Scully, N. M. Harrison, S. B. Leen, and P. E. O’Donoghue, “Cyclic plasticity of welded P91 material for simple and complex power plant connections,” *Int. J. Fatigue*, vol. 87, pp. 391–404, 2016.

[6] T. Shrestha, “Creep deformation, rupture analysis, heat treatment and residual stress measurement of monolithic and welded grade 91 steel for power plant,” *PhD Thesis, Univ. Idaho*, 2013.

[7] M. Joyce, “Chapter 11 - Advanced reactors and future concepts,” M. B. T.-N. E. Joyce, Ed. Butterworth-Heinemann, 2018, pp. 263–295.

[8] D. W. J. Tanner, “Life assessment of welded INCONEL 718 at high temperature,” *PhD thesis, Univ. Nottingham*, 2009.

[9] D. W. Dean and J. G. Johns, “Structural integrity issues in high temperature nuclear plant : Experience from operation of the uk advanced gas cooled reactor fleet,” *Trans. SMiRT-23 Manchester, United Kingdom*, 2015.

[10] G. Rayner, “Creep of welded branched pipes,” *PhD thesis, Univ. Nottingham*, 2004.

[11] N. G. Smith and D. W. Dean, “Structural integrity assessment of weldments at high temperature: A proposed new approach for R5,” *Int. J. Press. Vessel. Pip.*, vol. 87, no. 11, pp. 664–668, 2010.

[12] J. Bree, “Elastic-plastic behaviour of thin tubes subjected to internal pressure and intermittent high-heat fluxes with application to fast-nuclear-reactor fuel elements,” *J. Strain Anal.*, vol. 2, no. 3, pp. 226–238, 1967.

[13] J. Ure, “An advanced lower and upper bound shakedown analysis method to enhance the R5 high temperature assessment procedure,” *PhD Thesis, Univ. Strat.*, 2013.

[14] E. Melan, “Theorie statisch unbestimmter Systeme aus ideal-plastischem Baustoff,” Hölder-Pichler-Tempsky in Komm., 1936.

[15] W. T. Koiter, “General theorems for elastic-plastic solids, ” North-Holland, 1960.

[16] K. Zhang, “Characterization and modeling of the ratcheting behavior of the ferritic-martensitic steel P91,” *PhD Thesis, Karlsruher Institut für Technologie (KIT)*, 2017.

[17] H. Hübel, “Basic conditions for material and structural ratcheting,” *Nucl. Eng. Des.*, vol. 162, no. 1, pp. 55–65, 1996.

[18] S. K. Paul, “A critical review of experimental aspects inratcheting fatigue: Microstructure to specimen tocomponent,” *J. Mater. Res. Technol.*, vol. 8, no. 5, pp. 4894–4914, 2019.

[19] P. J. Amstrong and C. O. Frederick, “A mathematical represention of the multiaxial bauschinger effect,” *CEGB Rep. No. RD / B /N 731*, pp. 1–24, 1966.

[20] J. L. Chaboche, “Continuous damage mechanics - A tool to describe phenomena before crack initiation,” *Nucl. Eng. Des.*, vol. 64, no. 2, pp. 233–247, 1981.

[21] J. L. Chaboche, “Constitutive equations for cyclic plasticty and cyclic viscoplasticity,” *Int. J. Plast.*, vol. 5, pp. 247–302, 1989.

[22] J. L. Chaboche, “On some modifications of kinematic hardening to improve the description of ratchetting effects,” *Int. J. Plast.*, vol. 7, no. 7, pp. 661–678, 1991.

[23] Q. Meng and Z. Wang, “Creep damage models and their applications for crack growth analysis in pipes: A review,” *Eng. Fract. Mech.*, vol. 205, pp. 547–576, 2019.

[24] J. T. BOYLE and J. SPENCE, “Chapter 3 - Simple component behaviour,” J. T. BOYLE and J. B. T.-S. A. for C. SPENCE, Eds. Butterworth-Heinemann, 1983, pp. 21–38.

[25] D. Barbera, H. Chen, and Y. Liu, “On creep fatigue interaction of components at elevated temperature,” *J. Press. Vessel Technol.*, vol. 138, no. 4, p. 041403, 2016.

[26] D. Barbera, “On the evaluation of high temperature creep-fatigue responses of structures,” *PhD Thesis, Univ. Strat.*, 2017.

[27] J. Schijve, Ed., “Introduction to fatigue of structures and materials,” in *Fatigue of Structures and Materials*, Dordrecht: Springer Netherlands, 2009, pp. 1–9.

[28] F. C. Campbell, Ed., “Elements of metallurgy and engineering alloys.” ASM International, 01-Jun-2008.

[29] Q. Xin, “Durability and reliability in diesel engine system design,” *Diesel Engine Syst. Des.*, pp. 113–202, 2013.

[30] U. Muralidharan and S. S. Manson, “A modified universal slopes equation for

estimation of fatigue characteristics of metals," *J. Eng. Mater. Technol.*, vol. 110, no. 1, pp. 55–58, Jan. 1988.

[31] M. F. Harun, R. Mohammad, N. Othman, A. Amrin, S. Chelliapan, and N. Maarop, "Methods for estimating the fatigue properties of UNS C70600 copper-nickel 90/10," *Int. J. Mech. Eng. Technol.*, vol. 8, no. 11, pp. 413–422, 2017.

[32] K. S. Lee and J. H. Song, "Estimation methods for strain-life fatigue properties from hardness," *Int. J. Fatigue*, vol. 28, no. 4, pp. 386–400, 2006.

[33] J. H. Ong, "An improved technique for the prediction of axial fatique life from tensile data," *Int. J. Fatigue*, vol. 15, no. 3, pp. 213–219, 1993.

[34] J.-H. Park and J.-H. Song, "New estimation method of fatigue properties of aluminum alloys," *J. Eng. Mater. Technol.*, vol. 125, no. 2, p. 208, 2003.

[35] M. A. Meggiolaro and J. T. P. Castro, "Statistical evaluation of strain-life fatigue crack initiation predictions," *Int. J. Fatigue*, vol. 26, no. 5, pp. 463–476, 2004.

[36] A. Baumel Jr and T. Seeger, *Material Data for Cyclic Loading —supplement I. Amsterdam*. Elsevier Science Publishers, 1990.

[37] M. L. Roessle and A. Fatemi, "Strain-controlled fatigue properties of steels and some simple approximations," *Int. J. Fatigue*, vol. 22, no. 6, pp. 495–511, 2000.

[38] M. MR, S. DF, and C. EM, "Fundamentals of modern fatigue analysis," *Fract. Control Progr. Rep. No. 26, Univ. Illinois, USA*, pp. 385 – 410, 1977.

[39] M. W. Spindler, "An improved method for calculation of creep damage during creep-fatigue cycling," *Mater. Sci. Technol.*, vol. 23, no. 12, pp. 1461–1470, 2007.

[40] M. W. Spindler, "An improved method to calculate the creep-fatigue endurance of Type 316H stainless steel," *Mater. Adv. Power Eng.*, pp. 1673–1682, 2006.

[41] M. W. Spindler and W. M. Payten, "Advanced ductility exhaustion methods for the calculation of creep damage during creep-fatigue cycling," *Int. Symp. Creep Fatigue Interact. Test Methods Model.*, vol. 8, no. 7, pp. 102-102–26, 2012.

[42] R. P. Skelton and D. Gandy, "Creep-fatigue damage accumulation and interaction diagram based on metallographic interpretation of mechanisms," *Mater. High Temp.*, vol. 25, no. 1, pp. 27–54, 2008.

[43] A. and P. V. C. NH-Boiler, "Section III, Division 1, Subsection NH, Class 1 Components in Elevated Temperature Service.," *Am. Soc. Mech. Eng.*, 2014.

[44] EDF Energy, "R5 Assessment procedure for the high temperature response of structures." .

[45] AWS A2 Committee on Definitions and Symbols, "Standard welding terms and

definitions," p. 147, 2001.

[46] W. Sun, "Creep of service-aged welds," *PhD thesis, Univ. Nottingham*, 1996.

[47] S. B. Bhoje and P. Chellapandi, "Creep fatigue design of FBR components, in creep-fatigue damage rules for advanced fast reactor design, " *Int. At. Energy Agency*, no. 13, pp. 97–115, 1997.

[48] A. Khajuria, R. Kumar, R. Bedi, J. Swaminanthan, and D. K. Shukla, "Impression creep studies on simulated reheated haz of P91 and P91b steels," *Int. J. Mod. Manuf. Technol.*, vol. 10, no. 1, pp. 50–56, 2018.

[49] S. A. David, J. A. Siefert, and Z. Feng, "Welding and weldability of candidate ferritic alloys for future advanced ultrasupercritical fossil power plants," *Sci. Technol. Weld. Join.*, vol. 18, no. 8, pp. 631–651, Nov. 2013.

[50] J. Parker, "Factors affecting Type IV creep damage in Grade 91 steel welds," *Mater. Sci. Eng. A*, vol. 578, pp. 430–437, 2013.

[51] M. Saber, "Experimental and finite element studies of creep and creep crack growth in P91 and P92 weldments.," *PhD thesis, Univ. Nottingham*, 2012.

[52] W. Sun, T. H. Hyde, A. A. Becker, and J. A. Williams, "Comparison of the creep and damage failure prediction of the new, service-aged and repaired thick-walled circumferential CrMoV pipe welds using material properties at 640°C," *Int. J. Press. Vessel. Pip.*, vol. 77, no. 7, pp. 389–398, 2000.

[53] S. L. Mannan and M. Valsan, "High-temperature low cycle fatigue, creep-fatigue and thermomechanical fatigue of steels and their welds," *Int. J. Mech. Sci.*, vol. 48, no. 2, pp. 160–175, 2006.

[54] C. Becht, "New weld joint strength reduction factors in the creep regime in ASME B31.3 piping," *J. Press. Vessel Technol.*, vol. 128, no. 1, p. 46, 2006.

[55] M. D. Mathew, S. Latha, and K. B. S. Rao, "An assessment of creep strength reduction factors for 316L(N) SS welds," *Mater. Sci. Eng. A*, vol. 456, no. 1–2, pp. 28–34, 2007.

[56] P. Chellapandi and S. C. Chetal, "Influence of mis-match of weld and base material creep properties on elevated temperature design of pressure vessels and piping," *Nucl. Eng. Des.*, vol. 195, no. 2, pp. 189–196, 2000.

[57] B. Rivolta, F. Tavasci, R. Gerosa, and J. Yenus, "High-temperature mechanical properties of P91 weld metal," *Mater. Perform. Charact.*, vol. 6, no. 1, p. MPC20150054, 2017.

[58] Y. Takahashi and M. Tabuchi, "Evaluation of creep strength reduction factors for welded joints of HCM12A (P122)," Proceedings of the ASME 2006 Pressure Vessels

and Piping/ICPVT-11 Conference. Volume 6: Materials and Fabrication. *Vancouver, BC, Canada. July 23–27*, pp. 529-534, 2006.

[59] D. H. Kumar and a. S. Reddy, "Study of mechanical behavior in austenitic stainless steel 316 Ln welded joints," *Int J Mech Eng Robot. Res.*, vol. 2, no. 1, pp. 1–22, 2013.

[60] S. Spigarelli and E. Quadrini, "Analysis of the creep behaviour of modified P91 (9Cr-1Mo-NbV) welds," *Mater. Des.*, vol. 23, no. 6, pp. 547–552, 2002.

[61] R. A. Ainsworth and P. J. Budden, "Design and assessment of components subjected to creep," *J. Strain Anal. Eng. Des.*, vol. 29, no. 3, pp. 201–207, 2007.

[62] N. Cho, "Structural integrity assessment of engineering components under cyclic loading at high temperature," *PhD Thesis, Univ. Strat.*, 2019.

[63] R. A. Ainsworth, "R5 procedures for assessing structural integrity of components under creep and creep–fatigue conditions," *Int. Mater. Rev.*, vol. 51, no. 2, pp. 107–126, 2006.

[64] D. M. Knowles, "R5 high temperature creep-fatigue life assessment for austenitic weldments," *Procedia Eng.*, vol. 86, pp. 315–326, 2014.

[65] H. Y. Lee, "Comparison of elevated temperature design codes of ASME Subsection NH and RCC-MRx," *Nucl. Eng. Des.*, vol. 308, pp. 142–153, 2016.

[66] G.-H. Koo and J.-H. Lee, "High temperature structural integrity evaluation method and application studies by ASME-NH for the next generation reactor design," *J. Mech. Sci. Technol.*, vol. 20, no. 12, pp. 2061–2078, 2006.

[67] T. Li, H. Chen, W. Chen, and J. Ure, "On the Ratchet Analysis of a Cracked Welded Pipe," *J. Press. Vessel Technol.*, vol. 134, no. 1, p. 011203, 2012.

[68] J. Abou-Hanna and T. E. McGreevy, "A simplified ratcheting limit method based on limit analysis using modified yield surface," *Int. J. Press. Vessel. Pip.*, vol. 88, no. 1, pp. 11–18, 2011.

[69] D. Mackenzie, J. T. Boyle, and R. Hamilton, "Elastic compensation method for limit and shakedown analysis: A review," *J. Strain Anal. Eng. Des.*, vol. 35, no. 3, pp. 171–188, 2000.

[70] R. Seshadri, "Inelastic evaluation of mechanical and structural components using the generalized local stress strain method of analysis," *Nucl. Eng. Des.*, vol. 153, no. 2–3, pp. 287–303, 1995.

[71] H. Chen, W. Chen, T. Li, and J. Ure, "On shakedown, ratchet and limit analyses of defective pipeline," *J. Press. Vessel Technol.*, vol. 134, no. 1, p. 011202, 2011.

[72] H. Chen and A. R. S. Ponter, "Linear matching method on the evaluation of plastic and creep behaviours for bodies subjected to cyclic thermal and mechanical loading," *Int.*

J. Numer. Methods Eng., vol. 68, no. 1, pp. 13–32, 2006.

[73] H. Chen, J. Ure, and D. Tipping, "Integrated structural analysis tool using the Linear Matching Method part 2 - Application and verification," *Int. J. Press. Vessel. Pip.*, vol. 120–121, no. 1, pp. 152–161, 2014.

[74] J. Ure, H. Chen, and D. Tipping, "Integrated structural analysis tool using the linear matching method part 1 - Software development," *Int. J. Press. Vessel. Pip.*, vol. 120–121, no. 1, pp. 141–151, 2014.

[75] H. Chen, W. Chen, and J. Ure, "A direct method on the evaluation of cyclic steady state of structures with creep effect," *J. Press. Vessel Technol.*, vol. 136, no. 6, p. 061404, 2014.

[76] H. F. Chen and A. R. S. Ponter, "Shakedown and limit analyses for 3-D structures using the linear matching method," *Int. J. Press. Vessel. Pip.*, vol. 78, no. 6, pp. 443–451, 2001.

[77] H. F. Chen, M. J. Engelhardt, and A. R. S. Ponter, "Linear matching method for creep rupture assessment," *Int. J. Press. Vessel. Pip.*, vol. 80, no. 4, pp. 213–220, 2003.

[78] A. R. S. Ponter and H. Chen, "A minimum theorem for cyclic load in excess of shakedown, with application to the evaluation of a ratchet limit," *Eur. J. Mech. A/Solids*, vol. 20, no. 4, pp. 539–553, 2001.

[79] C. E. Jaske, "Fatigue-strength-reduction factors for welds in pressure vessels and piping," *J. Press. Vessel Technol.*, vol. 122, no. 3, p. 297, 2002.

[80] A. M. Clayton, "Thermal shock in nuclear reactors," *Prog. Nucl. Energy*, vol. 12, no. 1, pp. 57–83, 1983.

[81] H. Chou, "Structural reliability evaluation on the pressurized water reactor pressure vessel under pressurized thermal shock events," *Proc. ASME 2014 Press. Vessel. Pip. Conf. Vol. 7 Oper. Appl. Components*, pp. 1–9, 2014.

[82] J. Ure, H. Chen, and D. Tipping, "Calculation of a lower bound ratchet limit part 2 – Application to a pipe intersection with dissimilar material join," *Eur. J. Mech. - A/Solids*, vol. 37, pp. 369–378, 2013.

[83] T. Li, H. Chen, W. Chen, and J. Ure, "On the shakedown analysis of welded pipes," *Int. J. Press. Vessel. Pip.*, vol. 88, no. 8–9, pp. 301–310, 2011.

[84] M. F. Harun, R. Mohammad, and A. Kotousov, "Low cycle fatigue behavior of elbows with local wall thinning," *Metals (Basel).*, vol. 10, no. 2, pp. 1–9, 2020.

[85] G. E. Varelis and S. A. Karamanos, "Low-cycle fatigue of pressurized steel elbows under in-plane bending," *J. Press. Vessel Technol. Trans. ASME*, vol. 137, no. 1, pp.

1–10, 2015.

[86] Y. Madi, P. Matheron, N. Recho, and P. Mongabure, “Low cycle fatigue of welded joints : new experimental approach,” *Nucl. Eng. Des.*, vol. 228, pp. 161–177, 2004.

[87] G. V. Prasad Reddy, R. Sandhya, M. Valsan, and K. Bhanu Sankara Rao, “High temperature low cycle fatigue properties of 316(N) weld metal and 316L(N)/316(N) weld joints,” *Int. J. Fatigue*, vol. 30, no. 3, pp. 538–546, 2008.

[88] A. Shibli and F. Starr, “Some aspects of plant and research experience in the use of new high strength martensitic steel P91,” *Int. J. Pres. Ves & Piping*, vol. 84, pp. 114–122, 2007.

[89] T. P. Farragher, S. Scully, N. P. O’Dowd, C. J. Hyde, and S. B. Leen, “High temperature, low cycle fatigue characterization of P91 weld and heat affected zone material,” *J. Press. Vessel Technol. Trans. ASME*, vol. 136, no. 2, pp. 1–10, 2014.

[90] G. Dundulis, R. Janulionis, A. Grybėnas, V. Makarevičius, and R. Dundulis, “Numerical and experimental investigation of low cycle fatigue behaviour in P91 steel,” *Eng. Fail. Anal.*, vol. 79, no. May, pp. 285–295, 2017.

[91] T. H. Hyde and W. Sun, “Creep failure behaviour of a circumferential P91 pipe weldment with an anisotropic weld metal subjected to internal pressure and end load,” *Proc. Inst. Mech. Eng. Part L J. Mater. Des. Appl.*, vol. 220, no. 3, pp. 147–162, 2006.

[92] T. Nps and I. Standard, “Pipe Flanges and Flanged Fittings,” vol. 2003, 2008.

[93] “Data sheets on the elevated-temperature properties. NIMS Creep Datasheet No. 4B. Tsukuba, Japan: National Institute for Materials Science.”

[94] “Data sheets on the elevated-temperature properties. NIMS Creep Datasheet No. 57A. Tsukuba, Japan: National Institute for Materials Science.”

[95] A. Sorkhabi, and F. V. Tahami, “Experimental study of the creep behavior of parent , simulated HAZ and weld materials for cold-drawn 304L stainless steel,” *Eng. Fail. Anal.*, vol. 21, pp. 78–90, 2012.

[96] A. Sorkhabi, and F. V. Tahami, “Creep constitutive equation for 2- materials of weldment-304L stainless steel,” *Int. J. Mech & Mechatronics*, vol. 6, no. 1, 2012.

[97] Y. Takahashi, B. Dogan, and D. Gandy, “Systematic evaluation of creep-fatigue life prediction methods for various alloys,” *J. Press. Vessel Technol. Trans. ASME*, vol. 135, no. 6, pp. 1–10, 2013.

[98] M. W. Spindler, “Report AGR Creep-Fatigue Endurance of Type 316H Parent,” pp. 1–104, 2018.

[99] D. W. J. Tanner, M. Puliyaneth, W. Sun, and T. H. Hyde, “Creep damage modelling of

P92 pipe weld at 675°C," *Mater. Sci. Technol.*, vol. 30, no. 1, pp. 6–11, 2014.

[100] Y. Li, H. Hongo, M. Tabuchi, Y. Takahashi, and Y. Monma, "Evaluation of creep damage in heat affected zone of thick welded joint for Mod.9Cr-1Mo steel," *Int. J. Press. Vessel. Pip.*, vol. 86, no. 9, pp. 585–592, 2009.

[101] T. Ogata, T. Sakai, and M. Yaguchi, "Damage assessment method of P91 steel welded tube under internal pressure creep based on void growth simulation," *Int. J. Press. Vessel. Pip.*, vol. 87, no. 11, pp. 611–616, 2010.

[102] T. Ogata, T. Sakai, and M. Yaguchi, "Damage characterization of a P91 steel weldment under uniaxial and multiaxial creep," *Mater. Sci. Eng. A*, vol. 510–511, no. C, pp. 238–243, 2009.

[103] S. Goyal and K. Laha, "Creep life prediction of 9Cr-1Mo steel under multiaxail state of stress," *Mater. Sci. Eng. A*, vol. 615, pp. 348-360, 2014.

[104] L. B. Borkowski and A. Staroselsky, "Effect of compressive creep on fracture toughness: application to Thermomechanical Fatigue (TMF) life prediction," *Int. J. Fract.*, vol. 222, pp. 231–236, 2020.

[105] N. Gao, M. W. Brown, K. J. Miller, and P. A. S. Reed, "An effective method to investigate short crack growth behaviour by reverse bending testing," *Int. J. Fatigue*, vol. 29, no. 3, pp. 565–574, 2007.

[106] S. P. Zhu, H. Z. Huang, Y. U. Liu, R. Yuan, and L. He, "An efficient life prediction methodology for low cycle fatigue–creep based on ductility exhaustion theory," *Int. J. Damage Mech.*, vol. 22, no. 4, pp. 556–571, 2013.

[107] T. Goswami and H. Hanninen, "Dwell effects on high temperature fatigue behavior. Part I," *Mater. Des.*, vol. 22, no. 3, pp. 199–215, 2001.

[108] T. Goswami and H. Hänninen, "Dwell effects on high temperature fatigue damage mechanisms. Part II," *Mater. Des.*, vol. 22, no. 3, pp. 217–236, 2001.

[109] V. Shankar, K. Mariappan, R. Sandhya, K. Laha, and A. K. Bhaduri, "Long term creep-fatigue interaction studies on India-specific reduced activation ferritic-martensitic (IN-RAFM) steel," *Int. J. Fatigue*, vol. 98, pp. 259–268, 2017.

[110] Y. Gorash and H. Chen, "Creep-fatigue life assessment of cruciform weldments using the linear matching method," *Int. J. Press. Vessel. Pip.*, vol. 104, pp. 1–13, 2013.

[111] M. Puliyaneth, H. Chen, and W. Luan, "Creep fatigue damage assessment of V-butt weld pipe with an extended direct steady cycle analysis," *Am. Soc. Mech. Eng. Press. Vessel. Pip. Div. PVP*, vol. 5, pp. 1–9, 2018.

[112] S. S. Manson and G. R. Halford, *Fatigue and Durability of Metals at High*

Temperatures. 2009.

[113] T. Asayama, "Creep-fatigue evaluation of stainless steel welded joints in FBR class 1 components," *Nucl. Eng. Des.*, vol. 198, no. 1, pp. 25–40, 2000.

[114] Y. Yang and W. C. Mohr, "Weld residual stress and creep-fatigue analysis of a furnace roll in a continuous hot dip coating line," *Proc. ASME 2016 Press. Vessel. Pip. Conf.*, vol. Volume 6B:, Vancouver, British Columbia, Canada. July 17–21, 2016. V06BT06A074. ASME., 2016.

[115] I. T. Deaquino, "Fatigue evaluation of piping connections under thermal transients," *Int. J. Pres. Ves. & Piping*, vol. 61, pp. 9–12, 1994.

[116] D. Kronemeijer and R. Neggers, "Weldolet Inspections at Elevated Temperatures," *9th European Conference on NDT Berlin (Germany) (ECNDT 2006)*, pp. 2–8, 2006.

[117] S. B. Leen, M. Li, R. A. Barrett, S. Scully, D. Joyce, and P. E. O'Donoghue, "High temperature, multi-material, cyclic plasticity of a P91 welded branch-header connection under cyclic pressure," *Proc. ASME 2015 Press. Vessel. Pip. Conf.*, vol. Volume 3:

[118] R. P. Skelton and D. Gandy, "Creep-fatigue damage accumulation and interaction diagram based on metallographic interpretation of mechanisms," *Mater. High Temp.*, vol. 25, no. 1, pp. 27–54, 2008.

[119] A. Kapoor, "A Re‐evaluation of the life to rupture of ductile metals by cyclic plastic strain," *Fatigue Fract. Eng. Mater. Struct.*, vol. 17, no. 2, pp. 201–219, 1994.

[120] M. N. James, "Residual stress influences on structural reliability," *Eng. Fail. Anal.*, vol. 18, no. 8, pp. 1909–1920, 2011.

[121] L. Tan, L. Zhao, P. Zhao, L. Wang, J. Pan, and X. Zhao, "Effect of welding residual stress on operating stress of nuclear turbine low pressure rotor," *Nucl. Eng. Technol.*, vol. 52, no. 8, pp. 1862–1870.

[122] V. A. Degtyarev, B. S. Shul'ginov, O. N. Mikhailov, and O. I. Gushcha, "Effect of cyclic creep on residual welding stresses," *Strength Mater.*, vol. 20, no. 3, pp. 301–308, 1988.

[123] "Data sheets on the elevated-temperature properties. NIMS Creep Datasheet 43A. Tsukuba, Japan: National Institute for Materials Science." .

[124] T. H. Hyde, M. Saber, and W. Sun, "Testing and modelling of creep crack growth in compact tension specimens from a P91 weld at 650°C," *Eng. Fract. Mech.*, vol. 77, no. 15, pp. 2946–2957, 2010.

[125] A. H. Yaghi, T. H. Hyde, A. A. Becker, and W. Sun, "Finite element simulation of

welding and residual stresses in a P91 steel pipe incorporating solid-state phase transformation and post-weld heat treatment," *J. Strain Anal. Eng. Des.*, vol. 43, no. 5, pp. 275–293, 2008.

[126] A. H. Yaghi, T. H. Hyde, A. A. Becker, J. A. Williams, and W. Sun, "Residual stress simulation in welded sections of P91 pipes," *J. Mater. Process. Technol.*, vol. 167, no. 2–3, pp. 480–487, 2005.

[127] A. H. Yaghi, T. H. Hyde, A. A. Becker, and W. Sun, "Numerical simulation of P91 pipe welding including the effects of solid-state phase transformation on residual stresses," *Proc. Inst. Mech. Eng. Part L J. Mater. Des. Appl.*, vol. 221, no. 4, pp. 213–224, 2007.

[128] S. Mechanics, "FE-calculated stresses in a multi-pass butt-welded pipe-A simplified approach," *Int. J. Pres. Ves & Piping*, vol. 38, pp. 227–243, 1989.

[129] G. John, C. Aditya, and B. Malcolm, "A New Finite Element Model for Welding Heat Sources," *Metall. Trans. B*, vol. 15, no. 2, pp. 299–305, 1984.

[130] M. Abid and M. J. Qarni, "3D Thermal finite element analysis of single pass girth welded low carbon steel pipe-flange joints," *Turkish J. Eng. Environ. Sci.*, vol. 33, no. 4, pp. 281–293, 2009.

[131] J. R. Chukkan, G. Wu, M. E. Fitzpatrick, E. Eren, X. Zhang, and J. Kelleher, "Residual stress redistribution during elastic shake down in welded plates," *MATEC Web Conf.*, vol. 165, pp. 1–6, 2018.

[132] W. Wei, L. Han, Y. Feng, J. Zhang, and H. Wang, "Low cycle fatigue behavior of N80Q steel under the influence of mean strains," *Mater. Sci. Forum*, vol. 944 MSF, pp. 1067–1075, 2018.

[133] W. Wei *et al.*, "Low-cycle fatigue behavior and fracture mechanism of HS80H steel at different strain amplitudes and mean strains," *J. Mater. Eng. Perform.*, vol. 26, no. 4, pp. 1717–1725, 2017.

[134] B. Das and A. Singh, "Cyclic mean stress relaxation behaviour of P91 steel: Experiments and constitutive modeling," *Procedia Struct. Integr.*, vol. 14, pp. 619–626, 2019.

[135] R. H. Koztowski and M. Technology, "The effect of residual stresses and weld geometry on the improvement of fatigue life," *J. Mater. Process. Technol.*, vol. 53, pp. 239–246, 1995.

[136] B. L. K. Ian Milne, R. O. Ritchie, "Comprehensive Structural Integrity, Volume 4." 2007.

[137] H. Egner and M. Piotrowski, “Effects of fatigue testing on low-cycle properties of P91 steel,” *Int. J. Fat.,* vol. 120, pp. 65–72, 2019.